ADAPTIVE FINITE ELEMENT METHODS FOR FLUORESCENCE ENHANCED OPTICAL TOMOGRAPHY

A Dissertation

by

AMIT JOSHI

Submitted to the Office of Graduate Studies of
Texas A&M University
in partial fulfillment of the requirements for the degree of

DOCTOR OF PHILOSOPHY

August 2005

Major Subject: Chemical Engineering

ADAPTIVE FINITE ELEMENT METHODS FOR FLUORESCENCE ENHANCED OPTICAL TOMOGRAPHY

A Dissertation

by

AMIT JOSHI

Submitted to the Office of Graduate Studies of
Texas A&M University
in partial fulfillment of the requirements for the degree of

DOCTOR OF PHILOSOPHY

Approved by:

Chair of Committee,	Eva M. Sevick-Muraca
Committee Members,	J.N. Reddy
	L.V. Wang
	M. Bevan
	D.M. Ford
Head of Department,	K.R. Hall

August 2005

Major Subject: Chemical Engineering

ABSTRACT

Adaptive Finite Element Methods for Fluorescence Enhanced Optical Tomography. (August 2005)

Amit Joshi, B.E.(with honors), Panjab University, India

Chair of Advisory Committee: Dr. Eva M. Sevick-Muraca

Fluorescence enhanced optical tomography is a promising molecular imaging modality which employs a near infrared fluorescent molecule as an imaging agent and time-dependent measurements of fluorescent light propagation and generation. In this dissertation a novel fluorescence tomography algorithm is proposed to reconstruct images of targets contrasted by fluorescence within the tissues from boundary fluorescence emission measurements. An adaptive finite element based reconstruction algorithm for high resolution, fluorescence tomography was developed and validated with non-contact, planewave frequency-domain fluorescence measurements on a tissue phantom. The image reconstruction problem was posed as an optimization problem in which the fluorescence optical property map which minimized the difference between the experimentally observed boundary fluorescence and that predicted from the diffusion model was sought. A regularized Gauss-Newton algorithm was derived and dual adaptive meshes were employed for solution of coupled photon diffusion equations and for updating the fluorescence optical property map in the tissue phantom. The algorithm was developed in a continuous function space setting in a mesh independent manner. This allowed the meshes to adapt during the tomography process to yield high resolution images of fluorescent targets and to

accurately simulate the light propagation in tissue phantoms from area-illumination. Frequency-domain fluorescence data collected at the illumination surface was used for reconstructing the fluorescence yield distribution in a 512 cm^3, tissue phantom filled with 1% Liposyn solution. Fluorescent targets containing 1 micro-molar Indocyanine Green solution in 1% Liposyn and were suspended at the depths of up to $2cm$ from the illumination surface. Fluorescence measurements at the illumination surface were acquired by a gain-modulated image intensified CCD camera system outfitted with holographic band rejection and optical band pass filters. Excitation light at the phantom surface source was quantified by utilizing cross polarizers. Rayleigh resolution studies to determine the minimum detectable sepatation of two embedded fluorescent targets was attempted and in the absence of measurement noise, resolution down to the transport limit of $1mm$ was attained. The results of this work demonstrate the feasibility of high-resolution, molecular tomography in clinic with rapid non-contact area measurements.

To my parents

ACKNOWLEDGMENTS

This dissertation owes its successful completion to a number of people. My gratitude goes to Dr. Eva Sevick-Muraca for supporting my work, keeping faith in my ideas and abilities, emphasizing the power of creativity in science and more than anything else, teaching the timeless lessons of ethics, compassion, leadership and teamwork. Great thanks are due to Dr. Wolfgang Bangerth, who provided the inspiration for this research. His comments, and the effort put by him in this project are invaluable. His friendship (gained courtesy of www.google.com) will be the enduring legacy of this research. Colleagues Kildong Hwang, John Rasmussen, and Jessica Houston provided excellent and patient support in the laboratory. Dr. Ranadhir Roy initiated my curiosity and provided the motivation for venturing into the field of optical tomography. Friends, Sarabjyot Dali, and Amit Sahu have been with me in times of failure and times of success. The encouragement and the always positive remarks provided by Tianshu Pan, and Feng Liang have been a great support. Thanks are also due to the past members of the Photon Migration Laboratories, especially Dr. Anuradha Godavarty, and Alan Thompson who left a foundation of robust experimental techniques for me to build on. The unwavering support and love of my parents and sisters has held me firm on the path to Ph.D. in these past years. And at last I would like to acknowledge the bedrock of my life, my significant other Ruchi, whose unqualified love and sincere advice helped me sail through this venture.

I thank the committee members Dr. J.N. Reddy, Dr. L. Wang, Dr. D.M. Ford

and Dr. M. Bevan for going through the dissertation and their helpful comments. I am grateful to Dr. Perla Balbuena for agreeing to substitute for Dr. Bevan at a short notice. The financial support for the research work described in this dissertation was provided by National Institutes of Health grants RO1CA67176 and RO1CA88082

ABBREVIATIONS

ART	Algebraic reconstruction techniques
CW	Continuous wave
DTTCI	3,3-diethylthiatricarbocyanine
FDPM	Frequency domain photon migration
FOV	Field of view
GN	Gauss Newton method
ICG	Indocyanine Green
RTE	Radiative transport equation
TDPM	Time domain photon migration

NOMENCLATURE

C_{sca}	Scattering cross-section
d_k	Optimization update direction
$D_{x,m}$	Diffusion coefficient at excitation or emission wavelength
E	Optimization error function
g	Scattering anisotropy
$\mathbf{g}_E$	Gradient of the error function
G	Green's function
$\mathbf{H}_E$	Hessian matrix
H_x	Excitation diffusion/transport operator
H_m	Emission diffusion/transport operator
$\mathbf{J}$	Jacobian matrix
$L(\cdot)$	Lagrange functional
$L_{x,m}$	Angular fluence at excitation or emission wavelength
q_{scat}	angle dependent scattering efficiency
$p(\hat{s}, \hat{s}')$	Scattering phase function
$p(\cdot\|\cdot)$	Conditional probability
P_l	Legendre polynomial of order l
$\hat{s}, \hat{s}'$	Scattering directions
u	Excitation fluence
v	Emission fluence

α	Optimization step length
ε	fluorophore extinction coefficient
μ_a	Absorption coefficient
μ_s	Scattering coefficient
μ_t	Attenuation coefficient
$\mu_{ax,mi}$	Absorption due to chromophores at excitation or emission wavelength
$\mu_{ax,mf}$	Absorption due to fluorophore at excitation or emission wavelength
τ	Fluorophore lifetime
θ	Scattering angle
λ	Wavelength
$\lambda^{ex,m}$	Lagrange multipliers for excitation or emission diffusion equations
Γ	Rate constant for radiative relaxation of fluorophore
K_{nr}	Rate constant for non-radiative relaxation of fluorophore
ϕ	Quantum efficiency of the fluorophore
φ	Finite element weight functions

TABLE OF CONTENTS

CHAPTER Page

CHAPTER Page

Page

LIST OF TABLES

LIST OF FIGURES

FIGURE Page

FIGURE Page

FIGURE Page

FIGURE Page

CHAPTER I

INTRODUCTION

A. Molecular imaging

In vivo molecular imaging encompasses a rapidly growing research area emerging from the convergence of advances in molecular biology, chemistry, and imaging research. After the success of the first phase of human genome project, emphasis is now on the understanding of gene expression and protein function to illuminate the biomolecular steps preceding disease. *In vivo* molecular imaging is broadly defined as the visualization, characterization, and measurement of biological processes at the cellular and molecular levels. [2] As functional or molecular changes precede the development of anatomical changes, molecular imaging promises early diagnosis of human infirmities and may prove to be a useful tool for therapeutic monitoring and drug discovery. Upon realization of its full potential, molecular imaging research could transform current medical science from an enterprize focused on diagnosis and therapeutics to a disease prediction and prevention system. [3, 4, 5] Conventional medical imaging modalities, which include X-ray computed tomography, magnetic resonance imaging, and ultrasound imaging are inadequate for molecular imaging because of lack of sensitivity and specificity for functional or molecular contrast. Fluorescence optical tomography can exploit a wide range of molecular contrast in living systems with the aid of suitably designed fluorescent contrast agents. For flu-

---

This dissertation follows the style of *IEEE Transactions on Automatic Control.*

orescence optical tomography to emerge as a leading molecular imaging technique, we need to demonstrate its ability to interrogate functional and metabolic states of tissue at sufficiently high resolution to enable the extraction of pertinent spatial information. This dissertation presents a novel tomography scheme coupled with a non-contact imaging approach to generate rapid, high resolution, three-dimensional images of Fluorophore distribution in tissue-like phantoms. Before describing the developed fluorescence tomography scheme, a brief survey of other competing molecular imaging modalities is presented and their advantages and disadvantages are highlighted.

1. Single photon emission computed tomography (SPECT)

Single photon emission computed tomography is a molecular imaging modality which depends upon traditional nuclear imaging coupled with computed tomography algorithms for image reconstruction. SPECT uses radio-pharmaceuticals to target different tissue environments. γ emitting isotopes (e.g. ^{99}Tc, ^{111}In, ^{123}I, ^{131}I) are typically used to label the pharmaceuticals used as molecularly targeting probes(e.g. enzyme specific peptide sequences, mono-clonal antibodies etc.). γ photons emitted by the radioactive source are detected by Gamma cameras which rotate around the subject to acquire projection data from different views. These planar images are then converted to three dimensional maps of radio-isotope distribution by employing the standard computed tomography algorithms. [6] A detailed review of SPECT imaging can be found in reference. [7]

SPECT and its non-tomographic form gamma-scintigraphy, [8] are popular mole-

cular imaging modalities in clinic as they employ standard radio-isotopes which have comparatively longer half lives than the probes used for positron emission tomography(PET). In addition, the emitted gamma photons have lower energies (140keV for ^{99m}Tc) than PET photons (511keV), resulting in lower cost instrumentation and isotope handling. Furthermore SPECT imaging has a five decade old research track record in the development of radio-pharmaceuticals, instrumentation, and image processing techniques. Gamma photons emitted in tissue undergo photo-electric and Compton interactions as they propagate resulting in attenuation of signal with pathlength. These photons are emitted isotropically, thus collimation is required to restrict projection data to γ photons emitted in a certain direction. Collimation increases the resolution at the cost of sensitivity as significant numbers of photons are blocked by the lead collimators. The detection efficiency is approximately 10^{-4} times the emitted number of γ photons. For 1cm resolution, PET is about 15 times more sensitive than SPECT. Sensitivity limitations in SPECT can be improved by employing recently developed high resolution pinhole SPECT systems which have reported resolutions up to 1.7mm in small animals. [9] SPECT allows multiple event imaging by employing multiple isotopes emitting γ photons with different energies. Molecular imaging applications of SPECT include reporter gene imaging, gene therapy and cell tracking. [10]

2. Positron emission tomography (PET)

Positron emission tomography employs biological molecules with a positron emitting isotope (e.g. ^{11}C, ^{13}N, ^{15}O or ^{18}F) in place of the normal stable isotope. The

injected isotope accumulates in the areas for which the molecule has affinity. The radio-active nuclei then decay with a positron emission. The positron collides with the nearest electron and annihilates resulting in a 511 keV γ photon pair production. The emitted photons travel at 180 degrees to each other and are detected by an array of detectors surrounding the subject. After 100000 or more annihilation events are registered, tomographic reconstruction algorithms are used to generate the three dimensional map of radio-isotope distribution in the subject. [11] Spatial resolution of clinical scanners is $6-8\ mm^3$. Small animal micro-PET scanners can reach spatial resolutions of up to $1-2mm^3$. [12, 13] Advantages of PET are its high sensitivity (1 to 10 pico-moles of tracer can be detected) and the use of physiological tracers, hence chelation chemistry is not required to incorporate the radionuclide in the tracer as in SPECT. PET imaging is well suited for translational research as molecular imaging assays with PET can be validated in cell culture and small animal models prior to use of the same reported probe in clinic. Radio-isotopes used in PET tracers are typically short lived (half life on the order of 100 minutes). This is the primary disadvantage of PET imaging as it increases the cost and restricts PET imaging to centers in close proximity to radiopharmacies. Molecular imaging applications with PET include metabolic imaging, gene expression imaging, receptor-ligand, and enzyme targeting. [10, 14]

3. Contrast enhanced magnetic resonance imaging(MRI)

Magnetic resonance imaging relies on the contrast provided by interaction of nuclei with magnetic moments and angular momentum (e.g. ^{1}H, ^{13}C and ^{31}P), with an

external magnetic field. MR tissue characterization depends primarily on the detection of water protons through the application of radio-frequency pulses to the sample placed in a strong magnetic field(>1.5T). Variations in the tissue micro-environments cause variations in the relaxation behavior of protons once the radio-frequency pulse is removed. [15] This provides the contrast between different tissue types in MR images. MR imaging detects the concentration of water, longitudinal, or T1 relaxation time which depends upon the interaction of resonant nuclei with the magnetic fields of surrounding nuclei and transverse or T2 relaxation time which depends upon the interaction of nuclear spin with adjacent nuclear spins. MR images provide excellent soft tissue contrast and resolution down to 1mm for systems with applied magnetic fields of $1.5 - 2$T. [15] Resolution as high as $10\mu m$ has been attained with the use of magnetic field strengths of $4 - 7$T. [5, 11] Intrinsic MR contrast can be provided by variations in tissue oxygenation levels, a fact used in the study of brain function. However plain MR imaging is not a true molecular imaging modality because its extremely low sensitivity as only one out of 1 million hydrogen nuclei align themselves in an applied magnetic field of 1.5T. Magnetic contrast can be enhanced in desired locations by employing 'smart' molecular probes which typically consist of chelated paramagnetic species like Gadolinium or dysprosium or super-paramagnetic iron nanoparticles. [16, 17] These signal amplification strategies have been used for molecular imaging applications such as imaging receptor expression and regulation, enzyme-substrate interactions and visualizing the progress of gene therapy. MR imaging can produce high resolution anatomical and functional maps simultaneously. The disadvantage of MRI as a molecular imaging modality is

its low sensitivity [11], typically millimolar concentrations of contrast agents are required compared to nanomolar concentrations and less needed for nuclear or optical imaging [5]. The high cost of MR imaging apparatus is another disadvantage.

4. Contrast enhanced ultrasound tomography

Ultrasound tomography relies on the contrast provided by the variation in the elastic properties of tissue. Ultrasound can detect morphological changes associated with disease and is not a molecular imaging modality in its native form. However recent developments in ultrasound contrast agents such as nanoparticles which can coat desired tissue surfaces, or microbubbles attached to molecular probes have pushed ultrasound into the league of molecular imaging modalities. [5] High resolutions of 30 to 60 microns have been reported for small animal ultrasound tomography systems utilizing sound waves with frequency ranges of 40-60 MHz. [18] Micro-bubble based contrast agents have been used to image tumor vasculature and membrane receptors. [19] The advantages of ultrasound are its low cost, real time imaging and ubiquity in clinics. Molecular imaging with ultrasound is an emerging research area, but has not yet reached the specificity and sensitivity of nuclear or optical imaging.

5. Diffuse optical tomography

Diffuse optical tomography exploits the fact that near infrared photons (700-900nm wavelength) are multiply scattered nd minimally absorbed in tissues. [20] NIR optical tomography seeks to reconstruct the photon absorption and scattering maps of the tissue media from boundary light measurements. Measurements can be acquired

in a steady state fashion or in a time dependent manner by employing pulsed or modulated light sources. Tissue absorption maps in the NIR are affected by the concentrations of oxygenated and deoxygenated hemoglobin, water, and lipids providing contrast for functional imaging with NIR light. Diffuse optical tomography can not address specific biomolecular signatures and hence it is not a true molecular imaging modality. It has been primarily used for imaging tumor angiogenesis, however its performance is affected by low endogenous contrast (2:1) between tumor and healthy tissue. Resolution is on the order of 1cm. Ntziachristos *et al* [21] have performed diffuse optical tomography on malignant breast tissue by employing the enhanced absorption contrast provided by ICG which is a blood pooling agent. The sensitivity and specificity of diffuse optical tomography can be substantially improved by employing fluorescence or bioluminicent contrast agents which is the topic of next section.

6. Fluorescence enhanced optical tomography

Fluorescence enhanced optical tomography is an emerging molecular imaging modality which stands apart from the traditional molecular imaging approaches such as nuclear imaging and functional magnetic resonance imaging. In fluorescence optical tomography, an NIR excitation signal is applied at the tissue boundary, The NIR photons diffuse through the tissue domain and upon reaching an NIR excitable fluorophore, an emission wave is emitted at a longer wavelength. Measurements at the fluorescence emission wavelength provide the information for locating the fluorescence source distribution in tissue. Unlike nuclear imaging, fluorescence en-

hanced optical imaging employs non-ionizing radiation. Furthermore it requires only nanomolar concentrations of the molecular contrast agents [22] compared to the millimolar concentrations of contrast agents required for magnetic resonance imaging. Molecular imaging with fluorescent contrast agents has been demonstrated for visualizing gene expression in small animals [23], for in-vivo imaging of tumors and metastases [24], and for monitoring the spatio-temporal state of bacterial infections and immune response [25]. These applications have used Green Fluorescent Protein (GFP) as fluorescing agent which does not emit in the near infrared region, hence the tissue depth analyzed was only on the order of $2-5mm$. Red Shifted GFP mutants are now being synthesized which can improve the depth of penetration [26]. As near infrared light can travel several centimeters in tissue, fluorescence enhanced NIR optical imaging promises to open new pathways for the characterization of biological processes in living animals at cellular and molecular level. Optical tomography has seen rapid developments in the past decade. Multiple approaches have been proposed for contrast enhanced optical tomography based on fluorescence or bioluminescence. Tomographic image reconstruction in fluorescence imaging involves determination of the fluorophore yield and lifetime distribution in the tissues from a finite number of boundary fluorescence measurements. The forward problem in fluorescence optical tomography involves the determination of boundary fluorescence measurements, provided the tissue optical property map and the excitation source is known while the inverse problem involves the determination of distributed optical property map from the knowledge of boundary measurements. Inverse image reconstruction is a non-trivial problem because of the diffusive nature of photon propagation in tissue.

Initial efforts by O'Leary*et al.* [27], Wu [28] *et al.* and Hull*et al.* [29] focused on localization strategies for a fluorescent perturbation in an otherwise homogeneous medium. Schotland [30] proposed a back-projection algorithm for fluorescent optical tomography. O'Leary *et al.*. [31] and Ntziachristos *et al.* [32, 33] used the born approximation with algebraic reconstruction techniques. Chernomerdik *et al.* [34] have used random walk theory for three dimensional reconstructions of fluorophore concentration and recently Quan *et al.* [35] proposed a fast fluorescence localization algorithm. These approaches are successful in locating small targets in homogeneous backgrounds with low sample volumes. Other fluorescence tomography approaches cast the image reconstruction problem as an optimization problem in which a least squares type minimization is performed to determine the fluorescence map which best matches the measured boundary fluorescence energy distribution with that predicted by a light transport model. These approaches are more general in their scope and can handle heterogeneous backgrounds and large sample volumes at the cost of higher computational expenses. Paithankar *et al.* [36] used a Newton-Raphson algorithm along with a finite difference based numerical solution for diffusion equations. Eppstein *et al.* [37, 38] implemented an approximated Kalman filter based fluorescence tomography algorithm. Recently finite element methods have become popular for forward modelling. Finite element based fluorescence tomography algorithms have been proposed by Roy *et al.* [39] and Jiang *et al.* [40]. These algorithms use Newton or Newton type optimization schemes. Godavarty *et al.* [41] have used a finite element based forward model with approximate extended Kalman filter to perform fluorescence tomography in clinically relevant geometries. Hielscher *et al.* [42] and

Chang *et al.* [43] have employed the radiative transport model for fluorescence tomography. Recently Ntziachrsitos *et al.* [32] have reported sub-millimeter resolution for diffuse fluorescence molecular tomography for small animals. Achieving this resolution in clinical situations will entail enormous computational burden with regards to the dimensionality of the finite element or finite difference mesh and the inverse problem will be too ill-posed to solve accurately. Further a sub-millimeter resolution in diffuse fluorescence tomography doesn't make any sense as it violates the continuum limit(approx. $1mm$) for the diffuse propagation of photons in tissue.Past work done in the field of fluorescence optical tomography is summarized in Table-I.

B. Research goals

For fluorescence optical tomography to emerge as a leading molecular imaging technique, we need to demonstrate its ability to interrogate functional and metabolic states of tissue at high resolution. Resolution is set by the level of discretization in the inverse imaging problem. To date, the discretization level is selected *a priori* based on the knowledge of the domain or computational constraints. Image quality can be improved by uniformly refining the discretization. This type of global refinement further increases the ill-posedness of the problem and the computational burden can become insurmountable for three dimensional image reconstructions in clinically relevant geometries. Adaptive mesh refinement which provides fine mesh resolution around the target location and a coarse resolution in the other regions may improve the quality of tomographic reconstructions in fluorescence optical imaging. It also can be used to refine the mesh near the excitation sources, where the spatial gradients are

TABLE I

Literature survey of fluorescence tomography approaches.

Author	Mode	Data	Contrast	Forward	Inverse	Comments
O'Leary *et al* [27] (1994)	FDPM	Phantom (2D)	ICG (perfect)	Analytical solution (Diffusion)	Localization	One dimensional localization of μ_{axf} heterogeniety
Wu *et al* [28] (1995)	TDPM	Phantom (2D)	DTTCI (perfect)	None	Localization	Two dimensional localization of μ_{axf} heterogeniety
Schotland *et al* [30] (1997)	CW	Simulated (3D)	Not specified	Analytical solution (Diffusion)	Backprojection	Generalized Radon transform for optical tomography
O' Leary *et al* [31] (1996)	FDPM	Simulated (2D)	ICG (perfect)	Analytical solution (Diffusion)	ART	Two dimensional reconstruction of μ_{axf} and τ map
Paithankar *et al* [36] (1997)	FDPM	Simulated (2D)	ICG (perfect+ imperfect)	Multigrid Finite difference (Diffusion)	Newton Raphson	Two dimensional reconstruction of μ_{axf} and τ map
Chang *et al* [43] (1997)	CW+ FDPM	Simulated (3D)	Rhodamine (perfect+ imperfect)	Monte Carlo (Radiative transport)	Conjugate gradient	Three dimensional reconstruction of μ_{axf} map
Jiang *et al* [40] (1998)	FDPM	Simulated (2D)	Not Specified (imperfect)	Finite Element (Diffusion)	Levenberg-Marquardt	Two dimensional reconstruction of μ_{axf} and τ map
Hull *et al* [29] (1998)	CW	Phantom (3D)	Nile Blue A (perfect)	Analytical solution (Diffusion)	Regression	One dimensional localization of μ_{axf} heterogeniety
Roy *et al* [39] (1999)	FDPM	Simulated (2D)	ICG (perfect+ imperfect)	Finite element (Diffusion)	Truncated Newton	Two dimensional reconstruction of μ_{axf} and τ map
Eppstein *et al* [37] (1999)	FDPM	Simulated (2D)	ICG (perfect+ imperfect)	Multigrid finite difference (Diffusion)	Kalman filter	Two dimensional reconstruction of μ_{axf} and τ map
Chernomerdik *et al* [34] (1999)	CW	Phantom (3D)	Rhodamine (perfect)	Random walk model	Random walk theory	Depth reconstruction of μ_{axf} target
Ntziachristos *et al* [33] (2001)	CW	Phantom (3D)	ICG/Cy5.5 (perfect)	Born-Rytov approximation (Diffusion)	ART	Three dimensional reconstruction of μ_{axf} map
Eppstein *et al* [38] (2002)	FDPM	Phantom (3D)	ICG (perfect+ imperfect)	Multigrid finite difference (Diffusion)	Kalman filter	Three dimensional reconstruction of μ_{axf} and τ map
Hielscher *et al* [44] (2003)	CW	Simulated (2D)	Not specified (perfect)	Finite difference (Radiative transport)	Quasi-Newton	Two dimensional reconstruction of μ_{axf} map
Godavarty *et al* [41] (2003)	FDPM	Phantom (3D)	ICG (perfect+ imperfect)	Finite element (Diffusion)	Kalman filter	Three dimensional reconstruction of μ_{axf} map
Quan *et al* [35] (2004)	TDPM	Simulated (3D)	ICG (perfect)	Monte Carlo (Radiative transport)	Weighted Backprojection	Fast localization of μ_{axf} contrast

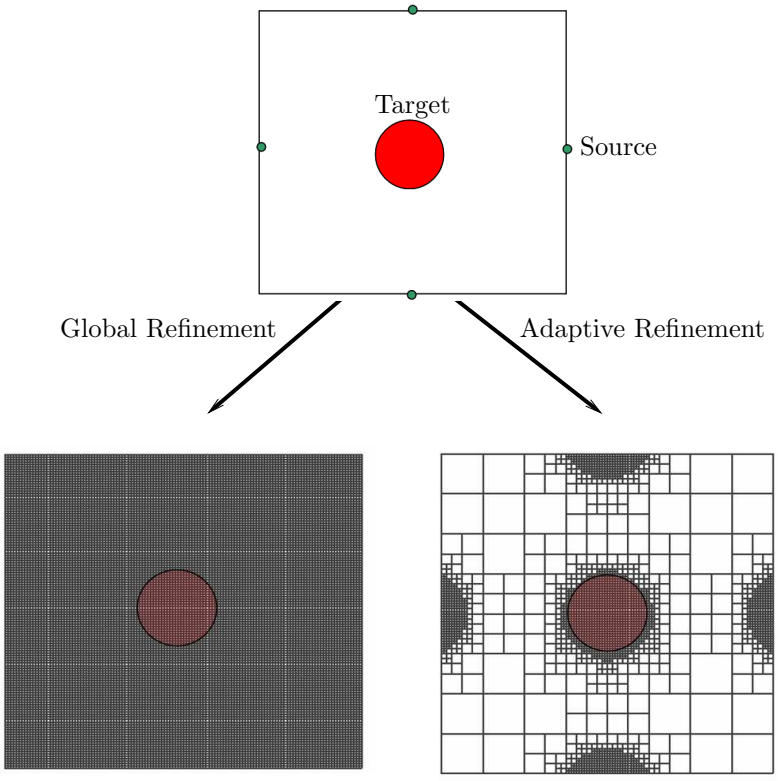

Fig. 1. Global vs. adaptive refinement for a 2-dimensional case, Fluorescent target is at the center and excitation light is provided by four point sources on the edges.

high and the discretization level impacts the accuracy of the forward solution. Fig.1 illustrates the global and adaptive mesh refinements for a hypothetical 2-dimensional case. The computational savings with adaptive mesh refinement are obvious. One of the major advantages of molecular imaging using fluorescent contrast agents is that it requires less than nano-molar amounts of the contrast agent, hence the ability to image smaller targets is important for fluorescence tomography schemes. Adaptivity refines the mesh where needed producing sharp corners but keeps the number of unknowns limited. Resolution archived by current tomographic schemes depends on the mesh used which is designed *a priori*. Adaptive mesh refinement can aid in resolving multiple fluorescent targets.

In this dissertation we present an adaptive finite element based algorithm for fluorescence enhanced frequency domain optical tomography. To the best of candidates knowledge, this is the first ever demonstration of a truly adaptive fluorescence optical tomography system. In addition to the development of diffusion model based fluorescence tomography, a fast image reconstruction scheme was also developed for small animal imaging by utilizing the radiative photon transport equation. The specific aims of this research effort are:

1. **Develop an adaptive finite element based solver for forward modeling of fluorescence tomography.** An adaptive finite element program was developed to solve the coupled diffusion equations for forward modelling of fluorescence optical tomography and validated with experimental data.

2. **Develop an adaptive finite element based algorithm for fluorescence tomography.** A Gauss-Newton algorithm was derived for fluorescence tomog-

raphy in an infinite dimensional function space setting independent of any *a priori* discretization. Dual adaptive finite element meshes for solving diffusion equations and for reconstructing the fluorescence property map in the tissue domain were employed for Gauss-Newton updates. The algorithm was implemented in C++ with object oriented programming techniques utilizing the platform developed by Dr.Wolfgang Bangerth for solving large scale inverse problems and the DEAL.II finite element libraries.

3. **Validate the adaptive fluorescence tomography algorithm with measurements from a frequency domain ICCD imaging system** The developed algorithm was tested on a tissue phantom with area-illumination and area-detection measurement geometry. A frequency domain intensified charge coupled device camera system was constructed in the Photon Migration Laboratory was used to test the ability of the proposed algorithm to reconstruct fluorescent targets buried in an 8cm x 8cm x 8cm phantom from surface fluorescent measurements. The phantom was illuminated by an expanded NIR laser beam and fluorescent targets of sizes upto $5mm$ diameter and buried at the depths of upto $2cm$ from the illumination surface were reconstructed

4. **Resolution studies** Rayleigh resolution studies were attempted by imaging two fluorescent targets placed at varying distances along the lateral(x-y plane) direction. The adaptive mesh refinement algorithm was used to reconstruct the fluorescent target locations. Image reconstructions were successfully performed with the actual experimental source and simulated measurement data. Reconstructions with experimental measurement data were limited by signal

to noise characteristics of the intensified CCD camera.

5. **Small animal tomography with radiative transport based forward model** A novel three-dimensional tomography algorithm integrating the traditional algebraic reconstruction techniques, with the frequency-domain Boltzmann transport equation, was developed for imaging small animal models. Tomographic images of $5mm$ targets buried in a tissue phantom were obtained by simulated point-illumination and point-detection measurements. Dual tetrahedral finite element meshes were used for the solution of radiative transport equations and for reconstructing the fluorescence absorption map.

Fig.2 presents the organization of this dissertation.

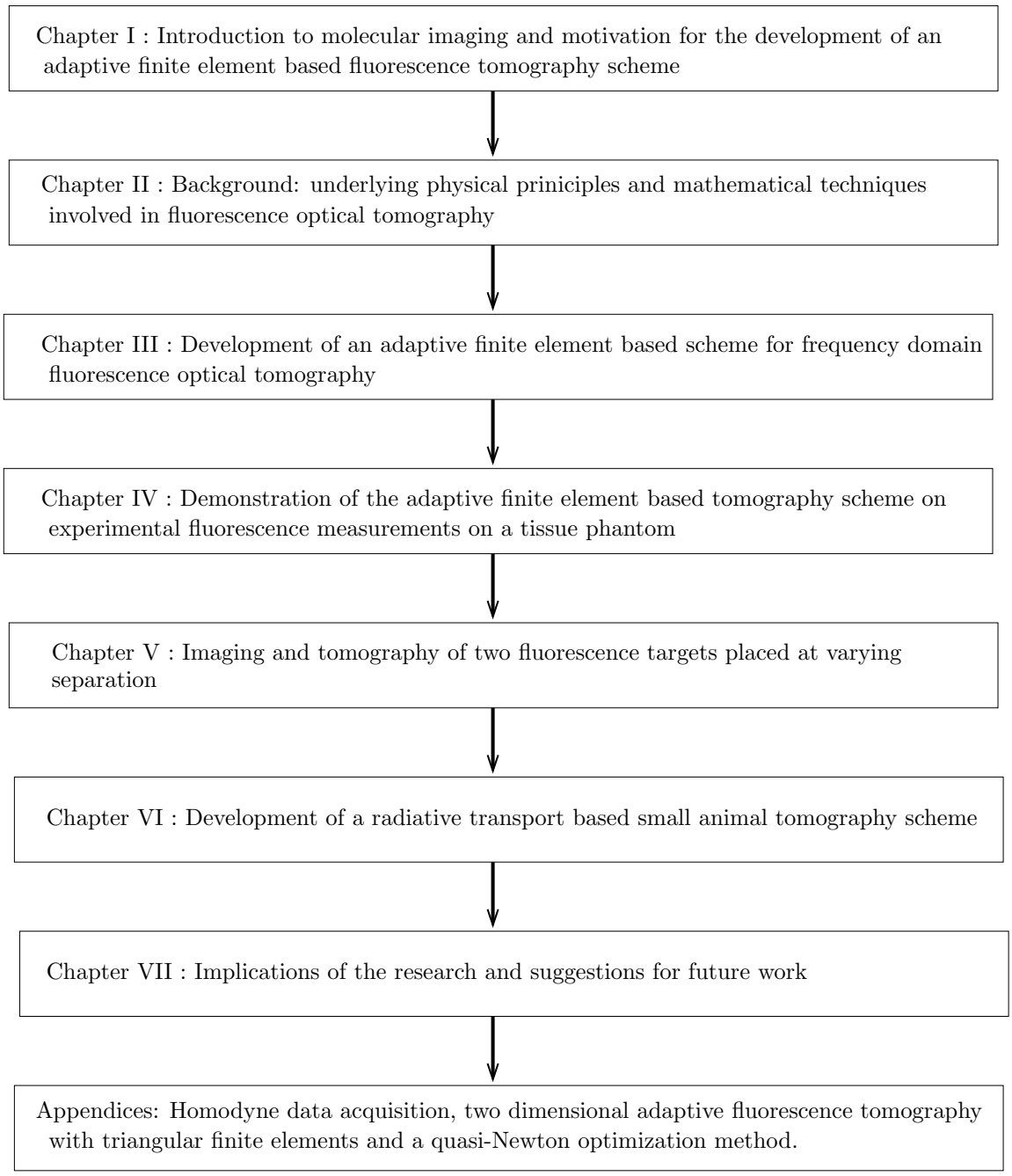

Fig. 2. Organization of the dissertation.

CHAPTER II

BACKGROUND

A. Interaction of light with tissue

Light is either scattered or absorbed as it traverses through tissues. Primary scattering centers in tissue are cellular organelle such as cell nuclei and mitochondria. Characterization of absorption and scattering properties of tissue is a prerequisite for further study of non-invasive optical diagnostic techniques. Under the classical physics treatment, light is considered as an electromagnetic wave. However the photon picture of light propagation provides an elegant means of illustration of light scattering, absorption, and propagation in tissue. Light is scattered when it hits a particle with a different refractive index than its surroundings. Scattering changes the propagation direction of light. Fig.3 illustrates a case when a uni-directed light beam is scattered by a spherical particle. θ is the scattering angle. Light is scattered predominantly in a forward direction by tissues. At a macroscopic level, tissue

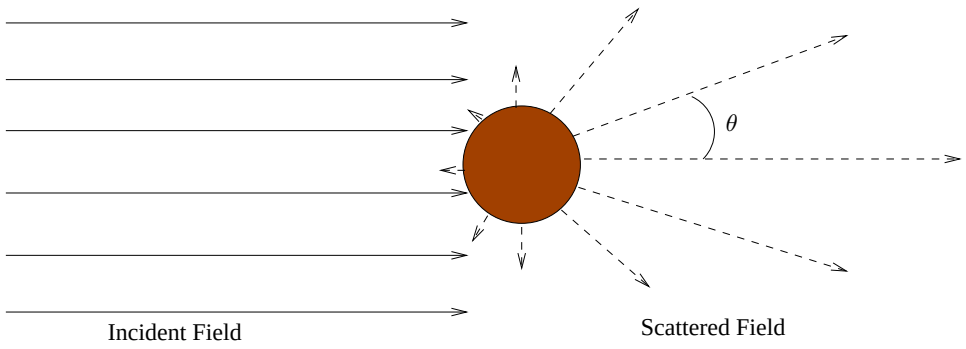

Fig. 3. Single scattering by a spherical particle, whereby θ is the scattering angle.

scattering and absorption are described by the scattering coefficient μ_s, and the absorption coefficient μ_a, with the dimensions of L^{-1}. These coefficients describe the probability of a photon being scattered or absorbed per unit length of the distance traversed. Another important parameter is the scattering anisotropy g, which is the mean of the cosine of the scattering angle θ. Mie scattering theory provides the solutions for the scattering coefficient and anisotropy provided the scatterer dimension, refractive index and the wavelength are known. An empirical relation known as the Beer-Lambart law is used to describe the absorption coefficient in non-scattering systems from the attenuation of light.

1. Mie scattering theory

Mie scattering theory is applicable under the conditions of single independent scattering. The scatters are assumed to be separated by distances much greater than the wavelength λ of the incident light so that the scattered fields from different particles are incoherent and the total scattered intensity can be obtained by the summation of individual scattered intensities. A closed form Mie solution is available for the scattering cross section of a spherical particle placed in a uniform incident field. Scattering cross section C_{sca}, is the effective particle cross-section seen by the incident field.

$$C_{sca} = \frac{\pi^2 a^2}{4} \int_{\theta=0}^{\theta=\pi} q_{scat}(\theta, a, n, \lambda) sin(\theta) d\theta \tag{2.1}$$

$q_{scat}(\theta, a, n, \lambda)$ is the angle dependent scattering efficiency predicted from the Mie theory provided that the particle radius a, refractive index n, and wavelength λ are

known. Mie theory also provides the solution for scattering anisotropy g.

$$g =< cos(\theta) >= \frac{\lambda^2}{16\pi C_{sca}} \int_{\theta=0}^{\theta=\pi} q_{scat}(\theta, a, n, \lambda) sin(\theta) cos(\theta) d\theta \tag{2.2}$$

The scattering cross-section C_{sca} is related to the macroscopic parameter μ_s by the following relation:

$$\mu_s = NC_{sca} \tag{2.3}$$

where, N is the number of scatterers per unit volume. In tissue, g varies from 0.7 to 0.95 and μ_s varies from 10 to 1000 cm^{-1} between UV and NIR wavelengths. [45]

2. Beer-Lambart law

The absorption coefficient, μ_a, is defined as the probability that a photon will be absorbed on traveling a unit length in the medium. Tissue absorption coefficients vary from 0.1 to 10000 cm^{-1}. [45] Chromophores are the species which absorb the incoming photons, resulting in the excitation of the electrons to higher energy levels followed by non-radiative relaxation which releases heat. Predominant chromophores in tissue include oxy and deoxyhemoglobin, melanin, myoglobin, and water. [46] The absorption coefficient is related to the Beer-Lambert extinction coefficient, ε, via:

$$\mu_a = 2.303\varepsilon C \tag{2.4}$$

where C is the concentration of chromophores in the medium. Absorption coefficients are measured from attenuation measurements in non-scattering solutions by applying

the Beer-Lambert law, which relates the light attenuation to the path length d.

$$log\frac{I_0}{I} = \mu_a d \tag{2.5}$$

I_0 is the incident light intensity and I is the light intensity measured at a distance d through the medium. Similar procedure is followed to determine the scattering coefficient via tubidity measurements, wherein light attenuation in a scattering solution is related to scattering coefficient μ_s by the Beer-Lambert law.

3. Diffuse light propagation in tissues

Photon propagation in tissues is dominated by multiple scattering. For most tissue types, the scattering coefficient dominates absorption, except for blood filled organs like liver and spleen where scattering and absorption are of the same order. Tissue anisotropy g typically varies from 0.7 to 0.99. For a review on the optical properties of different tissue types, refer to the reference [20]. As a result of high anisotropy, photon scattering in tissue is forward directed. Fig. 4 illustrates photon propagation in tissue. Each scattering event is forward directed but after sufficient number of scattering events, the photon propagation direction is randomized. This observation has prompted the description of photon propagation as a diffusive process in tissue. The propagation of light across restricted lengths where randomization does not occur is described by the full radiative transport equation. Section-II.C describes the mathematical models proposed to model photon propagation and their applicability ranges.

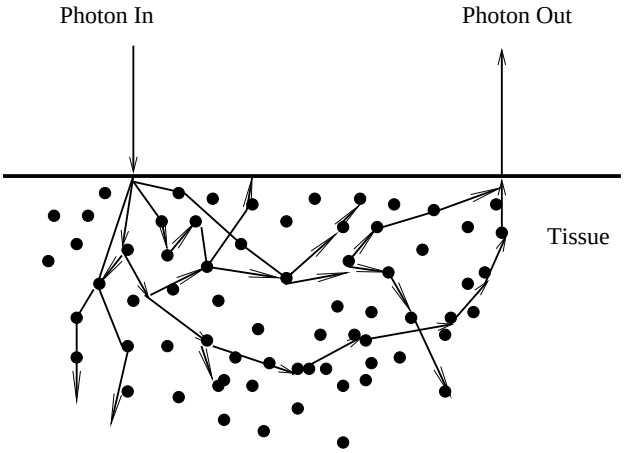

Fig. 4. Photon transport in tissue.

4. Fluorescence induced from exogenous probes

Contrast in NIR diffuse optical tomography is provided by the changes in absorption or scattering coefficients. However the endogenous contrast of diseased tissue is not sufficient to enable high SNR measurements. Exogenous fluorophore can be introduced into tissue for targeting specific disease markers, and thereby acting as an imaging agent or contrast agent. Incident NIR photons from the tissue surface diffuse through the tissue medium and upon reaching the fluorophore, they are absorbed and initiate fluorescence emission. Organic fluorescent molecules typically have aromatic or heterocyclic groups (typically cyanine [47] and porphyrin [48] derivatives) with delocalized electrons. These electrons excite to high electronic stages with relative ease. Fluorescence occurs when the excited fluorophore radiatively releases its energy during relaxation to come to ground state. The fluorophore can also return to ground state via a non-radiative pathway. The fluorescence energy transfer can

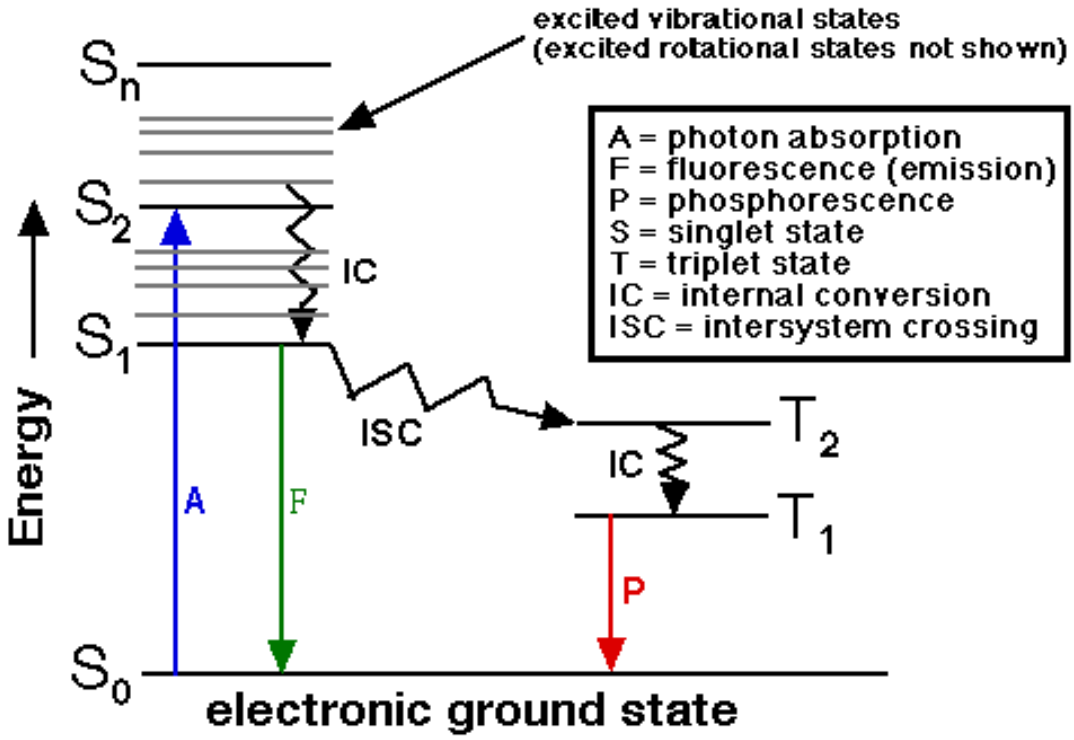

Fig. 5. Jablonski diagram illustrating the radiative relaxation of electrons resulting in fluorescence or phosphorescence, adapted from http://www.shsu.edu/chemistry/chemiluminescence/JABLONSKI.html.

be demonstrated by the Jablonski diagram (Fig.5). The ratio of number of photons emitted to the number of photons absorbed is termed as the fluorescent quantum yield, ϕ. The quantum yield depends upon the rates of radiative, and non-radiative relaxation of the fluorophore,

$$\phi = \frac{\Gamma}{\Gamma + K_{nr}} \tag{2.6}$$

where Γ is the first order rate constant for radiative relaxation and K_{nr} is the rate constant for non-radiative relaxation. Another important quantity is the fluorescent

lifetime τ which is the average time spent by the molecule in the excited state.

$$\tau = \frac{1}{\Gamma + K_{nr}} \tag{2.7}$$

For the fluorophore employed for optical tomography applications, τ is on the order of nanoseconds.

B. Methods of light propagation in tissue

Optical and fluorescence tomographic and spectroscopic measurements interrogate tissue volume by boundary excitation and boundary measurements of photon energy. As photons propagate in tissues not in straight line but via multiple scattering, both the photon intensity and the time of flight varies as a function of distance between the source and collection points available, as well as of the interior optical property distribution. Non-invasive techniques of probing the optical properties in tissue can be dividing into stationary approaches known as the continuous wave or CW imaging which measure only the light intensity at the boundary detectors and time dependent approaches which also seek to obtain the photon time of flight information in tissue. Time domain photon migration (TDPM) measurements and frequency domain photon migration measurements (FDPM) belong to the latter category. In the following sub-sections CW, TDPM, and FDPM approaches for interrogating tissue optical properties are described.

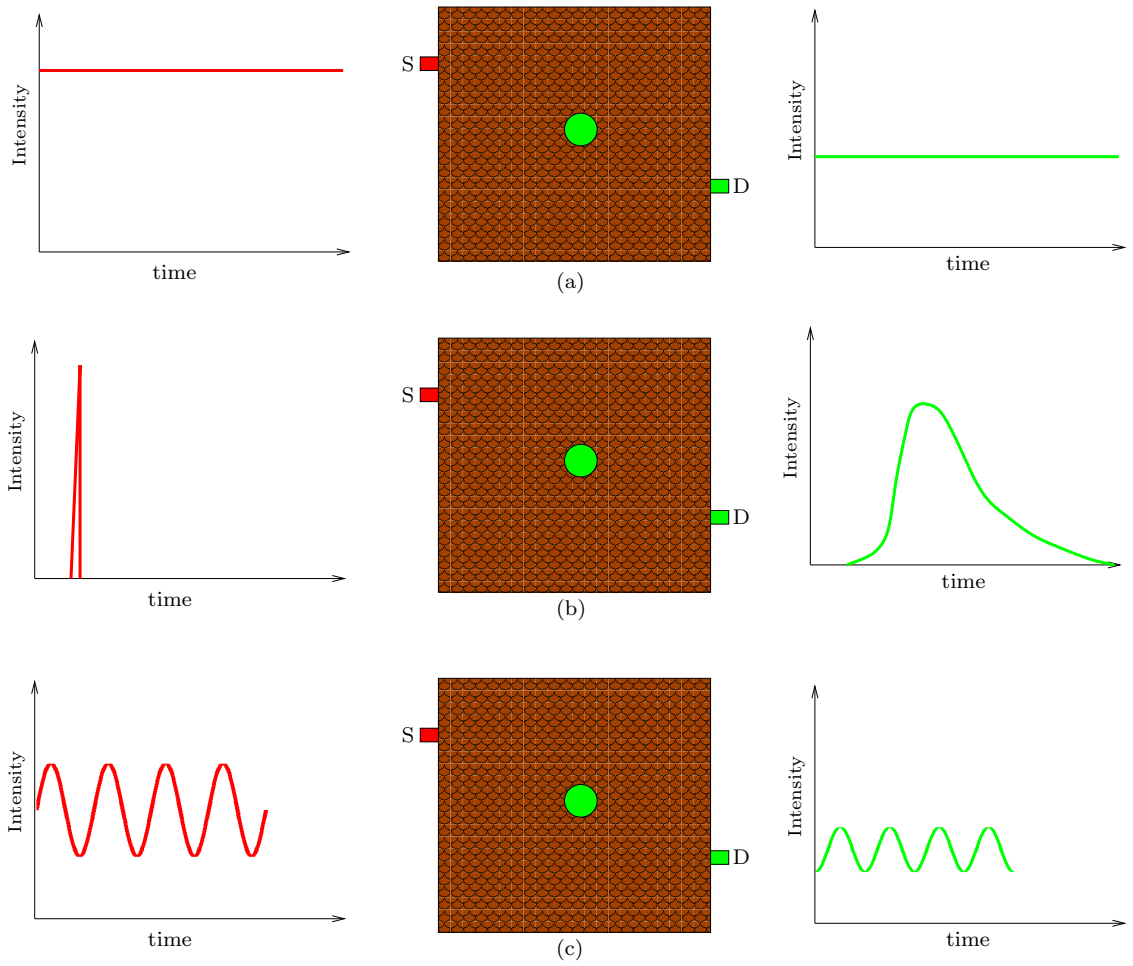

Fig. 6. Techniques for non-invasive interrogation of tissue optical(fluorescence) properties: (a) CW (b) TDPM (c) FDPM, Optical stimulation is provided at the boundary source (S) and measurements made at detector (D). Figures on the left illustrate the input signal and the figures on the right illustrate the measured light intensity profile for a fluorescent target embedded in the the tissue volume.

1. Continuous wave measurements

In the continuous wave measurement technique, a time invariant NIR light source at the excitation wavelength of the targeted fluorophore is applied at the tissue boundary. Excitation signal attenuates as it propagates into tissue to reach the fluorophore and the emitted fluorescent light also undergoes attenuation due to scattering and absorption by the time it is detected at the boundary detector. The detector measures a steady state fluorescent signal at a significantly lower intensity than the source excitation (Fig.6). The primary advantage of the CW measurement scheme is the simplicity of instrumentation and the ease and speed of acquiring measurements. Photons traverse a wide range of paths when travelling from the source to the detector, but in the CW approach only the average photon intensities at the detector locations are measured and time of flight information is averaged limiting the information available for reconstructing the optical property distribution in tissue from boundary measurements [49]. Hence a unique solution for scattering and absorption property distribution in tissue cannot be obtained from CW measurements [50, 51]. In fluorescence tomography CW measurements have been used for the reconstruction of fluorescence absorption coefficient [32, 33] provided the scattering coefficient of the tissue is known. Fluorescent molecules can exhibit changes in their decay kinetics and consequently in their lifetime depending upon their chemical environment, but CW techniques can not distinguish between the fluorescence intensity changes arising from the changes in fluorescence yield and from the changes in lifetime, furthermore they are not applicable for studying fluorescence targets exhibiting lifetime contrast. Other problems include the weighing of measurements towards illumination points

in case of imperfect fluorophore uptake in the target region.

2. Time domain photon migration measurements

Time domain photon migration approaches seek to directly measure photon time of flight information along with intensity at the detector locations. Excitation is provided by an impulse light source (pulse width of the order of pico-seconds) applied at the boundary of the domain. The detected pulse is reduced in height and is broadened during its propagation in tissue. The pulse broadening depends upon the photon path length distribution in tissue and the attenuation of the pulse depends upon the photon loss due to scattering and absorption. The time spread of the detected photon pulse is usually on the order of nanoseconds for sources and detectors position at the distance of several centimeters [52]. Time domain techniques for interrogating optical properties of tissue were first explored by Chance *et al.* [49]. Measurements are typically performed by photon counting techniques, time gated streak cameras, and by gated integrating devices. Ideally, time domain measurements provide the most complete set of information about the interior optical property and fluorescence distribution for tomographic reconstruction. However in practice the tail part of the detected pulse, which accounts for the photons with longest path lengths in tissue and is important for tomography, has the worst signal to noise characteristics. The low SNR behavior of large "time-of-flight" photons limits the attractiveness of time domain imaging, particularly in relation to the higher cost and complexity of instrumentation. Furthermore, the data acquisition time in time domain measurements is longer than in CW or FDPM measurements.

3. Frequency domain photon migration measurements

Frequency domain photon migration measurements are performed by applying a sinusoidal intensity modulated source at the tissue boundary. This photon density wave attenuates as it propagates in the tissue. The attenuated excitation wave is absorbed by the fluorophore and a modulated fluorescence emission wave is emitted which is detected at the boundary after undergoing further attenuation due to tissue scattering and absorption. The emitted wave is amplitude attenuated and phase shifted relative to the incident wave. The phase shift is the measure of average path travelled by the photons in reaching the detector. In case of fluorescence measurements, a major portion of the phase shift is caused by the fluorophore lifetime. Frequency domain measurements are the Fourier analogue of time domain measurements restricted to a single frequency. Typically frequencies of the order of $100MHz$ are employed which correspond to the temporal resolution in the nanosecond range. Information content of time domain data set can be created by employing a wide range of frequencies. Higher frequencies provide higher spatial and temporal resolution information. Frequency domain instrumentation is less complicated, and the setup, cost, and data acquisition time is lower than that of time domain measurement. As a result FDPM measurements are becoming the most popular way of investigating the tissue optical properties. Frequencies on the order of $100MHz$ are well suited for use with fluorescent dyes with lifetimes on the order of nanoseconds. FDPM schemes can detect both the fluorescence yield and lifetime contrast in tissues.

C. Mathematical modeling of photon transport in tissue

In general optical tomography schemes determine the interior distribution of tissue optical properties from boundary optical stimulation and measurements. The relation between boundary optical measurements and interior optical properties is non-linear owing to the multiple scattering behavior of photons in tissue. Thus, optical tomography cannot directly use the standard image reconstruction techniques of X-ray computed tomography. Most of the successful optical tomography algorithms perfrom model based iterative image reconstruction wherein a photon transport model is repeatedly solved with changing guesses of optical property maps, until the predicted boundary measurements match the experimentally observed values. Hence a photon transport model in tissue media is required. From the viewpoint of optical tomography a photon transport model should satisfy two requirements: 1) For known optical properties, model predictions should match experimentally observed light energy distributions in tissue to a reasonable degree of accuracy; and 2) computation time required for forward calculations should be on the order of minutes (preferably seconds) to allow the solution of three dimensional image reconstruction problems. Beer-Lambert law and Mie scattering theory are inadequate to explain tissue light propagation in a multiple scattering regime. Although a rigorous solution of Maxwell's equations will provide the solution for scattered light distribution in tissue for a given dielectric coefficient map, it is beyond the current computational capabilities to perform such calculations. Monte-Carlo methods can provide good solutions to photon transport problems in tissue but the time constraints involved make them infeasible for use in the solution to the inverse imaging problem. Radiative transport

theory provides a mathematically tractable platform for analyzing photon transport in turbid media by employing conservation arguments. Although radiative transport is not as rigorous as Maxwell's equations, it can explain a wide variety of tissue photon transport phenomena including polarized light propagation. [53, 54] Analytical solutions of radiative transport equation for problems of interest in optical imaging are not known and numerical solution approaches are cumbersome and time consuming. For highly scattering media such as breast tissue, wherein the length scales are much greater than the mean free path, photon transport is completely randomized. Diffusion equations can be derived as asymptotic approximations to radiative transport. Diffusion equations are popular as a forward modeling tool for optical and fluorescence tomography as they can be solved efficiently for most tissue imaging situations. In this section, we explain radiative transport and diffusion based modeling of NIR light propagation in tissue for fluorescence optical tomography.

1. Boltzmann radiative transport equation

Boltzmann radiative transport equation is a photon power balance equation. It relates the gradient of Radiance L at position $\mathbf{r}$ in the direction $\hat{s}$ to attenuation due to scattering and absorption and the photon influx from external source S and scattering from other directions $\hat{s}'$. [20]

$$\frac{\partial L(\mathbf{r},\hat{s},t)}{c\partial t}+\hat{s}\cdot\nabla L(\mathbf{r},\hat{s},t)+\mu_t L(\mathbf{r},\hat{s},t)=\mu_s\int_{4\pi}p(\hat{s},\hat{s}')L(\mathbf{r},\hat{s}',t)d\hat{s}'+S(\mathbf{r},\hat{s},t) \quad (2.8)$$

L denotes the time dependent radiance $(W/cm^2\cdot sr)$; c is the velocity of light in the medium; $\mu_t=\mu_a+\mu_s$ is the total attenuation(cm^{-1}); $S(\mathbf{r},\hat{s})$ $(W/m^3\cdot sr)$ is

the source of power at position $\mathbf{r}$ in the direction $\hat{s}$ at time t; p is the scattering phase function which denotes the normalized probability of a photon scattering from direction $\hat{s}'$ into the direction $\hat{s}$. If the refractive index of tissue is assumed to be isotropic then the scattering phase function depends only on the scattering angle θ and not on the direction of photon propagation [20], i.e. $p(\hat{s}, \hat{s}')$ can be replaced by $p(\hat{s} \cdot \hat{s}')\{= p(cos(\theta))\}$. Henyey-Greenstein phase function [55] is typically used for photon transport in turbid media [56]:

$$p(cos(\theta)) = \frac{1 - g^2}{2(1 + g^2 - 2gcos(\theta))} \tag{2.9}$$

Stationary radiative transport equation is obtained from eqn (2.8) by omitting the time dependent term, $\frac{\partial L(\mathbf{r},\hat{s},t)}{\partial t}$, and the frequency domain transport equation is derived by taking the Fourier transform of eqn (2.8). The quantity of interest for optical tomography is the fluence rate, which represents the total radiant power available at position $\mathbf{r}$. Fluence rate u is defined as the integral of radiance over all directions.

$$u = \int_{4\pi} L(\mathbf{r}, \hat{s}) d\hat{s} \tag{2.10}$$

Fluorescence generation and propagation is explained by introducing a second transport equation at emission wavelength. The coupled transport equation system for

modulated excitation light source is written in frequency domain as:

$$\hat{s}\cdot\nabla L_x(\mathbf{r},\hat{s},\omega)+[\frac{i\omega}{c_x}+\mu_{tx}]L_x(\mathbf{r},\hat{s},\omega)= \quad \mu_{sx}\int_{4\pi}p(\hat{s},\hat{s}')L_x(\mathbf{r},\hat{s}',\omega)d\hat{s}'+S_x(\mathbf{r},\hat{s},\omega) \tag{2.11}$$

$$\hat{s}\cdot\nabla L_m(\mathbf{r},\hat{s},\omega)+[\frac{i\omega}{c_m}+\mu_{tm}]L_m(\mathbf{r},\hat{s},\omega)= \quad \mu_{sm}\int_{4\pi}p(\hat{s},\hat{s}')L_m(\mathbf{r},\hat{s}',\omega)d\hat{s}'+S_m(\mathbf{r},\hat{s},\omega) \tag{2.12}$$

The subscript x represents the excitation field and m represents the emission field; $\mu_{tx}=\mu_{sx}+\mu_{axi}+\mu_{axf}$ is the total attenuation for the excitation field. μ_{axi} is the absorption due to endogenous chromophores and μ_{axf} is the absorption due to exogenous fluorophore. Analogously $\mu_{tm}=\mu_{sm}+\mu_{am}$ is the attenuation of the fluorescence emission field. Equations (2.11) and (2.12) are coupled by the isotropic emission source term S_m which depends upon the excitation fluence rate u and the fluorophore properties:

$$S_m=\frac{1}{4\pi}\frac{\phi\mu_{axf}}{1-i\omega\tau}u(\mathbf{r},\omega)=\frac{1}{4\pi}\frac{\phi\mu_{axf}}{1-i\omega\tau}\int_{4\pi}L(\mathbf{r},\hat{s})d\hat{s} \tag{2.13}$$

Here ϕ is the fluorophore quantum efficiency and τ is the fluorophore lifetime. Actual application of radiative transport equations requires the specification of boundary conditions at tissue-exterior interfaces. Traditionally no-return boundary condition has been used with the transport equation. This condition is valid for a refractive index matched boundary, However for tissue-air interface, a substantial amount of outward directed photon energy is reflected back into tissue in accordance with Snell's laws. Albedo boundary conditions have been proposed to account for diffuse reflectance at the boundary, wherein a specified portion of radiative flux at the

boundary is returned back. Klose *et al.* [42] have proposed direct application of Snell's laws to compute the reflected and transmitted radiance at the tissue-air interface for individual photon propagation directions. Solution schemes for radiative transport equations will be discussed in section 2.C.3. In the following section, the well known diffusion approximation to radiative transport is introduced.

2. Diffusion approximation

Diffusion equation for photon transport in tissue can be directly derived from Fick's law of diffusion and conservation statements on photon fluence rate. An alternative approach is to view diffusion equation as an approximation to the radiative transport equation. The latter approach can relate the photon diffusion coefficient to scattering and absorption coefficients. For a mostly scattering medium, diffuse radiance is almost isotropic and the radiance L can be expanded in terms of spherical harmonics of Legendre polynomials. If the expansion is limited to first two terms (P1 approximation), diffusion theory is obtained. Detailed derivations of diffusion equation are provided by Star [20] and Ishimaru [54]. The time dependent diffusion equation is written as:

$$\frac{1}{c}\frac{\partial u(\mathbf{r},t)}{\partial t} + \nabla \cdot [-D\nabla]u(\mathbf{r},t) + \mu_a u(\mathbf{r},t) = S(\mathbf{r},t) \tag{2.14}$$

$D = 1/3(\mu_a + \mu_s')$ is the photon diffusion coefficient and $\mu_s' = (1-g)\mu_s$ is the reduced or isotropic scattering coefficient. There are two main conditions for validity of diffusion approximation, 1) scattering should predominate absorption, i.e. $\mu_a/\mu_s << 1$; and 2) measurements should be taken at an adequate separation from the collimated source to allow isotropic scattering to predominate, A typical value of the distance

between source and detector reported in literature is $10\mu_s'$. Hence the diffusion equation is not valid in blood filled organs such as liver and spleen where absorption and scattering are on the scale and also in organs with large isotropic mean free pathlengths such as the white matter in brain and the synovial fluid in the joints. It is also not valid between points of illumination and collection closer than $10\mu_s'$. The diffusion equation can be written in frequency domain by taking the Fourier transform. Fluorescence generation and propagation is described by introducing a second diffusion equation. The coupled photon diffusion equations employed in fluorescence tomography are written as:

$$-\nabla \cdot [D_x(\mathbf{r})\nabla u(\mathbf{r},\omega)] + k_x u(\mathbf{r},\omega) = S_x(\mathbf{r}), \tag{2.15}$$

$$-\nabla \cdot [D_m(\mathbf{r})\nabla v(\mathbf{r},\omega)] + k_m v(\mathbf{r},\omega) = \beta_{xm} u(\mathbf{r},\omega), \tag{2.16}$$

where

$$D_{x,m} = \frac{1}{3(\mu_{ax,mi} + \mu_{ax,mf} + \mu'_{sx,m})}, \quad k_{x,m} = \frac{i\omega}{c} + \mu_{ax,mi}(\mathbf{r}) + \mu_{ax,mf}(\mathbf{r}),$$

$$\text{and} \quad \beta_{xm} = \frac{\phi\mu_{axf}}{1 - i\omega\tau(\mathbf{r})}.$$

Here we cast u, v as the fluence rates at excitation and emission wavelengths and $D_{x,m}$ are the corresponding photon diffusion coefficients. These equations are complemented by Robin-type boundary conditions. The outward fluence flux is related to the fluence at the boundary via a parameter γ which depends on the refractive

index mismatch at the boundary.

$$2\gamma D_x \frac{\partial u}{\partial n} + u = 0, \qquad 2\gamma D_m \frac{\partial v}{\partial n} + v = 0, \tag{2.17}$$

Zero boundary condition and extrapolated boundary conditions have also been used with diffusion equation. However Robin boundary conditions most accurately model the physics of light propagation on the tissue-air interface.

3. Forward modeling for radiative transport

Solution of radiative transport model to determine the detected fluence at the boundary for a given optical property map is an integral part of model based optical tomography schemes. A variety of solution methods have been proposed in the nuclear engineering community for solving the radiative transport equation which include the method of spherical harmonics, method of characteristics, and the discrete ordinates method with finite element or finite difference based spatial discretization. In the optical tomography community Chang *et al.* [43], Hielscher *et al.* [42, 44, 57, 58] and Dorn [59] have employed the radiative transport based forward model. Heilscher and coworkers have been active in the applications of different numerical techniques for the solution of radiative transport equations arising in optical and fluorescence tomography. Numerical solution of radiative transport equation is characterized by the fact that both angular and spatial discretization is needed to obtain the scattered radiance distribution, resulting in large computation times for even small optical tomography problems arising in small animal imaging. In this section we review predominant radiative transport simulation methods from an optical tomography

perspective. For a complete survey of numerical methods for radiative transport, reader is referred to reference [60].

a. Finite difference methods

Finite-difference discrete ordinate method is one of the most popular methods for solving the radiative transport equation and it has been evaluated by several optical tomography researchers. In discrete ordinates formulation radiative transport equation (2.8) is satisfied only on a finite set of angles $\{\hat{s}_n, n = 1, 2....N\}$. First the scattering phase function $p(\hat{s} \cdot \hat{s}')$ is expanded in a series of Legendre polynomials $P_l(\hat{s} \cdot \hat{s}')$:

$$p(\hat{s} \cdot \hat{s}') = \sum_{l=0}^{M} \frac{2l+1}{4\pi} b_l P_l(\hat{s} \cdot \hat{s}') \tag{2.18}$$

b_l are the Legendre expansion coefficients. for $b_l = g^l$, eqn (2.18) is reduced to Henyey-Greenstein phase function (2.9) [20]. The scattered internal source integral is replaced by a quadrature formula:

$$\mu_s \int_{4\pi} p(\hat{s}_n, \hat{s}') L(\mathbf{r}, \hat{s}', t) d\hat{s}' = \mu_s \sum_{n'=1}^{N} a_n p(\hat{s}_n, \hat{s}'_n) L(\mathbf{r}, \hat{s}'_n) \tag{2.19}$$

With the discrete ordinate assumption, the radiative transport equation is transformed into a set of N coupled differential equations with the coupling provided by eqn (2.19). Discretization in space can be performed by a variety of finite difference approximations. Hielscher and Alcouffe [58] have used the diamond differencing scheme while in recent work by Klose *et al.* [42] a step differencing scheme was employed. On a three dimensional spatial grid specified by grid coordinates (i, j, k), the fully discretized form of time independent radiative transport equation can be

written as a set of N equations:

$$(\hat{i}\cdot\hat{s}_n)\delta_x L_{i,j,k,n} + (\hat{j}\cdot\hat{s}_n)\delta_y L_{i,j,k,n} + (\hat{k}\cdot\hat{s}_n)\delta_z L_{i,j,k,n} + \mu_t L(i,j,k,n)$$
$$= S_{i,j,k,n} + \mu_s \sum_{n'=1}^{N} a_n p(\hat{s}_n, \hat{s}'_n) L(i,j,k,\hat{s}'_n) \quad \text{for} \quad n = 1, 2...N \tag{2.20}$$

$\{\hat{i},\hat{j},\hat{k}\}$ are the unit vectors in $\{x,y,z\}$ directions; $\{\delta_x,\delta_y,\delta_z\}$ represent discretized partial derivatives. Actual computation of discretized partial derivatives depends on the differencing scheme employed. Current state of the art radiative transport codes employ variants of linear discontinuous differencing schemes. Details and comparisons of differencing schemes are provided in the book bv Lewis [61]. Equation (2.20) can be written as a matrix system:

$$\mathbf{AL} = \mathbf{BL} + \mathbf{S} \tag{2.21}$$

The matrix $\mathbf{A}$ represents the left hand side of the eqn (2.20) and matrix $\mathbf{B}$ represents the internal scatter terms on the right hand side while the matrix S represents the external source. $\mathbf{L} = L_{i,j,k,n}$ is the solution for radiance for all the discrete ordinate directions. Equation (2.21) is efficiently solved by source iteration method. In the first step internal scattering term $\mathbf{B}$ is ignored:

$$\mathbf{AL_0} = \mathbf{S} \tag{2.22}$$

The preliminary solution $\mathbf{L_0}$ is then used to compute the internal scattering $\mathbf{BL_0}$ and the solution is updated by solving equation (2.21). The source iteration can be written as:

$$\mathbf{AL}^{k+1} = \mathbf{BL}^{k} + \mathbf{S} \tag{2.23}$$

For highly scattering media like tissue, source iteration procedure converges very slowly. The convergence speed can be enhanced by employing diffusion synthetic acceleration (DSA). In optical tomography Hielscher and Alcoufee [58] have used diffusion synthetic acceleration in isotropic scattering conditions. However the numerical schemes proposed by Heilscher *et al.* require the discretization level to be at the mean transport length scale for accurate solution. This limitation makes these differencing schemes prohibitively expensive for all but very small dimensional optical tomography situations. Klose *et al.* [44] have also solved the radiative transport model for fluorescence generation and propagation. Fluorescence radiance solution is obtained by first solving the excitation eqn (2.11) by the procedure discussed in this section and then repeating the source iteration procedure for fluorescence transport eqn (2.12) after substituting the excitation fluence $u = \int_{4\pi} L_x d\hat{s}$ to determine the fluorescence source.

b. Finite volume/element methods

Finite difference methods for solving RTE are limited to regular geometries, while finite element and finite volume methods can handle arbitrary geometries with unstructured meshes. The use of finite element methods for radiative transport calculations is a relatively recent phenomena. The finite element schemes for solving RTE in its native first order form are not yet available for problems arising in photon transport in highly scattering tissue media. Kanschat *et al.* [62] have proposed a fully adaptive three dimensional discrete ordinate finite element method for astrophysical calculations, but they have not demonstrated its performance for han-

dling highly scattering media. In the optical tomography community Abdoulaev and Hielscher [63] have proposed a finite element based solution for the second order even parity form of RTE, with the assumptions of isotropic scattering and isotropic external source. Ren and coworkers [64] have proposed a finite volume method for solving RTE. Their approach follows the same procedure as Klose *et al.* [42] except that spatial finite differencing steps are replaced by a finite volume based upwind differencing to arrive at equation (2.23). Wareing *et al.* [65, 66] have proposed a linear discontinuous finite element based differencing scheme for discrete ordinates solution of RTE. Their approach is available as a commercial software package ATTILA. ATTILA employs diffusion synthetic acceleration to speed up the convergence of source iterations and it can handle anisotropic scattering and directional external sources. Preliminary studies of the application of ATTILA to model NIR excitation and fluorescent light propagation in tissue media have yielded promising results. All the RTE solution approaches proposed in the optical tomography till now with the exception of out collaborative work with Wareing and coworkers, are either limited to isotropic scattering conditions or do not utilize diffusion synthetic acceleration to speed up the convergence of source iteration procedure. Both of these limitations will need to be addressed to enable the use of radiative transport equation as a viable forward model for optical or fluorescence tomography.

4. Forward modeling for diffusion approximation

Coupled diffusion equations (2.15), (2.16) describe the photon fluence distribution in tissue for a given excitation source and the distribution of optical properties in

tissue. These equations need to be solved repeatedly for iterative updates of optical property maps for solution of the inverse imaging problem. The repeated computation of diffusion equations comprises the bulk of the computational cost of the optical tomography process. The coupled diffusion equations belong to the class of linear elliptical partial differential equations and well studied numerical methods are available for their solution. Analytical solution methods are limited to cases with uniform optical property distributions and simple geometries. In this section a survey of numerical, analytical, and hybrid techniques for the solution of diffusion equations is reviewed.

a. Finite difference method

Solution of partial differential equations by replacing the derivative terms with difference approximations on a rectilinear grid is a classical numerical technique and descriptions are available in standard textbooks. Commercial solvers are available for solution of linear elliptic partial differential with a variety of boundary conditions. In the optical tomography community, the software package MUDPACK has been popular [38, 67]. Finite difference solvers are well researched and the solution schemes are computationally efficient. MUDPACK also provides a multigrid feature where the solution on a coarser grid to used to iteratively smooth the solutions on the finer grid to accelerate the convergence. The disadvantages of finite difference solvers include their inability to handle arbitrary domains and the restrictions of a fixed grid. For simulating near infrared light propagation in tissue media, finite difference meshes on the order of mean isotropic photon transport length (approx.

$1mm$) are needed. This results in a rapid increase in the number of grid points for clinically relevant tomography geometries, For example, Thompson *et al.* used a resolution of 129 grid points in each dimension for simulating NIR propagation in a $512cm^3$ cubical tissue phantom, requiring the solution for $129^3 = 2146689$ unknowns for each diffusion equation. Such simulations can take hours and are impractical for tomography algorithms requiring repeated solutions. Finite element methods avoid the pitfalls of finite difference methods by providing the ability to handle arbitrary geometries and the ability to generate discretizations tailored to specific problems. Finite element methods also enable the use of automatic adaptive mesh refinements to generate optimal numerical solutions to partial differential equations. The next section describes the application of finite element method to the solution of coupled photon diffusion equations for fluorescence optical tomography.

b. Finite element method

Finite element methods can be interpreted as the projection of the true solution on a finite dimensional space spanned by piecewise polynomials. We have employed a Galerkin scheme for the solution of coupled photon diffusion equations. The treatment in this section follows the notational conventions of Brenner *et al* [68]. The associated variational problem for the coupled photon diffusion equations can be written by multiplying the equations (2.15) and (2.16) by weighing functions $[w, z]$ and integrating over the domain Ω. The variational problem is:

Find $[u, v] \in H^1(\Omega)$ such that $\forall\ [w, z] \in H_0^1(\Omega)$

$$a(u,w) \equiv \int_\Omega [D_x \nabla u \cdot \nabla w + k_x uw] d\Omega + \int_{d\Omega} [\frac{\gamma}{2} uw] d\mathbf{s} = \int_{d\Omega} [S_x w] d\mathbf{s} \equiv f(w) \tag{2.24}$$

$$b(v,z) \equiv \int_\Omega [D_m \nabla v \cdot \nabla z + k_m uz] d\Omega + \int_{d\Omega} [\frac{\gamma}{2} vz] d\mathbf{s} = \int_\Omega [\beta_{xm} uz] d\Omega \equiv c_{xm}(u,z) \tag{2.25}$$

The space H^1 is the Sobolev space of continuous functions with continuous derivatives. The system of equations (2.24) and (2.25) has a unique solution for a smooth excitation source [68] which will be the case for our application. The variational problem is discretized with the finite elements $\{K, \mathcal{P}, \mathcal{N}\}$ as defined by Ciarlet [69]. The domain Ω is decomposed into distinct cells K(triangles,tetrahedrons,quads etc) such that the discretized domain $\Omega_h = \bigcup K$. $\mathcal{P}$ identifies the space of interpolating functions defined on K. For this application $\mathcal{P}$ will be chosen as the space of piecewise linear polynomials. $\mathcal{N}$ is the basis for $\mathcal{P}'$ (dual space of $\mathcal{P}$). It identifies the set of nodal variables which for linear interpolation will be the function values at vertice of K. The basis $\{\varphi_1, \varphi_2, \varphi_3 ..... \varphi_k\}$ is called the nodal basis of $\mathcal{P}$ if $N_i(\varphi_j) = \delta_{ij}$; k is the number of nodes in K. The variational problem can now be discretized. $[u, v, w, z]$ are interpolated over K in terms of the nodal basis and substituted into the equations (2.24) and (2.25).

$$u = \sum_{i=1}^{i=k} u_i \varphi_i\ ,\ v = \sum_{i=1}^{i=k} v_i \varphi_i\ ,\ w = \sum_{j=1}^{j=k} w_j \varphi_j\ ,\ z = \sum_{j=1}^{j=k} z_j \varphi_j \tag{2.26}$$

Where u_i, v_i, w_i, z_i are the nodal values. The discretized system over the element K can now be written as:

$$[w_k]^T(A_s^{ex} + A_m^{ex} + A_r^{ex})[u_k] = [w_k]^T F_K \tag{2.27}$$

$$[z_k]^T(A_s^{em} + A_m^{em} + A_r^{em})[v_k] = [z_k]^T B^{ex\rightarrow em}[u_k] \tag{2.28}$$

Where $[u_k], [v_k], [w_k], [z_k]$ are the vectors of nodal values of u, v, w, z; A_s^{ex} and A_s^{em} are the elemental stiffness matrices; A_m^{ex} and A_m^{em} are the elemental mass matrices; A_r^{ex} and A_r^{em} are the boundary matrices which are only evaluated for elements with at least one face on the boundary; F_K is the boundary excitation source vector; $B^{ex\rightarrow em}$ is the coupling matrix for the excitation and emission fields. The explicit forms of these matrices are:

$$A_s^{ex,m} = \int_K D_{x,m}\nabla\varphi_i \cdot \nabla\varphi_j d\Omega \ , \ A_m^{ex,m} = \int_K k_{x,m}\varphi_i\varphi_j d\Omega \ ,$$
$$A_r^{ex,m} = \int_{K \bigcap d\Omega} \frac{\gamma}{2}\varphi_i\varphi_j d\mathbf{s} \tag{2.29}$$

$$F_K = \int_{K \bigcap d\Omega} S_x\varphi_i d\mathbf{s} \ , \ B^{ex\rightarrow em} = \int_K \beta_{xm}\varphi_i\varphi_j d\Omega \tag{2.30}$$

The elemental linear systems obtained in equations (2.27) and (2.28) are then assembled for all the elements into a global linear system for the entire domain:

$$A_{global}^{ex}U - F = 0 \tag{2.31}$$

$$A_{global}^{em}V - B_{global}^{ex\rightarrow em}U = 0 \tag{2.32}$$

Where $A_{global}^{ex,m}$ are the global matrices for the excitation and emission equations; F is the global source vector for the excitation source; $B_{global}^{ex \rightarrow em}$ is the global coupling term; U *and* V are the vectors containing nodal values of excitation and emission fluence for the entire discretized domain Ω_h. Equations (2.31) and (2.32) can be solved with sparse direct methods or iterative schemes such as the conjugate gradient method [70].

c. Boundary element method (BEM)

Boundary element methods tries to save on computational costs of finite element method by discretizing the domain only on the boundaries of regions with different optical properties and using the analytical solutions within the regions themselves. While boundary element method can handle arbitrary shaped domains like the finite element method, it doesn't require for solution on large number of nodes resulting from the finite element discretization. In the optical tomography community BEM has been proposed by Heino *et al.* [71] for NIR optical imaging and Fedele *et al.* [72] for fluorescence optical imaging. Although BEM avoids the large dimensionality of FE method by avoiding internal discretizations, it is not generally applicable to optical tomography as it needs the knowledge of location of the fluorescence target to generate the discretization at the boundary of the fluorescent target. This information is not available *a priori* in the fluorescence tomography problem. Furthermore, fluorescence properties need to be uniformly distributed for the analytical solutions to work in the interior of the tissue domain. BEM can be a useful supplementary technique for the problems where fluorescence can be modeled as a perturbation on

a homogeneous background and the fluorescent target location has been determined by another tomographic technique. Readers are referred to the reference [72] for a detailed discussion of BEM in optical tomography.

d. Analytical solutions on complex domains

Analytical solutions for fluorescence and NIR propagation in tissues hold promise because of significant savings in computational cost of tomography algorithms. Analytical solutions are valid for homogeneous optical property distributions, however this disadvantage can be overcome by using perturbation based optical tomography schemes. The more significant disadvantage of analytical solutions is their inability to handle complex boundaries. Boundary element method is a rigorous numerical method to handle arbitrary boundaries, but it results in the generation of large non-sparse matrices which can not be inverted efficiently. Ripoll and coworkers [73, 74, 75] have proposed analytical approximation schemes, which avoid the need for boundary element discretizations for modeling NIR light propagation is homogeneous turbid media with complex boundaries. For the simple case of NIR optical tomography where only one diffusion equation is involved, on the closed volume Ω with arbitrary surface $\partial\Omega$ the solution for the fluence u at a detector location $\mathbf{r}_d$ on the boundary can be expressed in terms of the Green's function $G(\mathbf{r}_s, \mathbf{r}_d)$:

$$u(\mathbf{r}_d) = \frac{1}{4\pi} \int_{\Omega} \frac{S(\mathbf{r}')}{D} G(\mathbf{r}', \mathbf{r}_d) d\mathbf{r}' \tag{2.33}$$

where $S(\mathbf{r}')$ represents the source distribution and D is the diffusion coefficient. For a source located at $\mathbf{r}_s$ the Green's function inside the diffusive medium can be

represented in terms of its surface integral by using the Green's theorem. Detailed derivations are provided in reference [75]:

$$G(\mathbf{r}_s, \mathbf{r}_d) = g(\kappa|\mathbf{r}_s - \mathbf{r}_d|) - \frac{1}{4\pi}\int_{\partial\Omega}[C_{nd}D\frac{\partial g(\kappa|\mathbf{r}' - \mathbf{r}_d|)}{\partial n'} + g(\kappa|\mathbf{r}' - \mathbf{r}_d|)]\frac{\partial G(\mathbf{r}_s, \mathbf{r}')}{\partial n'}d\Omega \tag{2.34}$$

C_{nd} is the coefficient depending on the refractive index mismatch at the boundary; $\kappa = (\frac{i\omega}{c} + \mu_a)^{1/2}$ is the complex wavenumber of the photon density wave. $g(\kappa|\mathbf{r}_s - \mathbf{r}_d|)$ is the well known infinite media Green's function for the Helmholtz equation.

$$g(\kappa|\mathbf{r}_s - \mathbf{r}_d|) = \frac{exp[i\kappa|\mathbf{r}_s - \mathbf{r}_d|]}{|\mathbf{r}_s - \mathbf{r}_d|} \tag{2.35}$$

Equation (2.34) can be rigorously solved by the boundary element method which discretizes the integral on the right hand side by decomposing the surface into triangular or quadratic elements. Alternatively, the surface can be modeled by Kirchoff's approximation wherein the surface $\partial\Omega$ is replaced at each point by its tangent plane, so that the fluence u at each point $\mathbf{r}_p$ is replaced by the sum of infinite media solution and the photon density wave reflected by the local tangent plane at that point. The Kirchoff's approximation to the Green's function is written as:

$$G^{KA}(\mathbf{r}_s, \mathbf{r}_p) = g(\kappa|\mathbf{r}_s - \mathbf{r}_p) * [1 + R_{ND}(\mathbf{r}_p)] \tag{2.36}$$

R_{ND} is the reflection coefficient for diffusive waves. With this simplification eqn (2.34) can be solved by Fourier transform method. Kirchoff's method is limited to geometries with low curvature, hence it is suitable for clinical imaging situations with large tissue volumes. For small animal imaging, Ripoll *et al.* [73] have proposed iterative boundary methods which utilize image sources to model reflection at the

boundary. Analytical methods with complex boundaries can be suitable for the tomographic modeling for highly specific molecular targeting fluorophores, wherein the tissue background can be assumed to be homogeneous.

D. Adjoint/Sensitivity calculations for radiative transport and diffusion

Many optical tomography schemes are posed as optimization problems wherein an error functional representing the difference between observed boundary light measurements and the measurements predicted by a photon transport model is minimized. Local optimization methods require the computation of the gradient or first derivative of the error function with respect to the unknown optical properties. Alternative differential optical tomography schemes require the computation of Jacobian or sensitivity matrix of predicted photon fluence with respect to spatially distributed optical properties. A direct functional relationship between photon fluence and optical properties is available only for analytical solutions of diffusion or radiative transport equation. For general problems of light transport in heterogeneous media with complex boundaries, only numerical solutions are available and sensitivity computations can not be performed by straightforward differentiation. Typical computations required for fluorescence tomography schemes include the determination of the following quantities:

- Gradient of the error functional: $\mathbf{g}_E = \frac{\partial E}{\partial q_i}$, $E = f(v, z)|_{\sum \in \partial\Omega}$ is some function of observed(z) and predicted(v) fluorescence fluence at the measurement region $\sum$ on the boundary $\partial\Omega$; q_i is the fluorescence absorption or lifetime at the i_{th} node($i = 1, 2, 3..N$). In the discretized form $\mathbf{g}_E$ is a vector with length equal

to N.

- Jacobian matrix: $\mathbf{J} = \frac{\partial v_j}{\partial q_i}, j = 1, 2..M$, in the discretized form $\mathbf{J}$ is a matrix with dimensions of number of measurements(M) times the degrees of freedom of $q(N)$.

The following subsections describe the techniques used for the computations of gradient and Jacobian.

1. Difference schemes

The simplest scheme for gradient and Jacobian computation involves the application of difference formulas for the first derivative for a small perturbation Δq in the parameter q.

$$\mathbf{g}_E = \frac{E(q + \Delta q_i) - E(q)}{\Delta q_i} \quad i = 1, 2...N \tag{2.37}$$

$$\mathbf{J} = \frac{v_j(q + \Delta q_i) - v_j(q)}{\Delta q_i} \quad j = 1, 2..M, i = 1, 2...N \tag{2.38}$$

The computation of the gradient or Jacobian matrix by forward differencing requires $N + 1$ forward simulations. This limits the difference schemes to small phantom geometries with coarse discretizations [37, 38].

2. Adjoint schemes

Adjoint differentiation based schemes can perform the gradient and Jacobian computations in only two forward solutions. Adjoint formulation can be developed for both the radiative transport and diffusion computations in a concise manner if the

photon transport equations are written in operator notations. The following treatment is for diffusion equation but an analogous formulation applies for the radiative transport equation. These equations can be written in an abbreviated form by defining diffusion operators corresponding to the right hand sides of equations (2.15) to (2.16).

$$H_x u = S_x \tag{2.39}$$

$$H_m v = B_{xm} u \tag{2.40}$$

H_x is the excitation diffusion operator and H_m is the emission diffusion operator. B_{xm} is the operator which couples the excitation and emission fields. The Jacobian matrix and the error function gradient can be computed by the following differentiation procedure.

$$\mathbf{J} = \frac{\partial v_j}{\partial q_i} = \langle D, \frac{\partial v}{\partial q_i} \rangle \tag{2.41}$$

$$\mathbf{g}_E = \frac{\partial E}{\partial q_i} = \langle \frac{\partial E}{\partial v}, \frac{\partial v}{\partial q_i} \rangle \tag{2.42}$$

Here D is the Dirac matrix with dimensions of N x M, Each column is unity at the node corresponding to the detector location and zero everywhere else. The term $\frac{\partial E}{\partial v}$ is the analytical derivative of the error function with respect to the emission fluence v and it can be easily computed by straightforward differentiation. The notation $\langle \cdot, \cdot \rangle$ implies the standard inner product of vectors. The sensitivity term $\frac{\partial v}{\partial q_i}$ is computed by differentiating equations (2.39) and (2.40):

$$\frac{\partial v}{\partial q_i} = H_m^{-1}[B_{xm}\frac{\partial u}{\partial q_i} + \frac{\partial B_{xm}}{\partial q_i}u - \frac{\partial H_m}{\partial q_i}v], \quad \frac{\partial u}{\partial q_i} = H_x^{-1}[-\frac{\partial H_x}{\partial q_i}u] \tag{2.43}$$

Substituting equations (2.43) into equations (2.41), the Jacobian and gradient can be computed as:

$$\mathbf{J} = \frac{\partial v_j}{\partial q_i} = \langle D, H_m^{-1}[B_{xm}H_x^{-1}[-\frac{\partial H_x}{\partial q_i}u] + \frac{\partial B_{xm}}{\partial q_i}u - \frac{\partial H_m}{\partial q_i}v]\rangle \tag{2.44}$$

$$\mathbf{g}_E = \frac{\partial E}{\partial q_i} = \langle \frac{\partial E}{\partial v}, H_m^{-1}[B_{xm}H_x^{-1}[-\frac{\partial H_x}{\partial q_i}u] + \frac{\partial B_{xm}}{\partial q_i}u - \frac{\partial H_m}{\partial q_i}v]\rangle \tag{2.45}$$

The computation of Jacobian and gradient via equations (2.44) and (2.45) still requires $N+1$ forward solutions of coupled diffusion equations corresponding to perturbations in all the parameter nodes q_i. The definition of the adjoint operator can drastically reduce the computational cost of these calculations. If $\mathbf{a}, \mathbf{b}$ are vectors and A is a linear operator, then the adjoint identity states:

$$\langle \mathbf{a}, A\mathbf{b}\rangle = \langle A^*\mathbf{a}, \mathbf{b}\rangle \tag{2.46}$$

where the operator A^* is known as the adjoint of A, For real matrices the adjoint operator is the transpose operator. Substituting the definition of adjoint operator in eqns (2.44) and (2.45), we have:

$$\mathbf{J} = \frac{\partial v_j}{\partial q_i} = \langle [H_m^{-1}B_{xm}H_x^{-1}]^* D, -\frac{\partial H_x}{\partial q_i}u\rangle + \langle [H_m^{-1}]^* D, \frac{\partial B_{xm}}{\partial q_i}u - \frac{\partial H_m}{\partial q_i}v]\rangle \tag{2.47}$$

$$\mathbf{g}_E = \frac{\partial E}{\partial q_i} = \langle [H_m^{-1}B_{xm}H_x^{-1}]^* \frac{\partial E}{\partial v}, -\frac{\partial H_x}{\partial q_i}u\rangle + \langle [H_m^{-1}]^* \frac{\partial E}{\partial v}, \frac{\partial B_{xm}}{\partial q_i}u - \frac{\partial H_m}{\partial q_i}v]\rangle \tag{2.48}$$

Eqns (2.47) and (2.48) require the solution of one forward problem to determine $[u, v]$ and two adjoint solutions $H_m^{*-1}D$ and $H_x^{*-1}B_{xm}^*[H_m^{*-1}D]$. Since the diffusion operator is symmetric, hence the operators involved in the finite element discretization of diffusion equations $\{H_m, H_x, B_{xm}\}$ are self-adjoint. Thus adjoint problems are the same as forward problems with different right hand sides. However this is not true

for the radiative transport equations. Klose *et al.* have described the procedure for the computation for the error function gradient for radiative transport equations. Roy *et al.* [39, 76] and Klose *et al.* [57] implement the adjoint formulation in a reverse automated differentiation setting, which results in minimal computational effort (three times that of a forward solution) for the computation of error function gradient. Adjoint methods have made possible the application of large scale local optimization techniques to the field of optical and fluorescence tomography.

E. Fluorescence tomography approaches

The inverse problem in fluorescence enhanced optical tomography involves the determination of the fluorescence yield and/or lifetime map in the interior of the tissue domain from the boundary measurements of fluorescence emission. This section introduces the basic concepts and techniques for solving the inverse problem associated with fluorescence optical tomography. The following work will focus on the reconstruction of fluorescence absorption coefficient μ_{axf} which will be denoted by q. Analogous techniques apply for fluorescence lifetime tomography. The fluorescence tomography problem is formally defined as: Let Ω be the domain under consideration, $\partial\Omega$ is the boundary of the domain. Fluorescence measurements z are taken on a subset $\sum \subseteq \partial\Omega$ of the boundary for NIR sources$\{s\}$. Determine $q \in L^{\infty}(\Omega)$ The choice of the space $L^{\infty}(\Omega)$ restricts the unknown fluorescence absorption q within strict upper and lower bounds. In the following work, r_{si} denotes the position of ith source and r_{dj} denotes the position of jth detector; $z = \{z_j\}$ represents the boundary measurements vector; and M is the possible number of source-detector pairs. The

vector z is related with the fluorescence solution v via a measurement operator S, which selects the values at detector locations; $z = Sv$ holds for noise free measurements. The prevalent tomography schemes are broadly classified into two categories: perturbation based algorithms and nonlinear optimization based approaches. These categories are then further classified into algorithms with differing formulations and solution strategies.

1. Perturbation approach

Perturbation approaches were the earliest schemes applied for fluorescence yield imaging in turbid media. These approaches decouple the excitation and emission photon diffusion (or transport) equations by applying the first order Born approximation to the excitation photon fluence field and thus linearize the relationship between the boundary fluorescence measurements and the fluorescence absorption map q. That is the presence of a fluorescent target is not supposed to affect the excitation fluence distribution in the tissue. Perturbation schemes can be formulated both in integral and differential frameworks with identical results; however the integral method predominates in the literature [33, 77].

a. Formulation

Integral methods for solving the fluorescence tomography problem relate the boundary fluorescence light distribution to the interior fluorophore properties by an integral equation. The emission diffusion equation (2.16) can be reduced to Helmholtz form

by manipulating the Laplacian term:

$$-\nabla^2 v + k_m^2 v = \beta_{xm} u - \frac{\nabla D_m \cdot \nabla v}{D_m} \tag{2.49}$$

There is none or a very limited variation in the scattering coefficient of the tissue, which determines the D_m term; hence the second term on the right hand side of equation can be dropped. The Greens function corresponding to eqn(2.49) satisfies:

$$-\nabla^2 G(\mathbf{r}, \mathbf{r}') + k_m^2 G(\mathbf{r}, \mathbf{r}') = \delta(\mathbf{r} - \mathbf{r}') \tag{2.50}$$

The fluorescence emission fluence at a detector location $\mathbf{r}_d$ for an excitation source located at $\mathbf{r}_s$ can be expressed in terms of a convolution integral involving the Greens function $G(\mathbf{r}, \mathbf{r}')$ and the excitation fluence $u(\mathbf{r}', \mathbf{r}_s)$ For the i^{th} source and j^{th} detector:

$$v(\mathbf{r}_{dj}, \mathbf{r}_{si}) = \int_\Omega G(\mathbf{r}_{dj}, \mathbf{r}') \frac{\phi \mu_{axf}}{D_m(1 - i\omega\tau)} u(\mathbf{r}', \mathbf{r}_{si}) d\Omega \tag{2.51}$$

Eqn (2.51) is non-linear in $\mu_{axf} (\equiv q)$ as the excitation field u also depends on μ_{axf}. This equation is linearized via the first order Born approximation, where the true excitation fluence u is substituted by the excitation fluence u_0 computed for a uniform and known background μ_{axf} map. In the Born iterative method, the excitation field is recomputed after every update on the μ_{axf} map. Eqn (2.51) is discretized to

produce a linear system:

$$\begin{bmatrix} v(\mathbf{r}_d,\mathbf{r}_s)_1 \\ v(\mathbf{r}_d,\mathbf{r}_s)_2 \\ ... \\ ... \\ v(\mathbf{r}_d,\mathbf{r}_s)_M \end{bmatrix} = \begin{bmatrix} F_{11} & .. & .. & F_{1N} \\ .. & .. & .. & .. \\ .. & .. & .. & .. \\ .. & .. & .. & .. \\ F_{M1} & .. & .. & F_{MN} \end{bmatrix} \begin{bmatrix} q_1 \\ q_2 \\ .. \\ .. \\ q_N \end{bmatrix} \tag{2.52}$$

or

$$z = Fq$$

$$F_{ij} = \frac{G(\mathbf{r}_{di},\mathbf{r}_j)u(\mathbf{r}_{si},\mathbf{r}_j)\phi}{D_m(1-j\omega\tau)}\Delta \tag{2.53}$$

Here, M is the number of source-detector pairs and; Δ is the volume of each voxel and N is the number of voxels. Similar formulation can be developed for lifetime reconstructions. The unknown vector q is the sum of a known background part and the perturbation introduced by the heterogeneity:

$$q = q_b + \Delta q \tag{2.54}$$

So that, the linear system becomes:

$$F\Delta q = (z - Fq_b) \tag{2.55}$$

An equivalent linearization can be derived in a differential framework by considering the weight matrix F as the Jacobian or sensitivity matrix of the boundary fluorescence measurements. The boundary measurement vector z is approximated by a first

order Taylor expansion:

$$z(q) = z(q_b) + z'(q) \mid_{q_b} (q - q_b) \tag{2.56}$$

The Jacobian matrix is computed efficiently by applying the Born approximation (i.e. treating the excitation fluence u as a function of fixed background optical properties only) and an adjoint formulation as discussed in section-II.D.

b. Solution methods

Eqn (2.55) represents an underdetermined system; the predominant methods for solution are least squares (with Levenberg-Marquardt modification) and the Algebraic reconstruction technique. As F is not a square matrix, traditional inverse is not defined. Solution of the eqn (2.55) is written in terms of pseudo-inverse $F^{\#}$:

$$\Delta q = F^{\#}(z - Fq_b) \tag{2.57}$$

$$F^{\#} = F^T(FF^T)^{-1} \tag{2.58}$$

The inverse in eqn (2.57) is numerically unstable. Levenberg-Marquardt method handles this ill-posedness by scaling the diagonal terms with a regularization parameter β, so that the parameter update is determined from:

$$\Delta q = F^T(FF^T + \beta I)^{-1}(z - Fq_b) \tag{2.59}$$

Appropriate regularization parameter β can be chosen by generalized cross validation method. After each iteration the parameter map is updated by:

$$q^{k+1} = q^k + \Delta q^k = q_b \tag{2.60}$$

The weight matrix F is then recomputed with an updated excitation fluence u. Eqn(2.59) is used again to get a new update on q. The process is continued till the distance between the measured fluorescence fluence and the model prediction fall below a pre-specified tolerance:

$$\|z - Fq\|^2 \leq tol \tag{2.61}$$

Another approach to tomographic imaging is via Algebraic reconstruction. This method utilizes Kacmasz iterations for solving the system (2.55). Each row of the matrix F is used to the update the parameter map sequentially. For j^{th} row of F, the update is given by:

$$\Delta q^k = \Delta q^{k-1} - \frac{\Delta q^k \cdot F_k - (z - Fq_b)}{F_j \cdot F_j} F_j \tag{2.62}$$

An advantage of algebraic reconstruction is the avoidance of matrix operations with the consequent savings in computer memory utilization which is important for large values of M and N. Algebraic reconstruction is amenable to the use of *a priori* information about the parameter map. For example, it is very easy to incorporate non-negativity or bound constraints on the parameter in eqn (2.62) by projecting the update Δq^k onto the constraint set. In practice, absolute measurements of fluorescence emission fluence v are not available; Eqn (2.52) is then developed in terms of referenced measurements.

2. Optimization approach

a. Formulation

Fluorescence optical tomography can be posed as an optimization problem wherein the fluorescence absorption map which minimizes the distance between boundary fluorescence measurements and the fluorescence predicted by a photon transport model is sought. The optimization problem is:

$$\min_{q,u,v} \frac{1}{2}\|Sv - z\|^2 \quad subject \quad to \quad A(q)[u,v]^T = [S_x, o]^T \tag{2.63}$$

Here the semi-linear form A represents the coupled photon diffusion equations and S_x represents the boundary excitation source distribution. o is the null vector with dimension N corresponding to the absent external source for the emission diffusion equation. A is linear in excitation(u) and emission(v) fluence but is non-linear in the fluorescence absorption q. In practice A (size $2N$ x $2N$) is realized by the finite element or the finite difference model of coupled photon diffusion equations and the emission fluence can be obtained by implementing its inverse:

$$v = I_v[A(q)]^{-1}[S_x, o]^T, \quad I_v = \begin{bmatrix} O & O \\ O & I \end{bmatrix} \tag{2.64}$$

Where O is the null N x N matrix and I is the N dimensional identity matrix. The constrained optimization problem (2.63) can now be written as an unconstrained problem:

$$\min_q E(q) = \frac{1}{2}\|SI_v[A(q)]^{-1}[S_x, o]^T - z]\| \tag{2.65}$$

This formulation of the fluorescence tomography problem is also referred to as the output least squares. This is the predominantly reported method in the optical tomography literature. Forward model $A(q)[u,v]^T = [S_x, o]^T$ is always satisfied for the output least squares approach. A more general and elegant formulation for the fluorescence tomography problem can be derived by treating the model parameter q and the predicted data $[u,v]$ as independent quantities related by the forward model, by considering the constrained problem (2.63) directly. This constrained problem is then posed in a Lagrangian framework:

$$L([u,v],[\lambda^{ex},\lambda^{em}],q) = \frac{1}{2}\|Sv - z\|^2 + [\lambda^{ex},\lambda^{em}](A(q)[u,v]^T - [S_x,o]^T) \qquad (2.66)$$

Here, $[\lambda^{ex},\lambda^{em}]$ is the Lagrange multiplier vector corresponding to excitation and emission diffusion equation constraints. The Lagrange functional is then minimized with respect to state variables $[u,v]$, parameter variable q and Lagrange multipliers by Gauss-Newton or other Newton type optimization methods. In the constrained procedure the diffusion equations are not satisfied for the intermediate iterations, though they are satisfied at convergence.

b. Solution methods

Solution methods for optimization based approaches to fluorescence tomography are obtained by standard local optimization techniques. Although a few reports about the applications of global optimization schemes like evolutionary algorithms have been reported in optical tomography [78], they are not popular in fluorescence optical tomography because of the high computational demands of the global search

strategies. The local optimization schemes can be of the first order including the conjugate gradient or of second order such as Newton's, Gauss-Newton's or quasi-Newton schemes. All of these methods require the computation of the gradient of the optimization error function or the Jacobian matrix of sensitivities of the boundary fluorescence measurements with respect to the unknown fluorescence absorption. The iteration for updating the parameter map can be written as:

$$q^{k+1} = q^k + \alpha^k d^k \tag{2.67}$$

where d^k is the update direction depending on the type of optimization scheme chosen and α^k is the step size chosen by a line search strategy. The simplest first order method will be the steepest descent algorithm($d^k = -\mathbf{g}_E$). Steepest descent methods are suitable for only very small problems (10^2 unknowns) because of its slow convergence and small step size [79]. A better first order method is the conjugate gradient method. Conjugate gradient method can solve quadratic optimization problems with linear convergence rates and it does not require computation or storage of an N x N matrix like the Newton method. Conjugate gradient method searches along an orthogonal set of directions($d^0, d^1, d^2 ... d^k, \quad k < N$). The initial search direction is the steepest descent direction($d^0 = -\mathbf{g}_E$) and the other directions can be constructed from the previous directions by utilizing the classical Gramm-Schmidt technique of linear algebra [80]. The conjugate gradient search directions can be determined from the following formula:

$$d^{k+1} = -\mathbf{g}_E^{k+1} + \rho_k d^k \tag{2.68}$$

The correction factor ρ_k depends on the variant of the conjugate gradient algorithm chosen. Two popular choices are the Polak-Ribiere and Fletcher-Reeves algorithms:

$$\text{Polak-Ribiere} \quad \rho_k = \frac{\mathbf{g}_E^{(k+1)T}[\mathbf{g}_E^{(k+1)} - \mathbf{g}_E^k]}{\mathbf{g}_E^{(k)T}\mathbf{g}_E^k} \tag{2.69}$$

$$\text{Fletcher-Reeves} \quad \rho_k = \frac{\mathbf{g}_E^{(k+1)T}\mathbf{g}_E^{(k+1)}}{\mathbf{g}_E^{(k)T}\mathbf{g}_E^k} \tag{2.70}$$

According to a numerical study by Powell [81], Fletcher-Reeves method is superior for global convergence. However the Polack-Ribiere method provides a superior performance in many cases. Powell has suggested a modification to the Polak-Ribiere method which Arridge *et al.* [82] have used for optical tomography along with an inexact line search scheme. The primary advantage of conjugate gradient method for optical tomography is its efficient memory utilization as no matrices are created, stored or inverted. The convergence is slower than the Newton's method and the performance is sensitive to the line search scheme chose. The standard Newton's update direction can be written as:

$$d^k = -\mathbf{H}_E^{-1}\mathbf{g}_E \tag{2.71}$$

$\mathbf{H}_E = \partial^2 E/\partial q_i \partial q_j$ is the N x N Hessian matrix. Eqn(2.71) is rarely implemented directly as the computation of the Hessian matrix for realistic optical tomography problems ($N \cong 10^3$ to 10^4) is not possible. Even with an adjoint formulation the computation of Hessian will require $N + 1$ solutions of the coupled diffusion equations. Gauss-Newton(GN) method replaces the Hessian matrix with its first order approximation in terms of the Jacobian sensitivity matrix.

The Gauss-Newton direction is:

$$d^k = -[J^T J]^{-1} J^T \mathbf{b}, \quad \mathbf{b} = \partial E / \partial v \tag{2.72}$$

In most cases the GN Hessian matrix is illconditioned. As discussed in section-II.E-1 Levenberg-Marquardt modification can then be applied. GN approximation works well for the cases where the error functional is negligible near the optimal point, hence in presence of large measurement error, GN method convergence may slow. Alternatively, Quasi-Newton methods approximate the Hessian matrix by storing the gradient on previous iterations. Limited memory quasi-Newton methods are promising for optical tomography as they require the storage of only a few (typically 5) gradient vectors. For example the limited memory BFGS method iteratively updates the Hessian matrix in the following manner [83]:

$$\mathbf{H}_E^{k+1} = (I - \rho s_k y_k^T)\mathbf{H}_E^k(I - \rho y_k s_k^T) + \rho s_k s_k^T$$

Where $s_k = q^{k+1} - q^k$ and $y_k = \mathbf{g}_E^{k+1} - \mathbf{g}_E^k$. The performance of the quasi-Newton method is dependent on the quality of the line search procedure. The polynomial minimization based line search routine proposed by More, [84] performs better with quasi-Newton methods. For applications of quasi-Newton method to optical and fluorescence tomography, reader should consult the references [85, 42, 57]. Another way to apply the Newton's method to large dimensional optimization problems like optical tomography is the truncated Newton method with a finite difference approximation to the Newton direction. The Newton update direction can be obtained by

solving the following linear system:

$$\mathbf{H}_E^k d^k = -\mathbf{g}_E^k \tag{2.73}$$

Instead of exactly solving the eqn (2.73), a series of approximate solutions is generated by using the conjugate gradient method until the residual $\|\mathbf{H}_E^k d^k + \mathbf{g}_E^k\|$ drops below a preset tolerance (typically 10^{-3}). The Hessian-vector product is estimated by a finite difference formula:

$$\mathbf{H}_E d = \frac{1}{\sigma}[\mathbf{g}_E(q + \sigma d) - g(q)] \tag{2.74}$$

Eqn (2.74) avoids the storage of the Hessian matrix but requires the calculation of an additional gradient, which can be done efficiently by the adjoint differentiation method. The disadvantage of using the Newton's method is that it is not usually positive definite, hence the conjugate gradient method for determining the Newton update direction might not converge and the Newton update direction might not be a descent direction. Truncated Newton's method has been implemented in a stable manner by Roy with the help of a trust region framework [39]. With the advancement in computational capacities, local search methods are increasing in sophistication, however significantdisadvantagess remain: Newton's methods are sensitive to initial guess to the parameter map and they do notconvergee accurately unless fortified with some sort of *a priori* information about the optical property distribution. Prior information in the form of regularization, bounds on the parameters or in the form of probability distributions of parameter structure is explained in the next section.

3. Role of prior information

Optical or fluorescence tomography schemes are ill-posed in the sense that small errors in the measurement space can translate to huge variations in the image space of the unknown parameter. In discretized form, both the integral and differential or optimization based optical tomography functionals can be represented by a set of linearized equations $Fq = z$, where F is a matrix depending upon the formulation of the tomography problem. Ill-posedness of optical tomography is reflected by the large condition number or the presence ofinfinitesimall singular values of F, which result in the instability of inversion of F by direct or indirect (conjugate gradient, pseudo-inverse) means. In other words, the inverse operator $F^{\#}$ is unbounded. Prior information hastraditionallyy been used to solve these kinds of inverse problems. The following subsections describe the various methods of adding prior information to the optical tomography problem.

a. Regularization

Regularization process seeks to find an associated bounded inverse operator $F_{\beta}^{\#}$ which reduces to the unbounded operator $F^{\#}$ for $\beta = 0$ andstabilizess the solution with increasing values of β. Tikhonov regularization procedure modifies the tomography problem by solving for the parameter map minimizing $\|Fq - z\|^2 + \beta\|q\|^2$ where β is known as the Tikhonov regularization parameter [86]. The added regularization term prevents the generation of arbitrary large solutions. The regularization term can be generalized to include the derivatives of the unknown parameter map ($\|Fq - z\|^2 + \beta_1\|q\|^2 + \beta_2\|\nabla q\|^2 + \beta_3|\nabla^2 q\|^2 + ...$), thus enforcing additional smoothness on the

solution. These types of optical tomography schemes are successful in suppressing high spatial frequency errors in the reconstructed images. The crucial feature of regularization schemes is the choice of regularization parameter, it should not be too large to change the nature of the tomography problem and not too small to overcome the ill-conditioning of $F^{\#}$. L-curve and generalized cross-validation methods can be used to find the optimal regularization parameter at the cost of greatly increased computational expenditure.

b. Bound constraints

The unknown quantities in optical tomography are physical quantities, hence they are limited within strict lower and upper bounds. It makes sense to use this information instabilizingg the inverse imaging problem. Roy *et al.* [87] have utilized the simply bound constrained optimization framework for fluorescence optical tomography. By modifying an active set strategy, Roy reduced the number of unknown parameters in each iteration by fixing the parameters within an ϵ distance of the upper or lower bounds and optimizing only upon the free variables which lie within the bounds. This strategy results in both the regularization and the accelerated convergence of the image reconstruction. Joshi *et al.* [85] have used a traditional active set strategy without using the bounding parameter, ϵ, but with an adaptive finite element discretization and a limited memory quasi-Newton method [83] for fluorescence optical tomography. The use of prior information in optical tomography, whether by the choice of regularization or bounds can be elegantly represented by posing the image reconstruction problem in a Bayesian probability framework. The

next subsection discusses an important class of fluorescence tomography schemes which handle fluorescence tomography as a statistical estimation problem.

c. Bayesian optical tomography

Bayesian Analysis is a statistical procedure, which estimates parameters of an underlying distribution based on the observed distribution. We begin with a prior distribution which may be based on anything, including an assessment of the relative likelihoods of parameters or the results of non-Bayesian observations. In practice, it is common to assume a uniform distribution over the appropriate range of values for the prior distribution. Given the prior distribution, data is collected to obtain the observed distribution. Then the likelihood of the observed distribution is calculated as a function of parameter values, this is multiplied by the prior distribution, and normalized to obtain a unit probability over all possible values, in order to obtain the posterior distribution of the parameter. The mode of the posterior distribution is the parameter estimate. The above procedure can be implemented for inverse problem solution in the following manner:

Consider z as the measurement data vector (e.g. boundary fluence measurements) from an experiment and q is the parameter vector (fluorophore absorptioncoefficientt or lifetime) to be estimated. We consider a measurement of z as an experiment, which modifies the probability distribution of model parameters q. The inverse problem is equivalent to the determination of the conditional probability $p(q|z)$ of q given z. From Bayes theorem:

$$p(q|z) = p(z|q)\frac{p(q)}{p(z)} \tag{2.75}$$

Here $p(z|q)$ is the probability of measurement z conditioned to the known model q (forward problem). The probability $p(z)$ in is considered constant and ignored. The inverse image reconstruction problem can be posed as:

$$\underset{q}{\textbf{argmax}} \quad p(q|z) = \underset{q}{\textbf{argmax}} \quad p(z|q)p(q) \tag{2.76}$$

Forward problem term $p(z|q)$ incorporates the forward model solution and the noise characteristics of the measurements. The typical expression used is [88]:

$$p(z|q) \propto exp(-\sum_{j=1}^{M} \frac{1}{\sigma_j^2}[(Fq)_j - z_j]^2) \tag{2.77}$$

Above expression is for Gaussian noise with variance σ_j^2 of data point z_j. An alternative is the use ofPoissonn noise statistics often used in image processing. $(Fq)_j$ is the forward model solution for the j^{th} measurement z_j. The variance of the measurements can be determined statistically by using a large amount of prior data or it can be estimated from the physics of measurement process. Webb *et al.* [88] have estimated the $p(z|q)$ term by using the shot noise statistical model. Eppstein *et al.* [37] determined the error covariance directly from the measurement statistics. In that formulation σ_j^2 are the diagonal terms of the measurement error covariance matrix $E((z - \bar{z})(z - \bar{z})^T)$. Prior information term $p(q)$ is the probability density function of the model q without any knowledge of z:

$$p(q) = \int_{dataspace} p(q|z)dz \tag{2.78}$$

If we have no prior idea about the parameter map q, then $p(q)$ is uniform and is just another constant which can be ignored. Alternatively, the bounds of q may be

known, in that case:

$$p(q) = \begin{pmatrix} \frac{1}{ub-lb} & \text{if} \quad lb < q < ub \\ 0 & q < lb, q > ub \end{pmatrix} \tag{2.79}$$

This description of prior probability corresponds to the application of bound constrained image reconstruction. Many other distributions for $p(q)$ can be used:

- q is closer to a standard parameter map q^0

  $p(q) \propto exp(-c\|q - q^0\|^2)$

  For $q^0 = 0$, the above prior probability reduces to the application of standard Tikhonov regularization.

- q is smooth and hasminimumm first derivative

  $p(q) \propto exp(-c\|\nabla q\|^2)$

  This prior probability is same as regularization by bounded variation on the parameter.

The constant c signifies the certainty of the *a priori* knowledge and it corresponds to the regularization parameter β introduced in the section-II.E-3.c. Optimization error function for fluorescence optical tomography for normally distributed measurement errors and bounded uniform *a priori* distribution of unknown parameters can be obtained by taking the log of both sides of eqn (2.76):

$$\underset{q}{\textbf{argmax}} \quad log[p(z|q)] + log[p(q)] = \underset{lb<g<ub}{\textbf{argmin}} \quad \sum_{j=1}^{M} \frac{1}{\sigma_j^2}[(Fq)_j - z_j]^2 \tag{2.80}$$

The above cost function can be minimized by any of the local optimization methods introduced in the previous sections. Cost functions corresponding to different types

of regularization can be obtained by choosing different prior probabilities. Eppstein and coworkers [37, 38] have employed a Kalman filter algorithm for solving the least squares problem represented by eqn (2.76). The kalman filter is weighted damped recursive least squares estimator. The parameter update is given by:

$$\Delta q = [[\mathbf{J}^T(Q+R)^{-1}\mathbf{J} + P_{qq}^{-1}]^{-1} \cdot \mathbf{J}^T(Q+R)^{-1}] \cdot (Fq - z) \tag{2.81}$$

R is the measurement error covariance matrix and Q is the system or model error covariance. P is the parameter errorcovariancee. It is unknown in the tomography process and acts like spatially varying regularization. The kalman filter algorithm provides a way of generating updates on the P recursively, once an intital guess is provided. Eqn (2.81) can be derived from Bayes theorem eqn (2.76) for normally distributed parameter map andGaussiannmeasurementt and system errorstatisticss. [89]

CHAPTER III

ADAPTIVE FINITE ELEMENT BASED TOMOGRAPHY FOR FLUORESCENCE OPTICAL IMAGING IN TISSUE*

A. Introduction

Molecular Imaging is a rapidly advancing research area with the potential of providing early diagnosis and identification of the underlying biochemical causes of human diseases [5]. As near infrared (NIR) light can travel several centimeters in tissue, fluorescence enhanced NIR optical imaging promises to open new pathways for the characterization of biological processes in living animals at cellular and molecular levels.

In the past decade, several approaches have been proposed for fluorescence enhanced optical tomography involving the determination of the fluorophore yield and/or fluorescence lifetime distribution in the tissue from a finite number of boundary measurements. Due to the diffusive nature of photon propagation in tissue, fluorescence-enhanced tomography represents a non-trivial inverse problem. Initial efforts did not involve classical optimization but instead focused on approaches such as: perturbative localization [27, 28, 29], backprojection [30], Born Approximation [31, 32, 33], random walk theory [34], and more recently, fast fluorescence localization [35]. These approaches were successful in locating small fluorescent targets

---

*Reprinted with permission from "Adaptive finite element based tomography for fluorescence optical imaging in tissue" by A. Joshi, W. Bangerth and E.M. Sevick-Muraca, 2004, Optics Express, vol.12, 5402-5417. ©2004 by Optical Society of America

in otherwise homogeneous, small sample volumes. Other approaches to fluorescence tomography cast the image reconstruction problem as an optimization problem in which a least squares type minimization is performed in order to determine the fluorescence map which best predicts the measured boundary fluorescence distribution. Optimization approaches are more general in their scope and can handle heterogeneous backgrounds as well as large sample volumes albeit at increased computational cost. These approaches include algorithms based on Newton's or Newton-type optimization methods [36, 39, 40] and Bayesian nonlinear least squares approaches [37, 38, 41, 67].

The sensitivity of fluorescence enhanced imaging potentially rivals that of the conventional, but "gold-standard" molecular imaging using radiotracers [90]. Yet, the achievable resolution for fluorescence tomography is determined first by the signal to noise ratio, and secondly by the level of discretization. To date, the discretization level is selected *a priori* based on knowledge of the domain and/or computational constraints. Image quality can be improved by uniformly refining the level of discretization throughout the domain. However, this global refinement further increases the ill-posedness of the problem and results in insurmountable computational requirements by increasing the number of unknowns. For example, to achieve a resolution of one millimeter in a volume of one liter would require the use of 10^9 mesh points, a number that is clearly not achievable with today's computational technologies. In contrast, adaptive mesh refinement provides fine mesh resolution around target locations with coarser resolution in other regions to improve image quality, while maintaining solution stability and computational economy.

The outline of this article is as follows: In Section B the fluorescence tomography algorithm is described in a continuous function space setting and its discrete implementation with an adaptive mesh strategy is presented. Sections C and D detail the computational experiments conducted to demonstrate the adaptive tomography algorithm for reconstructing single and resolving dual fluorescence targets embedded in turbid media with a target to background ratio of $100:1$. Finally, the results are summarized in Section 5 and we show that Rayleigh resolution (i.e. the minimum distance between which two target can be resolved from one another) can approach the continuum limit using the adaptive strategy. To the best of the authors' knowledge, this contribution represents the first time that adaptivity has been used in optical tomography to address the issue of reconstructed image quality.

B. Methodology

In this section, the formulation for the nonlinear inverse problem of fluorescence tomography is developed in a continuous function space setting, allowing separate and independent discretization of the parameter map and the finite element mesh used to solve state/adjoint problems for the nonlinear update steps toward the optimal solution. The mesh refinement criteria and implementation described herein are based on the general framework developed in [91, 92].

1. Formulation

Under conditions of multiple scattering, the generation and propagation of diffuse fluorescence photon density waves from modulated, time-periodic sources can be

described by the following coupled system of diffusion equations [93]:

$$-\nabla \cdot [D_x(\mathbf{r})\nabla u(\mathbf{r},\omega)] + k_x u(\mathbf{r},\omega) = 0, \tag{3.1}$$

$$-\nabla \cdot [D_m(\mathbf{r})\nabla v(\mathbf{r},\omega)] + k_m v(\mathbf{r},\omega) = \beta_{xm} u(\mathbf{r},\omega), \tag{3.2}$$

where

$$D_{x,m} = \frac{1}{3(\mu_{ax,mi} + \mu_{ax,mf} + \mu'_{sx,m})}, \quad k_{x,m} = \frac{i\omega}{c} + \mu_{ax,mi}(\mathbf{r}) + \mu_{ax,mf}(\mathbf{r}),$$
$$\beta_{xm} = \frac{\phi\mu_{axf}}{1 - i\omega\tau(\mathbf{r})}.$$

Here, an index x denotes the excitation light field and m denotes the emission field; u, v are the complex-valued photon fluence fields at excitation and emission wavelengths, respectively;(Note that part of the literature uses the symbols Φ_x, Φ_m for these variables; u, v are used to avoid overly complicated expressions with many indices in the next sections.) $D_{x,m}$ are the photon diffusion coefficients; $\mu_{ax,mi}$ is the absorption coefficient due to endogenous chromophores; $\mu_{ax,mf}$ is the absorption coefficient due to exogenous fluorophores; $\mu'_{sx,m}$ is the reduced scattering coefficient; ω is the modulation frequency; ϕ is the quantum efficiency of the fluorophore; finally, τ is the fluorophore lifetime associated with first order fluorescence decay kinetics. The fluorescence generation mechanism is detailed in [93]. These equations are complemented by Robin-type boundary conditions on the boundary $\partial\Omega$ of the domain Ω:

$$2D_x \frac{\partial u}{\partial n} + \gamma u + S(\mathbf{r}) = 0, \qquad 2D_m \frac{\partial v}{\partial n} + \gamma v = 0, \tag{3.3}$$

where n denotes the outward normal to the surface and γ is a constant depending on the optical reflective index mismatch at the boundary [94]. $S(\mathbf{r})$ is the excitation boundary source. There is no source term for the emission boundary condition. Note that, here the NIR excitation source is modeled as a boundary condition. This is an approximation as the true isotropic source will be one scattering length below the illumination surface. This approximation is justified for a diffuse area illumination scheme [1] instead of the traditional point illumination by fiber optics and the finite element solutions of equations (3.1)–(3.3) match the experimentally observed boundary fluorescence [95]. The goal of fluorescence tomography is the reconstruction of a spatial map of coefficients $\mu_{axf}(\mathbf{r})$ and/or $\tau(\mathbf{r})$ from measurements of the fluences u, v on the boundary.

Instead of the (strong) formulation as a PDE above, equations (3.1)–(3.3) are posed in a weak variational form as is usual in finite element applications. The two equations are multiplied with arbitrary test functions $\zeta, \xi \in H^1$, integrated over Ω, and terms with second derivatives are integrated by parts. Here, H^1 is the Sobolev space of functions with integrable (weak) first derivatives (see Adams [96]). With this, the resulting variational equation reads:

$$A(q; [u, v])([\zeta, \xi]) = 0 \qquad \forall \zeta, \xi \in H^1, \tag{3.4}$$

where the semilinear form A is nonlinear in its first set of arguments and linear in the test functions. q denotes the set of unknown parameters, i.e. μ_{axf} and/or τ. In this work, we only consider $q = \mu_{axf}$. With $(\cdot, \cdot)$ denoting the L_2 inner product, the

definition of A reads

$$A(q;[u,v])([\zeta,\xi]) = (D_x\nabla u, \nabla\zeta)_\Omega + (k_x u, \zeta)_\Omega + \frac{\gamma}{2}(u,\zeta)_{\partial\Omega} + \frac{1}{2}(S,\zeta)_{\partial\Omega} + (D_m\nabla v, \nabla\xi)_\Omega + (k_m v, \xi)_\Omega + \frac{\gamma}{2}(v,\xi)_{\partial\Omega} - (\beta_{xm}u, \xi)_\Omega. \quad (3.5)$$

Note that $D_{x,m} = D_{x,m}(q), k_{x,m} = k_{x,m}(q), \beta_{xm} = \beta_{xm}(q)$.

The goal of the parameter identification problem is to find the set of parameters q for which the predicted boundary fluorescence measurements resulting from equation (3.4) best match actual measurements. The quantity to be minimized (i.e. the misfit between prediction and measurement) is then

$$J(q,v) = \frac{1}{2}\|v - z\|_\Sigma^2 + \beta r(q), \quad (3.6)$$

where the L_2 norm of the difference between the actual measurements, z, and the prediction of the emission fluence v on a part Σ of the boundary $\partial\Omega$ is minimized. In practice, z is interpolated between the pixels of an area detection system such as the gain modulated CCD camera. $r(q)$ is a Tikhonov regularization functional which penalizes certain undesirable aspects of solutions [86] and β is the regularization parameter. Information about measurement noise can be incorporated by using a different or weighted norm of the misfit [93].

In the past, optical tomography approaches have followed the output least squares formulation where the state variables u, v are taken to be dependent on the parameters q [82, 39]. In this work, however, we minimize the error functional J by treating $\{q, u, v\}$ as independent variables where their relationship is enforced by including the state equation as a constraint to the optimization prob-

lem [91, 92, 97, 98, 99]. We also deviate from the larger part of the literature in that we formulate the following steps in function spaces, rather than choosing the route of most optical tomography papers to first discretize state equation and objective function and then stating the optimization problem in the finite-dimensional space of matrices and vectors. While our approach leads to equations that at times look cumbersome, they are exactly equivalent to the matrix formulation if a fixed grid is used. However, they afford for the possibility of using different grids for different nonlinear iterations; in other words, we do not yet want to settle on a fixed discretization and therefore cannot choose the more usual matrix formulation.

With these considerations, the minimization problem reads:

$$\min_{q,u,v} \; J(q,v) \qquad \text{subject to} \quad A(q;[u,v])([\zeta,\xi]) = 0. \tag{3.7}$$

This constrained optimization problem can be considered in a Lagrangian framework where the Lagrangian is defined as:

$$L([u,v],[\lambda^{ex},\lambda^{em}],q) = J(q,v) + A(q;[u,v])([\lambda^{ex},\lambda^{em}]). \tag{3.8}$$

Here, $\lambda^{ex}, \lambda^{em}$ are the Lagrange multipliers corresponding to the excitation and emission diffusion equation constraints, respectively. For simplicity, the abbreviation of $x = \{u, v, \lambda^{ex}, \lambda^{em}, q\}$ is introduced so that the Lagrangian functional can be written as $L(x)$. The optimum is then characterized by a stationary point of the Lagrangian, i.e. the first order conditions:

$$L_x(x)(y) = 0 \qquad \forall y = \{\varphi^{ex}, \varphi^{em}, \psi^{ex}, \psi^{em}, \chi\}, \tag{3.9}$$

where $L_x(x)(y)$ is the Fréchet differential [100] of $L(x)$ and y denotes possible test functions. Eq. (3.9) can be expanded for all components of x:

$$L_u(x)(\varphi^{ex}) = A_u(q;[u,v])(\varphi^{ex})([\lambda^{ex},\lambda^{em}]) = 0, \tag{3.10}$$

$$L_v(x)(\varphi^{em}) = J_v(q,v)(\varphi^{em}) + A_v(q;[u,v])(\varphi^{em})([\lambda^{ex},\lambda^{em}]) = 0, \tag{3.11}$$

$$L_{\lambda^{ex}}(x)(\psi^{ex}) = A(q;[u,v])([\psi^{ex},0]) = 0, \tag{3.12}$$

$$L_{\lambda^{em}}(x)(\psi^{em}) = A(q;[u,v])([0,\psi^{em}]) = 0, \tag{3.13}$$

$$L_q(x)(\chi) = J_q(q,v)(\chi) + A_q(q;[u,v])(\chi)([\lambda^{ex},\lambda^{em}]) = 0. \tag{3.14}$$

Subscripts q, u, v, λ^{ex}, and λ^{em} indicate first order partial Fréchet derivatives of J or A. Equations (3.12)–(3.13) are the state equations in variational form. Equation (3.12) can be solved to provide the excitation fluence u which is then used to solve equation (3.13) to obtain the emission fluence v. Equations (3.10)–(3.11) are the adjoint equations defining the Lagrange multipliers $[\lambda^{ex},\lambda^{em}]$. Finally, equation (3.14) is the control equation.

The above set of coupled nonlinear equations is solved by Newton's method. The update direction for the kth iteration, $\delta x_k = \{\delta u_k, \delta v_k, \delta\lambda_k^{ex}, \delta\lambda_k^{em}, \delta q_k\}$, is determined from

$$L_{xx}(x_k)(\delta x_k, y) = -L_x(x_k)(y) \qquad \forall y, \tag{3.15}$$

where $L_{xx}(x_k)$ is the Hessian matrix of second derivatives of L at point x_k. These equations represent one condition for each variable in δx_k and when expanded read

as follows [91, 100]:

$$A_u(q_k;[u_k,v_k])(\varphi^{ex})([\delta\lambda_k^{ex},0]) + A_u(q_k;[u_k,v_k])(\varphi^{ex})([0,\delta\lambda_k^{em}]) \\ + A_{uq}(q_k;[u_k,v_k])(\varphi^{ex},\delta q_k)([\lambda^{ex},\lambda^{em}]) = -L_u(x_k)(\varphi^{ex}),$$

$$J_{vv}(q_k,v_k)(\delta v_k,\varphi^{em}) + A_v(q_k;[u_k,v_k])(\varphi^{em})([\delta\lambda_k^{ex},0]) + A_v(q_k;[u_k,v_k])(\varphi^{em})([0,\delta\lambda_k^{em}]) \\ + J_{vq}(q_k,v_k)(\delta q_k,\varphi^{em}) + A_{vq}(q_k;[u_k,v_k])(\varphi^{em},\delta q_k)([\lambda^{ex},\lambda^{em}]) = -L_v(x_k)(\varphi^{em}),$$

$$A_u(q_k;[u_k,v_k])(\delta u_k)([\psi^{ex},0]) + A_v(q_k;[u_k,v_k])(\delta v_k)([\psi^{ex},0]) \\ + A_q(q_k;[u_k,v_k])(\delta q_k)([\psi^{ex},0]) = -L_{\lambda^{ex}}(x_k)(\psi^{ex}),$$

$$A_u(q_k;[u_k,v_k])(\delta u_k)([0,\psi^{em}]) + A_v(q_k;[u_k,v_k])(\delta v_k)([0,\psi^{em}]) \\ + A_q(q_k;[u_k,v_k])(\delta q_k)([0,\psi^{ex}]) = -L_{\lambda^{em}}(x_k)(\psi^{em}),$$

$$A_{qu}(q_k;[u_k,v_k])(\delta u_k,\chi)([\lambda^{ex},\lambda^{em}]) + A_{qv}(q_k;[u_k,v_k])(\delta v_k,\chi)([\lambda^{ex},\lambda^{em}]) \\ + J_{qv}(q_k,v_k)(\delta v_k,\chi) + J_{qq}(q_k,v_k)(\delta q_k,\chi) + A_q(q_k;[u_k,v_k])(\chi)([\delta\lambda^{ex},0]) \\ + A_q(q_k;[u_k,v_k])(\chi)([0,\delta\lambda^{em}]) = -L_q(x_k)(\chi).$$

From Eq.s (3.10)–(3.11) one can infer that the Lagrange multipliers $[\lambda^{ex},\lambda^{em}]$ are proportional to $J_v(q;v)$. As a consequence, all terms involving $[\lambda^{ex},\lambda^{em}]$ become negligible near the optimal solution under conditions of low noise and can be dropped from the Hessian of the Lagrange functional, resulting in the simplified Gauss-Newton method. The equations for the Gauss-Newton method are then the same as above

with the exception that (i) the last terms on the left hand side of the first and second equations as well as (ii) the first and second term of the last equation are eliminated.

Once the search direction is computed from Eq. (3.15), the actual update is determined by calculating a safeguarded step length α_k:

$$x_{k+1} = x_k + \alpha_k \delta x_k. \tag{3.16}$$

The step-length α_k can be computed from one of several methods, such as the Goldstein-Armijo backtracking line search [39, 91, 92].

In many cases, bounds on the parameters q are available. For example, background or maximal uptake concentrations may be known. This information should be used in the inverse problem to stabilize its solution, as well as to enforce physically reasonable solutions. Thus, we incorporate bounds $q_0 \leq q(\mathbf{r}) \leq q_1$ using the scheme presented in [91, 92]. The method is a variation of the active set strategy, see [101]. At the beginning of each iteration, the set of parameters which lie at either of the bounds is identified. A first order approximation based on the gradient of the Lagrangian is used to determine whether the parameters are likely to move out of the feasible region. If so, then the update for these parameters is constrained to be zero. This method is computationally efficient since the determination of the likely direction uses only the information that is already available. Furthermore, enforcing a zero constraint on the update is equivalent to removing rows and columns from the Schur complement matrix described in the next section. In particular, no penalty terms need to be integrated into the objective function.

2. Discretization

In the previous section, we have formulated the Gauss-Newton method in function spaces. For carrying out actual computations, we discretize the Gauss-Newton equations with the finite element method and choose $\{\varphi_i\}$ as the basis functions for the state and adjoint variables u, v, λ^{ex}, and λ^{em}, and $\{\chi_i\}$ as the basis for the parameter q. Piecewise linear, continuous shape functions on hexahedral meshes for $\{\varphi_i\}$ and piecewise constant, discontinuous functions for $\{\chi_i\}$ are used. The discrete equations resulting from the Gauss-Newton modification of (3.15) are then represented by the following block system:

$$\begin{bmatrix} M & 0 & P^T \\ 0 & R & C^T \\ P & C & 0 \end{bmatrix} \begin{bmatrix} \delta p_k \\ \delta q_k \\ \delta d_k \end{bmatrix} = \begin{bmatrix} F_1 \\ F_2 \\ F_3 \end{bmatrix}, \tag{3.17}$$

where the updates for the primal and dual variables are abbreviated as $\delta p_k = [\delta u_k, \delta v_k]^T$, $\delta d_k = [\delta \lambda_k^{ex}, \delta \lambda_k^{em}]^T$. The blocks of the matrix are defined as

$$M = \begin{bmatrix} 0 & 0 \\ 0 & (\varphi_i, \varphi_j)_\Sigma \end{bmatrix}_{ij}, \quad R = \Big[\beta r''(q_k, \chi_i, \chi_j)\Big]_{ij}, \quad P^T = \begin{bmatrix} A_{global}^{ex} & -B_{global}^{ex \to em} \\ 0 & A_{global}^{em} \end{bmatrix}. \tag{3.18}$$

Here, P is the representation of the discrete forward diffusion model; A_{global}^{ex} and A_{global}^{em} are the global stiffness matrices associated with the excitation and emission diffusion equations; and $B_{global}^{ex \to em}$ is the matrix which couples the excitation and emission linear systems. The subscripts i, j in the preceding equations iterate over all degrees of freedom. The matrix C is defined as $C^T = [C_1, C_2]$ with its components

obtained by differentiating the semilinear form A in Eq. (B.4) with respect to the parameter q:

$$
\begin{aligned}
C_1 &= \left(\frac{\partial D_x(q_k)}{\partial q}\nabla u_k \cdot \nabla\psi_i, \chi_j\right)_{ij} + \left(\frac{\partial k_x(q_k)}{\partial q}u_k\psi_i, \chi_j\right)_{ij}, \\
C_2 &= \left(\frac{\partial D_m(q_k)}{\partial q}\nabla v_k \cdot \nabla\psi_i, \chi_j\right)_{ij} + \left(\frac{\partial k_m(q_k)}{\partial q}v_k\psi_i, \chi_j\right)_{ij} - \left(\frac{\partial \beta_{xm}(q_k)}{\partial q}u_k\psi_i, \chi_j\right)_{ij}.
\end{aligned}
\tag{3.19}
$$

The right hand side terms in Eq. (3.17) are the discretized components of the negative gradient of the Lagrangian:

$$
\begin{aligned}
F_1 &= \begin{bmatrix} -(D_x(q_k)\nabla\lambda_k^{ex}, \nabla\varphi_i) - (k_x(q_k)\lambda_k^{ex}, \varphi_i) - \frac{\gamma}{2}(\lambda_k^{ex}, \varphi_i)_{\partial\Omega} + (\beta_{xm}(q_k)\lambda_k^{em}, \varphi_i) \\ -(v_k - z, \varphi_i)_\Sigma - (D_m(q_k)\nabla\lambda_k^{em}, \nabla\varphi_i) - (k_m(q_k)\lambda_k^{em}, \varphi_i) - \frac{\gamma}{2}(\lambda_k^{em}, \varphi_i)_{\partial\Omega} \end{bmatrix}_i, \\
F_2 &= \begin{bmatrix} -\beta r'(q_k, \chi_i) - \left(\frac{\partial D_x(q_k)}{\partial q}\nabla u_k \cdot \nabla\lambda_k^{ex}, \chi_i\right) - \left(\frac{\partial k_x(q_k)}{\partial q}u_k\lambda_k^{ex}, \chi_i\right) \\ + \\ -\left(\frac{\partial D_m(q_k)}{\partial q}\nabla v_k \cdot \nabla\lambda_k^{em}, \chi_i\right) - \left(\frac{\partial k_m(q_k)}{\partial q}v_k\lambda_k^{em}, \chi_i\right) + \left(\frac{\partial \beta_{xm}(q_k)}{\partial q}u_k\lambda_k^{em}, \chi_i\right) \end{bmatrix}_i, \\
F_3 &= \begin{bmatrix} -D_x(q_k)\nabla\psi_i, \nabla u_k) - (k_x(q_k)\psi_i, u_k) - \frac{1}{2}(S_x, \psi_i)_{\partial\Omega} - \frac{\gamma}{2}(\psi_i, u_k)_{\partial\Omega} \\ -D_m(q_k)\nabla\psi_i, \nabla v_k) - (k_m(q_k)\psi_i, v_k) - \frac{\gamma}{2}(\psi_i, v_k)_{\partial\Omega} + (\beta_{xm}(q_k)\psi_i, u_k) \end{bmatrix}_i.
\end{aligned}
\tag{3.20}
$$

For large domains and fine discretization, the linear system Eq. (3.17) can be as large as several 100,000 unknowns. Furthermore, the matrix is generally indefinite, restricting the choice of available iterative linear solvers for determining the Gauss-Newton update directions. Thus, instead of solving Eq. (3.17) directly, we use an efficient solver based on the Schur complement developed in [91, 92]. By block

elimination, Eq. (3.17) is reduced to the following sequence of three equations:

$$\{R + C^T P^{-T} M P^{-1} C\}\ \delta q_k = F_2 - C^T P^{-T} F_1 + C^T P^{-T} M P^{-1}\ F_3, \tag{3.21}$$

$$P\ \delta p_k = F_3 - C\ \delta q_k, \tag{3.22}$$

$$P^T\ \delta d_k = F_1 - M\ \delta p_k. \tag{3.23}$$

The matrix $R+C^T P^{-T} M P^{-1} C$ is the Schur complement matrix of the Gauss-Newton system. Under practical conditions it is symmetric positive definite [91] and can thus be inverted efficiently by iterative solvers such as the conjugate gradient method. Furthermore, the Schur complement matrix is comparatively small (at most a few 1,000 to 10,000) with its size equivalent to the number of discretized parameters, rather than the number of parameters, state, and adjoint variables combined. Since the Newton method updates only approximates the direction to the optimal solution, it is not necessary to solve Eq. (3.21) exactly for each Newton step. The conjugate gradient iteration is thus stopped once the l_2 residual falls below a certain tolerance, for example 10^{-3} times its initial value. Consequently, this method is a variant of truncated or inexact Gauss-Newton methods [101].

3. Adaptive mesh refinement

The accuracy of finite element solutions of partial differential equations depends on the mesh width. This is reflected in *a priori* error estimates comparing the exact solution u and the numerically computed finite element solution u_h. For the simple

example of the Laplace equation, an *a priori* error estimate would be [102]:

$$\|u - u_h\| \leq C(u)\ h^2, \tag{3.24}$$

where h is the maximum mesh size and $C(u)$ is a constant that depends on the exact (and unknown) solution, the domain, and element shapes, but not upon the mesh width. Thus, the accuracy of the finite element solution can be increased by decreasing the maximum mesh size h. Similar estimates may be derived for the system in Eq.s (3.1)–(3.2). The drawback of *a priori* estimates is that the exact solution, and thus the numerical value of $C(u)$, is unknown, so that no quantitative bound on the error can be computed.

While Eq. (3.24) shows that it can be guaranteed that global mesh refinement reduces the error in the solution, this does not represent an efficient strategy in general. A fine mesh is only necessary where the solution varies greatly and where small cells are needed to accurately capture this variation. Since it is in general unknown in advance where these locations are, *a posteriori* error estimates have been derived in the mathematical community to provide criteria for local mesh refinement. These estimates use the computed solution u_h to not only provide a bound on the error $\|u - u_h\|$ without requiring knowledge of the exact solution u, but also to indicate on which cells the contribution to this error is largest. Thus, these estimates indicate the cells for which mesh refinement will be most beneficial, and conversely for which cells, mesh refinement will not yield a significant contribution to the reduction of the error. Using this process, the mesh on which u_h was computed can be appropriately refined, and the solution is computed again on the refined mesh; this process is iter-

ated until either the error estimate indicates that the requested accuracy is obtained, or computational resources are exhausted. The method in which only selected cells are repeatedly refined based upon an error indicator is commonly referred to as *adaptive mesh refinement*. For nonlinear problems, an additional advantage is realized by performing the initial Gauss-Newton updates on coarse meshes: finer and thus computationally more expensive meshes are employed only near the solution which reduces both the ill-posedness of the problem and the computational work in the initial steps.

A posteriori error estimates and adaptive mesh refinement have been extensively studied in the last two decades. See [103, 104] and the references therein for an overview. However, most of the previous work is tailored to model equations rather than parameter estimation problems with the exception of Molinari *et al.* [105, 106] for adaptive mesh refinement in electrical impedance tomography (EIT); see also [91, 92, 98, 107, 97, 108, 109, 110] for approaches in other fields.

In this work, we use two separate meshes that are adaptively refined. The first one is used for the discretization of state and adjoint variables u, v and $\lambda^{ex}, \lambda^{em}$, while the second one is used for the discretization of the parameter field q. The state/adjoint mesh is finer than the parameter mesh in order to avoid stability problems with the saddle point problem Eq. (3.17). In addition, and in accordance with the regularity requirements of the equation, we discretize state and adjoint variables using piecewise tri-linear finite elements, and the parameter with piecewise constant functions. Whenever Gauss-Newton iterations on these meshes have reduced the error function by a significant amount, both meshes are refined using *a posteriori* re-

finement criteria. In this work, the state and adjoint mesh is refined using a variation of the refinement criterion first derived by Kelly *et al.* [111]:

$$\eta_K^u = \frac{h}{24} \left\| [\partial_n u_h] \right\|_{\partial K}^2 , \qquad \eta_K^v = \frac{h}{24} \left\| [\partial_n v_h] \right\|_{\partial K}^2 , \qquad \eta_K = \alpha \eta_K^u + (1-\alpha)\eta_K^v, \quad (3.25)$$

where $[\partial_n u_h]$ is the jump of the normal derivative of the finite element solution u_h across the element boundary ∂K, and α is chosen so that the errors in the two variables are roughly weighted equally. In our implementation, we refine those 35% of elements with highest error indicator η_K and coarsen those 5% of elements with lowest errors in each cycle. Some other elements are also refined to maintain numerical stability of the solution.

The mesh for q is refined by computing, for each cell, a discrete approximation to the gradient of q weighted by the local mesh width [91]. Note that the choice of two separate meshes means that the first mesh can be fine close to the source where the excitation fluence greatly varies, while the second mesh will only be fine close to the fluorescent target and coarse everywhere else. The detailed derivation of error estimates can be found elsewhere [91, 97, 104].

4. Software implementation

A simplified block diagram of the tomography algorithm is shown in Fig. 7. At the beginning of the algorithm, all variables are initialized on coarse meshes (mesh level $m = 1$): state/adjoint variables are set to zero, while the parameter is set to the lower bound q_0 (the minimal background concentration). In each subsequent iteration, Gauss-Newton update directions are determined from Eq.s (3.21)–(3.23)

and all variables are updated after computating the step length. The program is terminated if the number of Gauss-Newton iterations exceeds the maximum number of iterations $k_{\max}$ or if the model misfit $\frac{1}{2}\|v - z\|^2_\Sigma$ is reduced below a prespecified threshold ϵ. For the results reported in this paper we used $k_{\max} = 40$ and $\epsilon = 10^{-15}$.

Mesh refinement is triggered if either (i) the Gauss-Newton step length α_k is less than a prespecified minimum step length $\alpha_{\min}$, or (ii) the nonlinear residual, $r_k = \|L_x(x_k)(\cdot)\|$, of the optimality condition (3.9) has been sufficiently reduced on the current mesh m, i.e. $r_k \leq \epsilon_{\text{mesh}} r_{k_m^0}$, where k_m^0 denotes the first iteration on mesh level m. In this work $\alpha_{\min} = 0.15$ and the error reduction threshold is $\epsilon_{\text{mesh}} = 10^{-4}$. Mesh refinement is followed by re-computation of synthetic measurements z on the new, finer mesh.

This scheme for fluorescence tomography with adaptive mesh refinement was implemented in C++ based on the deal.II finite element library [112]. Deal.II provides advanced object oriented design techniques and support for the complex data structures needed for adaptive finite element applications. While the current version of the software is used for an area excitation illumination geometry as previously published [1], the implementation is also suitable for point illumination geometries. Reconstructions were carried out on a dual processor (750MHz) Sun Sparc workstation with 3GB of RAM.

C. Computational experiments

Two computational experiments were performed to test the efficacy of the proposed algorithm: image reconstruction of (i) a single fluorescent target, and (ii) of two

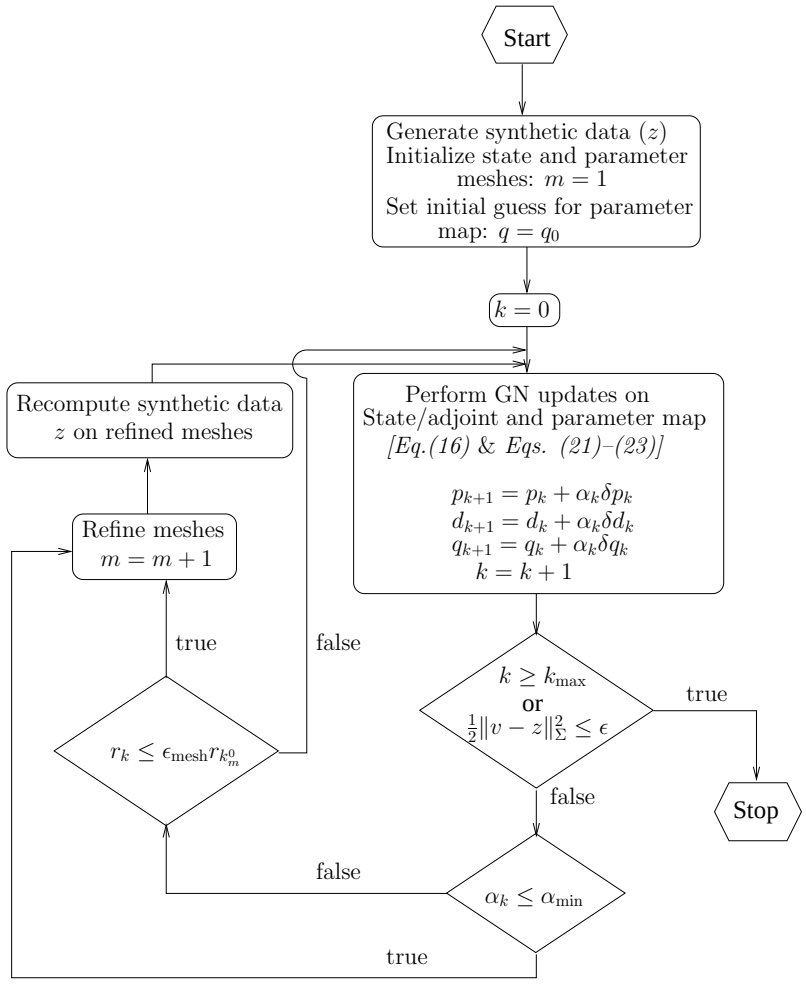

Fig. 7. Adaptive tomography algorithm. GN stands for Gauss-Newton; see Section 4 for a description of symbols.

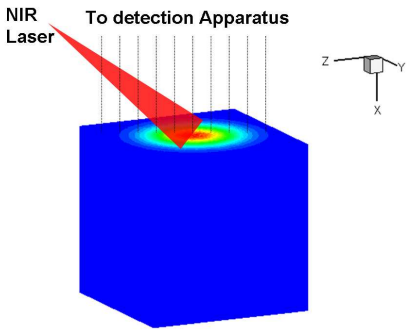

Fig. 8. Area illumination and area detection geometry employed by Thompson *et al.* [1]

closely spaced fluorescence targets of varying separation distance. The synthetic frequency-domain fluorescence data was generated on a simulated $8 \times 8 \times 8$ cm^3 cube illuminated by a simulated expanded laser beam with a Gaussian profile at the $x = 0$ plane, as shown in Fig. 8. This measurement geometry and phantom corresponds to experimental measurements previously reported [1]. Fluorescence phase and amplitude measurements were generated at the illumination surface in order to mimic the actual experimental data collection. Random Gaussian noise of zero mean and specified half width is then applied to these synthetic measurements.

1. Single fluorescent target

Data was generated for a $0.5cm$ diameter spherical target at a depth of $2.15cm$ from the illumination surface at an off-center position ($x = 2.15cm$, $y = 3.15cm$, $z = 3.15cm$). The absorption and isotropic scattering properties of 1% Liposyn solution were chosen to mimic the background of the phantom, corresponding to actual experimental measurements using a gain modulated ICCD camera system [1].

For the simulated background absorption coefficient, we chose $\mu_{axi} = 0.023cm^{-1}$ and $\mu_{ami} = 0.0289cm^{-1}$ [113]. The absorption coefficient due to fluorophore at the excitation wavelength was set to $\mu_{axf} = 0.5cm^{-1}$ in the target and $0.005cm^{-1}$ in the background. The emission wavelength absorption coefficient was $\mu_{amf} = 0.0506cm^{-1}$ in the target and $0.00506cm^{-1}$ in the background. The lifetime of the fluorophore was taken to be $\tau = 0.56ns$ and the quantum efficiency was $\phi = 0.016$ to match the corresponding properties of Indocyanine Green (ICG) dye used in experiments. The excitation wavelength for ICG is $785nm$ and the emission data is collected at $830nm$. The reduced scattering coefficient was taken as $\mu_s' = 9.84cm^{-1}$ in both the target and the background, and for this study was taken to be the same at excitation and emission wavelengths. Two percent random Gaussian noise was added to real and imaginary parts of the synthetic emission fluence solution at the measurement surface at $x = 0$.

2. Two fluorescent targets

Tomographic reconstructions were performed from synthetic data generated from the solution of Eq.s (3.1)–(3.3) for two closely spaced fluorescent targets to test the resolving ability of the adaptive inverse algorithm. Two spherical targets with diameter $0.4cm$ were placed at an edge to edge distance varying from $1cm$ to $0.1cm$, the latter of which is the continuum limit of the diffusion equation for the chosen optical properties. The depth of both targets was simulated to be $1.2cm$ from the illumination and measurement plane at $x = 0$. The optical properties of targets and background as well as the noise level remained the same as in the single target study.

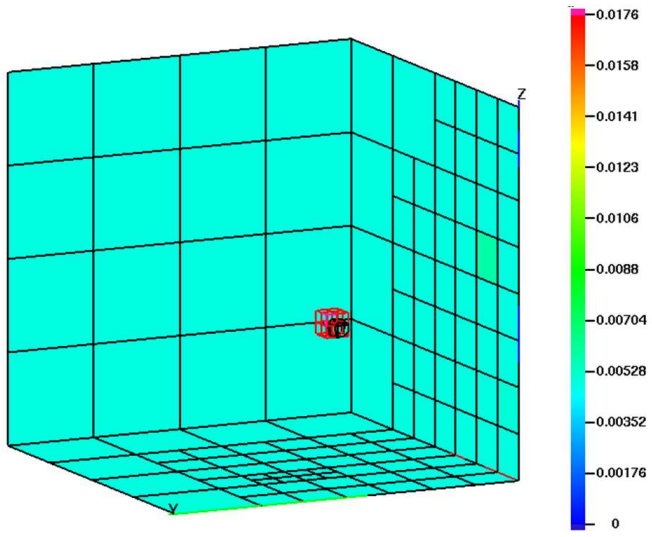

Fig. 9. Single target reconstruction: A black wire-frame depicts the actual target and colored blocks represent the reconstruction. Top 10% of the contour levels of μ_{axf} are shown.

D. Results

1. Single fluorescent target

Figure 9 illustrates the tomographic reconstruction for the single target case after 22 Gauss-Newton update steps utilizing approximately $2hrs$ of CPU time. The location of the target is reconstructed accurately. However, the magnitude $0.0176cm^{-1}$ of reconstructed μ_{axf} is lower than the actual value $0.5cm^{-1}$, which is an artifact of the L_2 regularization used ($r(q) = \frac{1}{2}\|q\|^2$, with a fixed value $\beta = 10^{-3}$). Figure 10 shows the evolution of state/adjoint and parameter meshes during the reconstruction process. The algorithm started with coarse initial meshes with 64 hexahedral elements. Five automatic mesh refinements were carried out by the algorithm. The final state/adjoint mesh consisted of $116,936$ nodes and was refined predominantly on the

illumination plane to accurately resolve the Gaussian NIR excitation source. The final parameter mesh had 1016 elements, mostly located around the reconstructed fluorescent target. A uniformly refined mesh with the same parameter mesh resolution as the adaptive mesh surrounding the target would have $32^3 = 32,768$ unknowns. The advantages of adaptive refinement for the reduction of the total number of unknowns and the improvement of resolution are obvious.

2. Two fluorescent targets

Figure 11 shows the tomographic reconstructions for targets separated by 1.0142, 0.6607, 0.3071, and $0.1657cm$. The reconstruction process was started with the same coarse state and parameter meshes as used in the single target case. A heuristic criterion was used to assess the reconstructions of the two targets: the top 10% contour levels of the μ_{axf} map were plotted and if two distinct maximum were visible, then the two targets were considered to be identified separately. The centroid of these two maxima was computed and treated as the reconstructed centroids. The centroids of the two targets was reconstructed accurately for target separations of $0.1657cm$ and greater, when the reconstructed targets begin to appear as one.

At a target spacing of $0.1cm$, the reconstruction is biased towards one of the targets, and no maximum associated with a second target is resolved at this distance (see Fig. 12). This is consistent with the fact that this separation is approximately the mean isotropic scattering length, below which the continuum assumption necessary for the validity of the diffusion approximation is violated. No image resolution below this threshold can be expected.

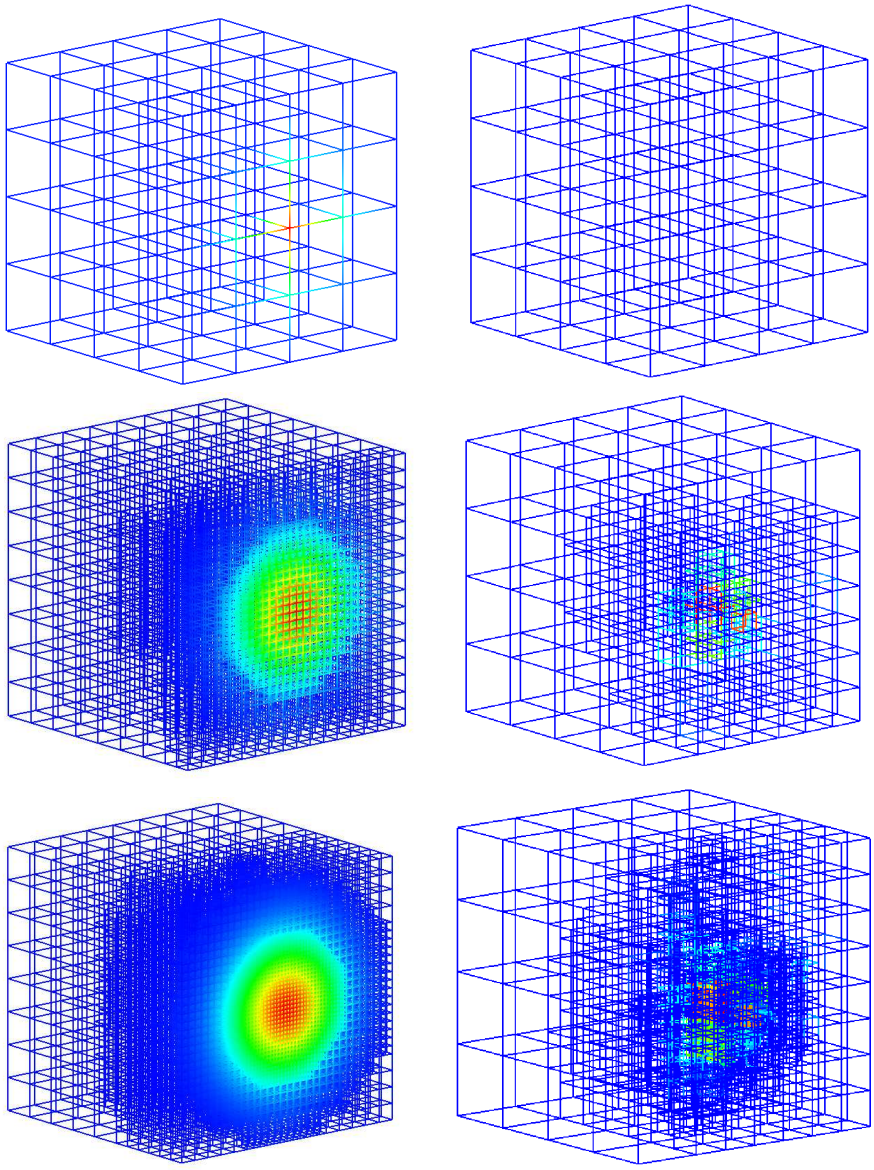

Fig. 10. Adaptive mesh evolution for state/adjoint (left) and parameter discretization (right). Meshes are shown at 1st, 11th and 22nd Gauss-Newton iterations.

TABLE II

Summary of results for dual fluorescent target reconstructions. d is the edge to edge target separation in cm; Iter. is the Gauss-Newton iteration for which the other results are reported;$\|q - q_{\text{true}}\|_2$ is the error in reconstructed parameter; $\frac{1}{2}\|v - z\|^2_\Sigma$ is the meausurement error; N_q is the number of elements (unknowns) in the parameter mesh.

d	Iter.	$\|q - q_{\text{true}}\|_2$	$\frac{1}{2}\|v - z\|^2_\Sigma$	$(x, y, z)_{\text{true}}$	$(x, y, z)_{\text{recovered}}$	N_q
1.0142	27	0.125	$2.58 \cdot 10^{-9}$	$(1.2, 3.15, 3.15)$	$(1.2, 3.13, 3.20)$	729
				$(1.2, 4.15, 4.15)$	$(1.2, 4.19, 4.22)$	
0.6607	18	0.127	$2.27 \cdot 10^{-9}$	$(1.2, 3.625, 3.625)$	$(1.4, 3.68, 3.625)$	1359
				$(1.2, 4.375, 4.375)$	$(1.2, 4.30, 4.30)$	
0.3071	27	0.119	$2.14 \cdot 10^{-9}$	$(1.2, 4.23, 4.23)$	$(1.1, 4.23, 4.27)$	1359
				$(1.2, 4.73, 4.73)$	$(1.2, 4.73, 4.71)$	
0.1657	28	0.118	$2.31 \cdot 10^{-9}$	$(1.2, 3.8, 3.8)$	$(1.3, 3.9, 3.8)$	638
				$(1.2, 4.2, 4.2)$	$(1.3, 4.1, 3.8)$	
0.1	25	0.121	$2.47 \cdot 10^{-9}$	$(1.2, 3.82, 3.82)$	$(1.2, 3.82, 3.82)$	1247
				$(1.2, 4.18, 4.18)$		

Table 2 summarizes the computational results for the dual target reconstructions, demonstrating the efficacy of adaptive mesh refinement for determining the maximum achievable resolution for a given experimental configuration in the presence of measurement noise. The reconstructed targets appear slightly closer than the actual separation as the target spacing is reduced. This can be explained by the merging of the fluorescence emission fields with decreasing distance when using only the reflectance data for image reconstruction as we have done here.

E. Conclusions

In this work, we have demonstrated an efficient adaptive finite element algorithm for fluorescence optical tomography. The algorithm is formulated in function spaces independent of any *a priori* discretization in order to allow for meshes to change as nonlinear (Gauss-Newton) iterations progress. Independent meshes have been used for the state/adjoint variables and the parameter map, and physical information about upper and lower bounds on the unknown parameters have been incorporated to improve the stability of the algorithm. The choice of separately adapted meshes (with the parameter mesh being coarser), different shape functions for the state and parameter variables, as well as the inclusion of bounds on the parameter and a Tikhonov regularization term yield an algorithm that is able to cope with the well known ill-posedness of optical tomography for comparable high resolution imaging with acceptable numerical effort in the presence of noise. The discretization scheme can be contrasted with that recently proposed by Huang *et al.* [114], in which prior information about the subdivision (discretization) of the domain is obtained from

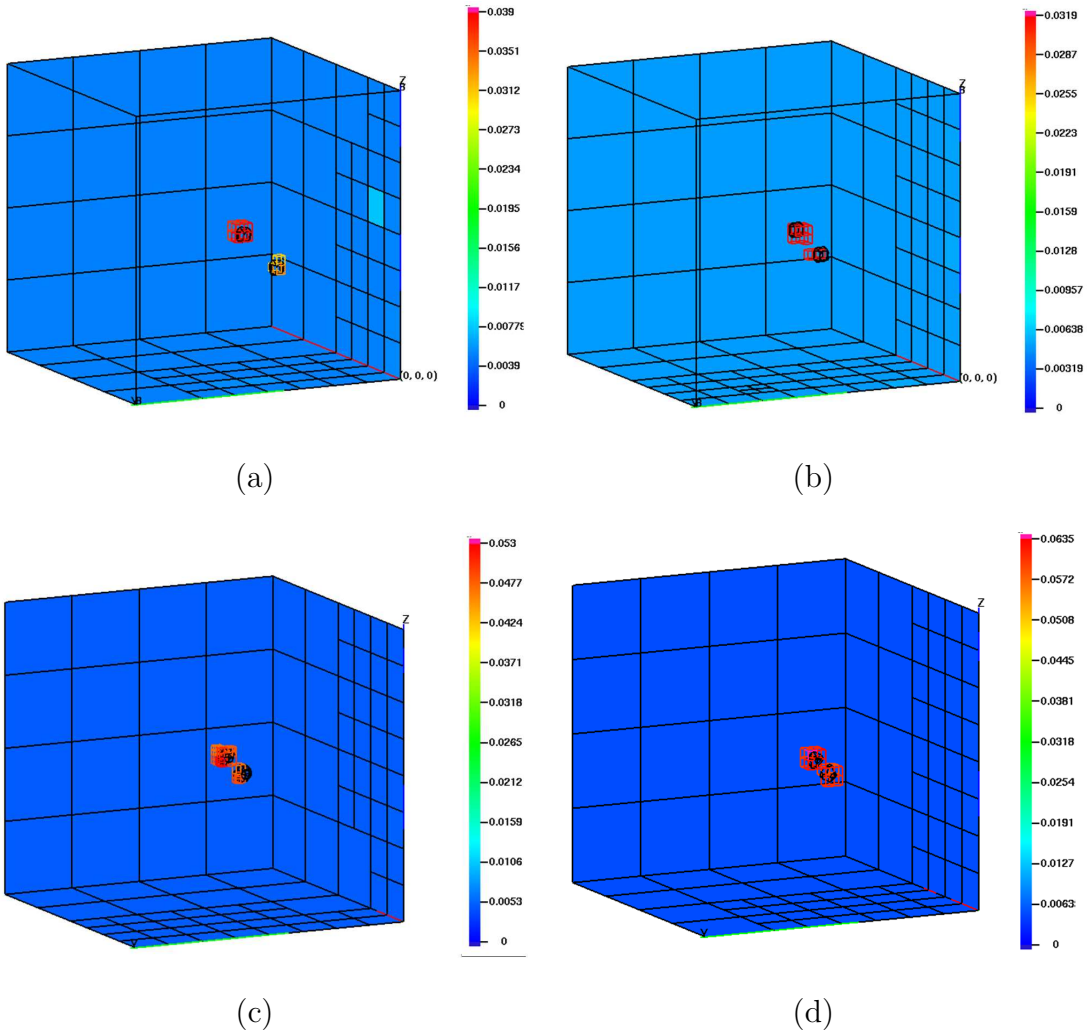

Fig. 11. Dual target reconstructions: A black wire-frame depicts the actual targets and colored blocks represent the reconstruction. Top 10% of the contour levels of μ_{axf} are shown. Edge to edge spacing: (a) $1.0142cm$, (b) $0.6607cm$, (c) $0.3071cm$, and (d) $0.1657cm$.

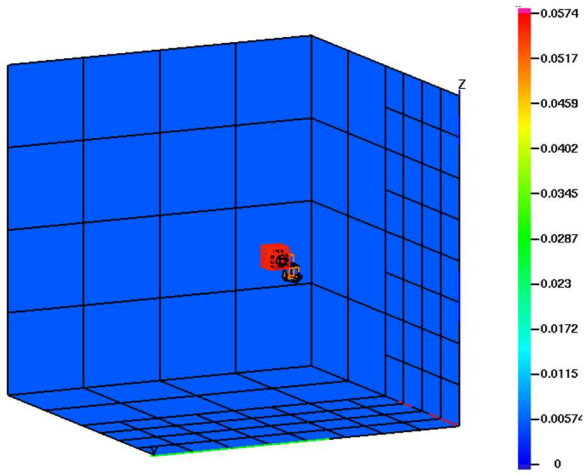

Fig. 12. Dual target reconstruction for $0.1cm$ target separation.

ultrasound images. While their strategy requires that the target is structurally dissimilar to the surrounding tissue to obtain meaningful information via ultrasound or MRI, our algorithm is able to find high resolution discretizations automatically by using the solutions on coarse grids to generate finer grids where necessary. To reiterate, the final number of unknowns (between 729 and 1359) is 25 to 40 times less than that necessary with the use of conventional finite element based optical tomography schemes for large tissue volumes while still retaining the resolution in the regions of interest. In addition, the reduced number of unknowns in our adaptive finite element scheme greatly reduces the ill-posedness of the inverse problem and thus aids in the quality of the reconstruction. Jiang *et al.* [115] have also proposed a dual and adaptive meshing scheme for diffuse optical tomography, However their scheme

doesn't implement automatic mesh adaptation with *a posteriori* error estimates.

We have demonstrated image reconstruction from frequency-domain fluorescence reflectance data arising from area-illumination. In comparison to circumferential point illumination measurements, reflectance measurements possess reduced information content for image reconstruction, but make the approach practical for patient imaging. This reflectance geometry and the associated 3-D adaptive finite element reconstruction algorithm could be pertinent for sentinel lymph node mapping as well as intraoperative localization of metastatic lesions (as used to track the progress of breast cancer). Our results provide the first report of a practical approach which may lead to high resolution molecular imaging in the clinic.

CHAPTER IV

FLUORESCENCE OPTICAL TOMOGRAPHY WITH AREA ILLUMINATION AND DETECTION

A. Introduction

Fluorescence tomography schemes have been proposed both for the pre-clinical small animal imaging applications [32, 116] and for the clinical imaging of large tissue volumes [41, 67, 38]. Typical fluorescence optical tomography schemes employ iterative image reconstruction techniques to determine the 3-dimensional fluorescence yield or lifetime map from boundary fluorescence measurements. A successful clinically relevant fluorescence tomography system will have the following attributes: 1) rapid data acquisition to minimize patient movement and discomfort, 2) accurate and computationally efficient modeling of light propagation in large tissue volumes, and 3) a robust image reconstruction strategy to handle the ill-posedness introduced by the diffuse propagation of photons in tissue.

Early fluorescence tomography schemes employed point-illumination and point-detection strategies with fiber optics [38, 77]. While these strategies can sample the tissue volume from multiple sides, the acquired data sets are sparse owing to the limitations on the number of fiber optics and the slow data acquisition rate. Ntziachristos *et al.* [33], and Godavarty *et al.* [41] employed a hybrid strategy to improve the data acquisition rate of the point-illumination and point collection schemes by imaging multiple detector fibers with a CCD camera. While Ntziachristos did this with CW measurements, Godavarty *et al.* did this with FDPM measurements. Even with

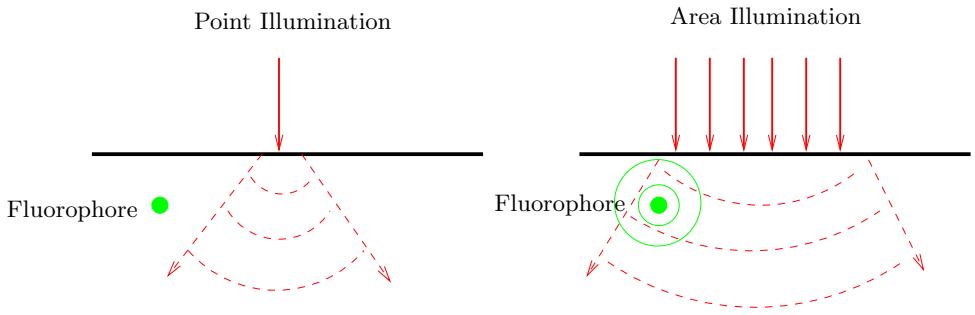

Fig. 13. Point illumination vs. area illumination.

the improvements in acquisition rate offered with simultaneous imaging of detectors, point illumination and point collection schemes might fail in large tissue volumes if sufficient excitation light is not delivered to the target fluorophore (Fig.13), Such is the case if the fiber optic delivering the excitation light do not illuminate the tissue volume adequately, In contrast, an area-illumination and area detection based fluorescence imaging setup can deliver excitation light over large tissue surfaces and thus acquire a dense set of fluorescence measurements rapidly. Furthermore, area illumination and area detection fluorescence measurements do not require physical contact with the tissue surface, making them attractive for clinical applications such as sentinel lymph node imaging to track breast cancer and melanoma.

The challenges in fluorescence tomography with area-illumination and area-detection measurements include : 1) developing measurement schemes to acquire fluorescence measurements with high SNR simultaneously over a large area, 2) ability to model light propagation in tissue from arbitrary expanded light beams incident on tissue and 3) managing the increased ill-posedness introduced into the

tomography problem, as only the reflectance measurements are available for image reconstruction. Recently Roy and coworkers [117] demonstrated fluorescence yield reconstructions from frequency domain area measurements made on a tissue phantom with an embedded fluorescence target. Their approach required a carefully designed finite element scheme to model the expanded laser excitation source. The fluorescence target depth was limited to $1cm$; and the target size was $1cm^3$; the image reconstruction problem involved over 30000 unknowns; and the algorithm required advanced optimization and regularization techniques to maintain stability and accuracy of the solution. Nonetheless, it was the first demonstration of tomography from area-illumination and area-detection methods.

We have previously reported a novel fluorescence tomography algorithm employing dual adaptive finite element meshes for area-illumination and area-detection measurement schemes [118], wherein separate meshes were employed for modeling light propagation in tissue and for describing the unknown fluorescence yield map. Both meshes adapt independently and automatically, hence area excitation illumination can be readily modeled and high resolution fluorescence images can be obtained with minimum computational expenditure. In this chapter, we present an integrated fluorescence tomography system wherein frequency domain fluorescence measurements made on a tissue phantom in area-illumination and area detection mode are utilized by the adaptive finite element based tomography algorithm to produce three dimensional images of fluorescent targets buried at the depths of $1cm - 2cm$ from the illuminated surface. Section-B describes the tissue phantom along with the instrumentation used for acquiring fluorescence emission and excitation source light

measurements and the adaptive tomography method used for image reconstruction. Section-C details the tomography results obtained for varying depths of fluroescent targets and the impact of adaptivity on the accurate modeling of photon propagation in tissue is illustrated. Finally section-D summarizes the implications of the presented work.

B. Materials and methods

The following subsections describe 1) the tissue phantom and fluorescent targets used for making measurements of fluorescent and excitation light, 2) the gain modulated image intensified CCD camera system and optical assembly, 3) data acquisition procedure for excitation and emission measurements and 4) the inverse image reconstruction scheme.

1. Tissue phantom

The phantom model was an $8cm$ side clear acrylic box filled with 1% Liposyn solution. The fluorescent targets used for this work were blown glass bulbs with an approximate outside diameter of $5mm$ and the internal diameters of $3mm - 4mm$ depending upon construction. The fluorescent targets were filled with $1\mu M$ Indocyanine Green(ICG) solution in 1% Liposyn which was stabilized with the addition of sodium polyaspartate [113]. The peak excitation and emission wavelengths of ICG are $785nm$ and $830nm$ respectively. The tissue phantom was illuminated at the top surface over a region of approximately $2.5cm$ diameter. The targets were positioned at the depth of $1cm$ or $2cm$ beneath the illumination surface by supporting them

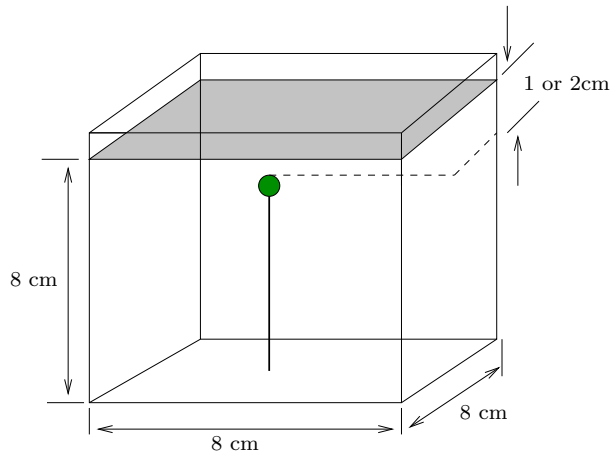

Fig. 14. Tissue phantom with fluroescent target.

with a fiber optic. Fig.14 illustrates the tissue phantom geometry.

2. Instrumentation

Fig.15 illustrates the homodyne gain modulated image intensified CCD camera system used for acquiring frequency domain optical measurements. The tissue phantom was illuminated by an expanded $785nm$ laser beam produced by a 70mW laser diode (Thorlabs, HPD 1105-9mm-D-78505). Measurements were acquired by a 1024 x 1024 pixel resolution $16-bit$ frame transfer CCD camera (Photometrics Ltd., series AT200, model SI512B, Tucson, AZ) which was coupled with an image intensifier (ITT Industries Night Vision, model FS9910C, Roanoke, VA). Fluorescence measurements were isolated by utilizing a $785nm$ holographic band rejection filter (Kaiser Optical Systems Inc., Ann Arbor, MI, model HNPF-75.0-2.0) and an $830nm$ interference bandpass filter (Image Quality, Andover Corp., Salem, NH, model 830.0-2.0). Optical filters were contained in a filter box assembly attached to the intensified CCD

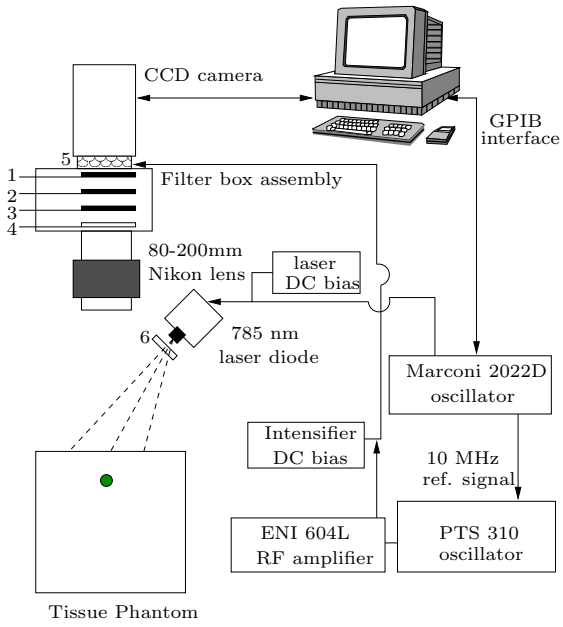

Fig. 15. Instrumentation for acquiring frequency domain fluorescence measurements in a homodyne mode. Numbered components include: 1. Neutral density filter (OD-3), 2. 785nm Holographic band rejection filter, 3. 830nm interference bandpass filter, 4. Linear polarizer, 5. Image intensifier, 6. Linear polarizer. Optical filters can be moved in and out of the filter box assembly to acquire measurements at excitation and emission wavelengths.

camera. Sliding trays carried the filters in and out of the light path to enable excitation and fluorescence emission light measurements. The top surface of the phantom was focused upon the image intensifier an $80mm-200mm$ Nikon zoom lens. The field of view attained was a $4cm$ diameter circle centered on the top surface of the phantom. Area illumination was contained in this area by utilizing a beam shaping lens placed in front of the laser diode. Frequency domain data was acquired by the homodyne procedure, wherein the laser diode and the image intensifier were modulated at $100MHz$ by two oscillators with a constant phase offset. A PTS-310 frequency synthesizer (Programmed Test Sources Inc., Littleton, MA, model 310M201GYX-53) modulated the photocathode of the image intensifier, and a Marconi signal generator (Marconi Instruments Ltd., Hertfordshire, England, model 2022D) modulated the laser diode. The oscillators were phase locked with a $10MHz$ reference signal. In the homodyne mode of data acquisition, phase of the image intensifier modulation is offset in 32 steps from the laser diode modulation to cover the full 2π cycle. At each phase delay 5 images were acquired. A sine curve is fitted to the images corresponding to the 32 phase delays with a fast Fourier transform and the amplitude and phase signal at each pixel is extracted. See Reynolds *et al.* [119] for a more detailed description of the multipixel frequency domain data acquisition instrumentation.

3. Data acquisition procedure

The instrumentation described in the previous section was used to obtain the frequency domain measurements at excitation and emission wavelengths by changing the optical filters and varying the parameters governing the CCD camera and image

intensifier operation.

a. Fluorescence emission measurements

For acquiring the fluorescence emission measurements, the signal intensity was increased by maximizing the aperture of the Nikon lens focusing the phantom surface onto the image intensifier and increasing the gain voltage of the microchannel plate of the image intensifier. The CCD camera images were binned down to 128 x 128 pixel and the image integration time was kept at 1200 milliseconds. The fluorescence amplitude and phase at each pixel was then computed by the homedyne data processing procedure detailed in the previous section. These measurements were performed for the fluroescent target depth of $1cm$ and $2cm$.

b. Excitation source characterization

As the surface excitation illumination was produced by expanding the laser beam from the laser diode using simple non-compensating optics, the amplitude and phase variation of the modulated excitation light incident on the phantom surface was unknown and should be considered in the image recovery process. [117] For measuring excitation light incident on the surface, the aperture of the focusing Nikon lens was minimized and the gain on the image intensifier was reduced to avoid saturating the CCD camera. A neutral density filter (OD-3 at $785nm$) was also used to further reduce the intensity of reflected excitation light. The integration time was maintained at 40 milliseconds.

The specularly reflected excitation light signal from the phantom surface was

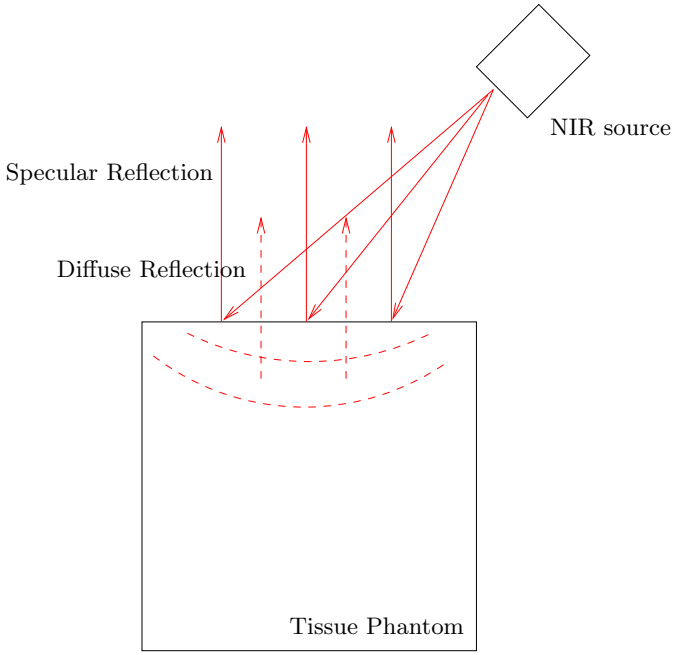

Fig. 16. Excitation light emitting out of phantom comprises of specular and diffuse reflectance components.

considered to be representative of the incident source. Yet the measured rreflectedexcitation light comprised of specularly reflected light and the diffusely reflected light (Fig.16). The specularly reflected component was isolated by utilizing two high efficiency (extinction ratio 10000:1) cross polarizers (Newport Corp., model 05P109AR.16, Irvine, CA). The polarizers were positioned at the laser diode output and image intensifier input. Multiple scattering causes the polarization to be randomized. One set of 32 phase dependent images was acquired with polarizers oriented in parallel. This set of images consisted primarily of the specularly reflected excitation light. Another set of images was acquired with polarizers oriented in

perpendicular. This set corresponded to the diffuse reflected excitation light. The correction for the multiply scattered excitation light was performed by subtracting the images acquired by orienting the polarizers in a perpendicular direction from the images acquired with polarizers in parallel. Finally excitation source amplitude and phase was isolated by performing the fast Fourier transform on the difference images. For more details on the excitation source characterization using polarizers, please consult Thompson *et al.* [1].

4. Inverse imaging scheme

As discussed in the previous chapters, fluorescence optical tomography is typically performed in a model based framework wherein a photon transport model in tissue is used to generate predicted boundary fluorescence measurements for a given fluorescence absorption map. The fluorescence absorption map is then iteratively updated until the predicted boundary fluorescence measurements converge to the actual experimentally observed fluorescence measurements. The coupled photon diffusion equations are an appropriate model for photon propagation in large tissue volumes:

$$-\nabla \cdot [D_x(\mathbf{r})\nabla u(\mathbf{r},\omega)] + k_x u(\mathbf{r},\omega) = 0, \tag{4.1}$$

$$-\nabla \cdot [D_m(\mathbf{r})\nabla v(\mathbf{r},\omega)] + k_m v(\mathbf{r},\omega) = \beta_{xm} u(\mathbf{r},\omega), \tag{4.2}$$

where

$$D_{x,m} = \frac{1}{3(\mu_{ax,mi} + \mu_{ax,mf} + \mu'_{sx,m})}, \quad k_{x,m} = \frac{i\omega}{c} + \mu_{ax,mi}(\mathbf{r}) + \mu_{ax,mf}(\mathbf{r}),$$
$$\beta_{xm} = \frac{\phi\mu_{axf}}{1 - i\omega\tau(\mathbf{r})}.$$

Here, subscript x denotes the excitation light field and m denotes the emission field; u, v are the complex-valued photon fluence fields at excitation and emission wavelengths, respectively; $D_{x,m}$ are the photon diffusion coefficients; $\mu_{ax,mi}$ is the absorption coefficient due to endogenous chromophores; $\mu_{ax,mf}$ is the absorption coefficient due to exogenous fluorophore; $\mu'_{sx,m}$ is the reduced scattering coefficient; ω is the modulation frequency; ϕ is the quantum efficiency of the fluorophore; finally, τ is the fluorophore lifetime associated with first order fluorescence decay kinetics. These equations are complemented by Robin-type boundary conditions on the boundary $\partial\Omega$ of the domain Ω:

$$2D_x\frac{\partial u}{\partial n} + \gamma u + S(\mathbf{r}) = 0, \qquad 2D_m\frac{\partial v}{\partial n} + \gamma v = 0, \tag{4.3}$$

where n denotes the outward normal to the surface and γ is a constant depending on the optical reflective index mismatch at the boundary [94]. $S(\mathbf{r})$ is the excitation boundary source. There is no source term for the emission boundary condition. Here the NIR excitation source is modeled as a boundary condition. For planar illumination, excitation source light can vary both in amplitude and phase across the illuminated surface, Hence $S(\mathbf{r})$ is a complex number. The goal of fluorescence tomography is the reconstruction of a spatial map of coefficients $\mu_{axf}(\mathbf{r})$ and/or $\tau(\mathbf{r})$ from measurements of the complex emission fluence v on the boundary. In this work we will focus on the recovery of μ_{axf} map from the boundary measurements. μ_{axf} will be denoted by q in the following paragraphs for notational simplicity. We had previously proposed a novel fluorescence tomography algorithm utilizing adaptive finite element methods [118]. In the following lines we briefly describe the formula-

tion of the scheme and its application to image reconstructions from experimentally obtained fluorescent measurements on the tissue phantom. The fluorescence image reconstruction problem is posed as a constrained optimization problem wherein an L_2 norm based error functional of the distance between boundary fluorescence measurements and the diffusion model predictions is minimized with the constraint that the coupled diffusion model is satisfied. In a function space setting this minimization problem reads as:

$$\min_{q,u,v} \; J(q,v) \quad \text{subject to} \quad A(q;[u,v])([\zeta,\xi]) = 0. \tag{4.4}$$

Here, the error functional $J(q,v)$ incorporates a least square error term over the measurement region Σ and a Tikhonov regularization term:

$$J(q,v) = \frac{1}{2}\left\|v - \sigma z\right\|_{\Sigma}^{2} + \beta r(q), \tag{4.5}$$

where $[u,v]$ represent the excitation and emission fluence; $q = \mu_{axf}$ denotes the unknown fluorescence map; σ is a scaling factor accounting for the unknown excitation source amplitude magnitude. For our instrumentation setup, σ was empirically determined to be 10^{-7}. β is the Tikhonov regularization parameter. In the studies reported in this paper the value of β was set as 10^{-12}. The constraint $A(q;[u,v])([\zeta,\xi]) = 0$ is the weak or variational form of the coupled photon diffusion equations in frequency domain with partial current boundary conditions, and with

test functions $[\zeta, \xi] \in H^1(\Omega)$:

$$A(q;[u,v])([\zeta,\xi]) = (D_x\nabla u, \nabla\zeta)_\Omega + (k_x u, \zeta)_\Omega + \frac{\gamma}{2}(u,\zeta)_{\partial\Omega} + \frac{1}{2}(S,\zeta)_{\partial\Omega} + (D_m\nabla v, \nabla\xi)_\Omega + (k_m v, \xi)_\Omega + \frac{\gamma}{2}(v,\xi)_{\partial\Omega} - (\beta_{xm}u, \xi)_\Omega. \quad (4.6)$$

The solution of minimization pproblem(4.4) is determined as a stationary point of the Lagrangian

$$L(x) = J(q,v) + A(q;[u,v])([\lambda^{ex}, \lambda^{em}]). \quad (4.7)$$

Here, $\lambda^{ex}, \lambda^{em}$ are the Lagrange multipliers corresponding to the excitation and emission diffusion equation constraints, respectively. For simplicity, we introduce the abbreviation $x = \{u, v, \lambda^{ex}, \lambda^{em}, q\}$. A stationary point of $L(x)$ is found using the Gauss-Newton method wherein the update direction $\delta x_k = \{\delta u_k, \delta v_k, \delta\lambda_k^{ex}, \delta\lambda_k^{em}, \delta q_k\}$ is determined by solving the linear system

$$L_{xx}(x_k)(\delta x_k, y) = -L_x(x_k)(y) \qquad \forall y, \quad (4.8)$$

where $L_{xx}(x_k)$ is the Gauss-Newton approximation to the Hessian matrix of second derivatives of L at point x_k, and y denotes the possible test functions. These equations represent one condition for each variable in δx_k. Once the search direction is computed from eqn (4.8), the actual update is determined by calculating a safeguarded step length α_k:

$$x_{k+1} = x_k + \alpha_k \delta x_k. \quad (4.9)$$

The step-length α_k can be computed from one of several methods, such as the Goldstein-Armijo backtracking line search [39, 91]. For carrying out actual computations, we discretize the Gauss-Newton equations with the finite element method. State and adjoint variables u, v, λ^{ex}, and λ^{em} are discretized and solved for on a mesh with continuous finite elements, while the unknown parameter map q is discretized on a separate mesh with discontinuous finite elements. Whenever Gauss-Newton iterations on these meshes have reduced the error function by a significant amount, both meshes are refined using *a posteriori* refinement criteria. In this work, the state and adjoint mesh is refined using a variation of the refinement criterion first derived by Kelly *et al.* [111]. The mesh for q is refined by computing, for each cell, a discrete approximation to the gradient of q, weighted by the local mesh width [91] and refining the cells with maximum variation in gradient. The choice of two separate meshes means that the first mesh can be fine close to the source where the excitation fluence greatly varies, while the second mesh will only be fine close to the fluorescent target and coarse everywhere else. The mesh refinement criteria and actual implementation of the reconstruction algorithm are described in reference [118]

C. Results and discussion

1. Excitation source extraction

Fig.17 illustrates the real and imaginary parts of the complex excitation source isolated and measured by utilizing cross-polarizers. The excitation source is normalized to have the maximum amplitude of one. The real and imaginary parts of the excitation source are used in the finite element simulations of coupled diffusion equations

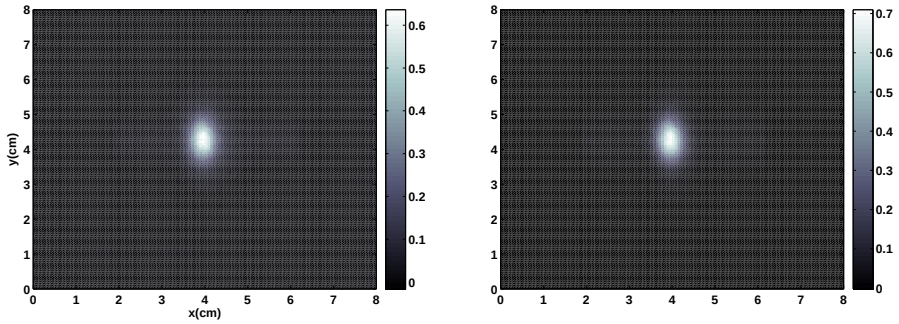

Fig. 17. Excitation source fluence: real(left image) and imaginary(right image) components.

for forward and inverse modeling of fluorescence light generation and propagation in the phantom. The mesh evolution at the illumination surface is illustrated in Fig.18 and demonstrates the ability of adaptive mesh generation to obtain optimal finite element discretizations for the experimental excitation source automatically. Simulation is started with coarse $1cm$ cells and after 5 adaptive mesh refinements a mesh well suited for accurately modeling the measured incident excitation light.

2. Measurements and model match

As described in sections-B,C complex fluorescence measurements were acquired by placing fluorescent targets at depths of $1cm$ and $2cm$ from the illuminated surface. Simulated fluorescence measurements were obtained from an adaptive finite element solution of the coupled diffusion equations (4.1), (4.2) for the experimental phantom and fluorescent target geometry. The experimentally observed fluorescence measurements should agree with the simulated measurements to a reasonable degree for

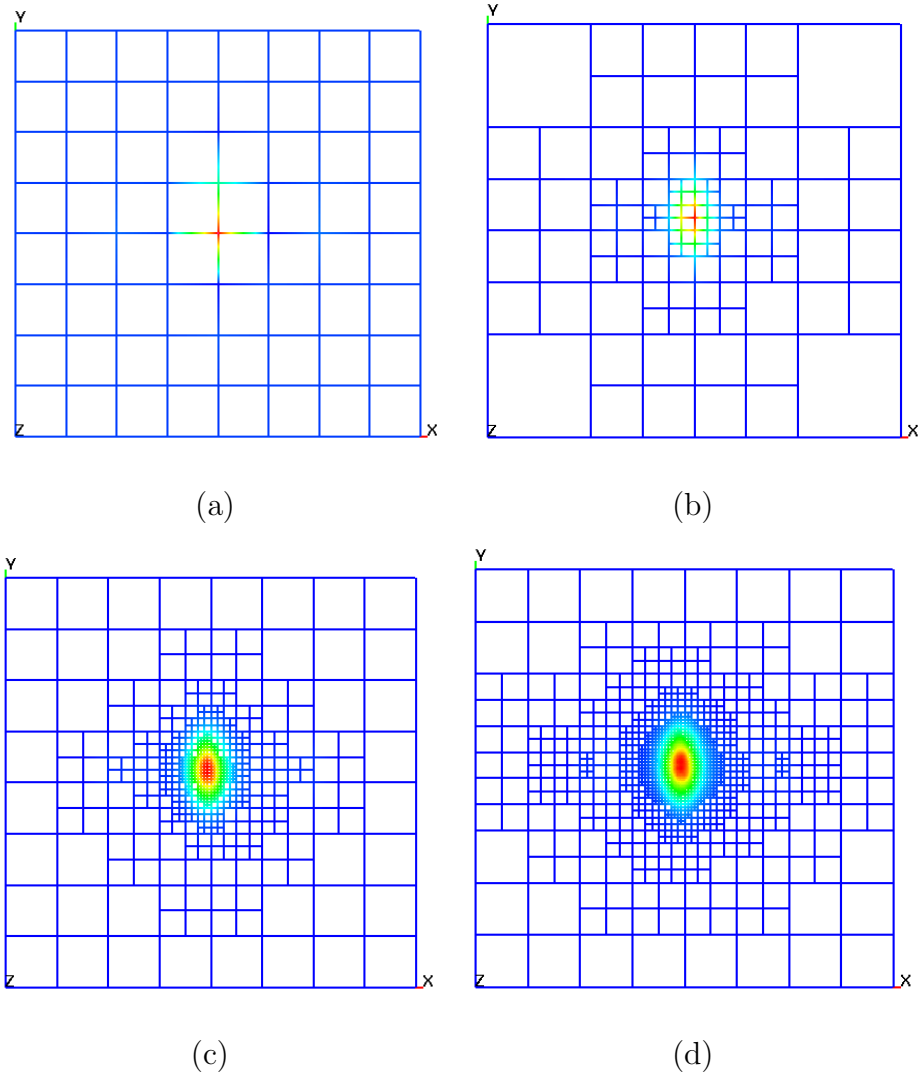

Fig. 18. Forward mesh evolution on the illumination surface. Meshes after (a)0, (b)2, (c)4 and (d)5 adaptive refinements are depicted.

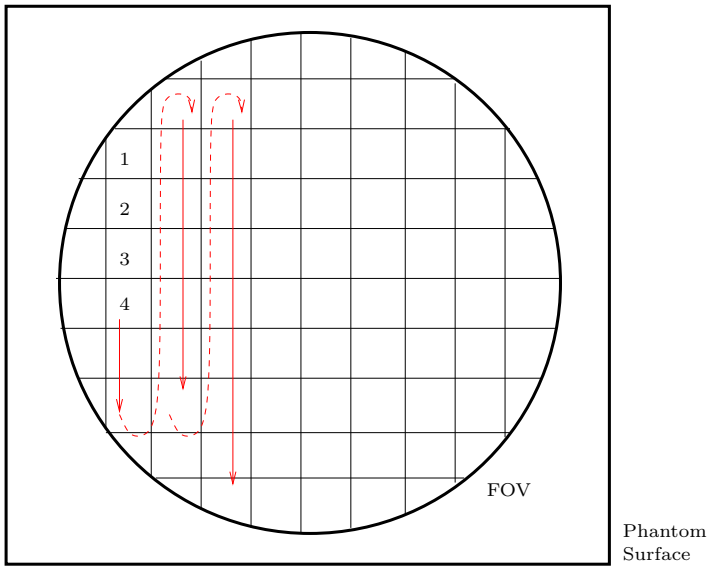

Fig. 19. Raster scanning of the CCD pixels to determine the area fluorescence measurements.

model based tomography approaches to work. To account for the different orders of magnitudes of the observed and simulated measurements, the real and imaginary components of the fluorescence measurements were referenced with the position with the maximum simulated fluorescence amplitude value. This referencing was only employed to compare the simulated and measured boundary measurements, and not for inverse image reconstruction. The simulated and observed fluorescence fluence is plotted against the detector points resulting from a raster scan across CCD camera pixels mapping the measurement region (Fig.19). Fig.20a-20d depict the model match between experimentally observed and simulated fluorescence ($v^{re} + iv^{im}$) at the measurement surface for the target depths of $1cm$ and $2cm$. Observed and simulated fluorescence follow the same general trend, the differences in their profiles can

be attributed to three main reasons: 1) for the purposes of simulation fluorescent targets were treated as spheres with radius $2.5mm$, however the actual fluorescent targets were made in the chemistry glass blowing workshop and had ellipsoidal shape with varying glass wall thickness. 2) The image intensifier employed for making measurements had variations in sensitivity across its surface which results in a positive bias for points towards the center of the measurement region. 3) Measurement data is also corrupted by arbitrary thermal and electronic noise in the gain modulated homodyne instrumentation and the leakage of excitation light through fluorescence filters. The accuracy of forward simulation of coupled diffusion equations also affects the model mismatch error between the simulated and predicted measurements. The root mean squared model mismatch error(RMSE) across all detector points was computed for adaptively refined finite element meshes used for forward simulation. RMSE was defined as:

$$RMSE = sqrt \sum_{d=1}^{M} (v_d^{meas.} - v_d^{sim.})(v_d^{meas.} - v_d^{sim.})^* \tag{4.10}$$

$v_d^{meas.}$ and $v_d^{meas.}$ denote the measured and simulated complex fluence $v = v_{re} + iv_{im}$ at the detector point d; * indicates the complex conjugate. RMSE decreased rapidly during the first couple of iterations of adaptive mesh refinements and then converged to a constant value (Fig.20e,f). Forward simulations were started with coarse meshes with $1cm$ side cubical finite elements. The above results suggest that three adaptive mesh refinements are enough for accurate simulation of coupled diffusion equations with an expanded area excitation source.

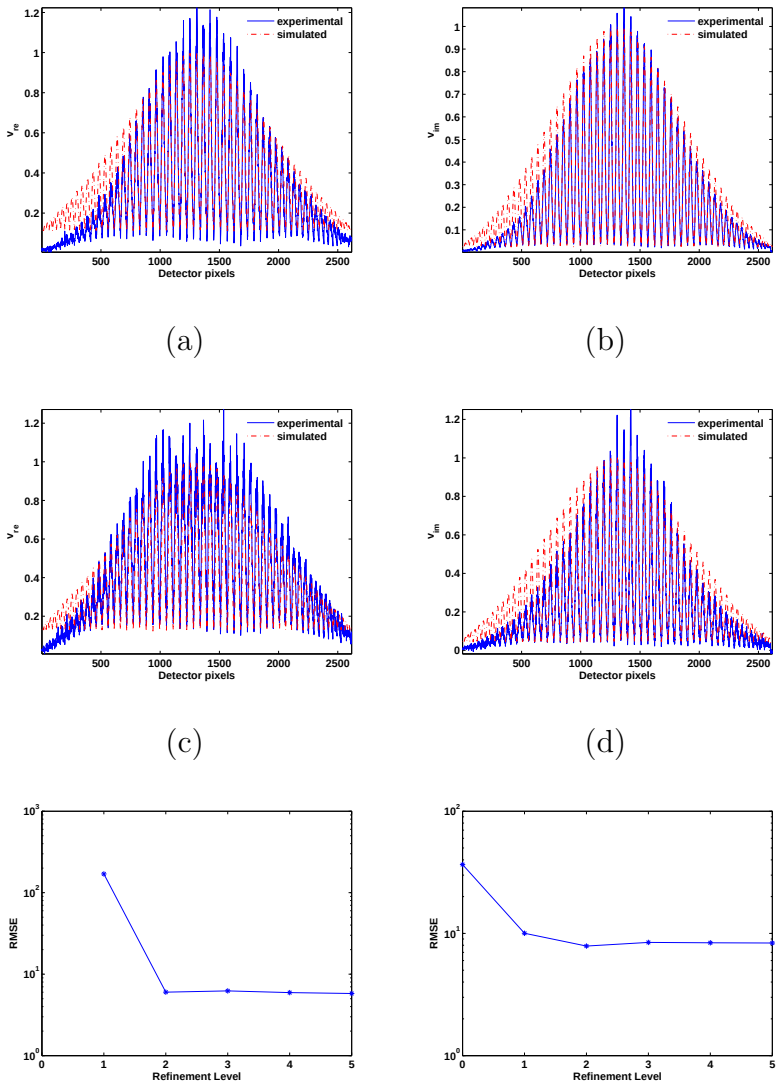

Fig. 20. Experimentally observed and simulated real and imaginary components of fluorescence fluence(v_{re}, v_{im}) at the measurement surface are plotted vs detector points for the target depths of $1cm$ (Fig.20-a,b) and $2cm$ (Fig.20-c,d). Fig.20-e,f plot the root mean squares model mismatch error(RMSE) for adaptive refinements of the mesh used for solution of coupled diffusion equations.

3. Image reconstructions

The adaptive tomography algorithm described in section-B was used to reconstruct the three dimensional images of fluorescence absorption distribution in the tissue phantom from experimentally observed fluorescence measurements. The image reconstruction procedure was initiated with coarse state (512 cells) and parameter ($64 cells$) meshes. Computations were performed on a 2.00 GHz Pentium-M notebook computer with 2GB of memory. Image reconstructions required 12 to 15 minutes of computational time depending upon the target depth. Fig.21 and Fig.22 depict the true and reconstructed fluorescent targets for target depths of $1cm$ and $2cm$ respectively. The top 10% of the contour levels of the reconstructed fluorescence absorption were considered to constitute the fluorescent heterogeneity. Both the state and parameter meshes were automatically refined during the reconstruction process. As shown in Fig.18 state mesh was primarily refined at the illumination surface to resolve the expanded laser source, while the parameter mesh was resolved finer in the region containing the recovered fluorescent target(Fig.21e and Fig.22e). The recovered target volume was over predicted for both $1cm$ and $2cm$ deep targets, However the recovered target volume depended on the arbitrary definition of recovered fluorescent target as the top 10% of contour levels. The recovered target for the $2cm$ deep case was lifted towards the illuminated surface. This can be attributed to the lower fluorescence signal penetrating up to the measurement surface which was corrupted to a greater degree by the excitation light leakage through the fluorescence filters than the fluorescence signal arising from the $1cm$ deep target. The lateral displacement of the recovered targets compared to the true position occurs because

of uncertainity in positioning of the fluorescent target within the phantom. Fig.21-f and Fig.22-f depict the change in model misfit $\|v - \sigma z\|$ with Gauss-Newton iterations. Traditional optical tomography schemes are characterized by a monotonous decrease in model misfit with the progress of solution. The presented optical tomography scheme allows small increase in value of model misfit with the progress of iterations as the entire Lagrange functional $L(u, v, \lambda^{ex}, \lambda^{em}, q)$ is minimized. Furthermore, the magnitude of the misfit functional changes with the refinements of the state and parameter mesh. The image reconstructions were terminated if the number of Gauss-Newton iterations exceeded 40 or if the algorithm stopped further progress without triggering mesh refinements leading to computer memory exhaustion. The image reconstruction details are summarized in Table-3.

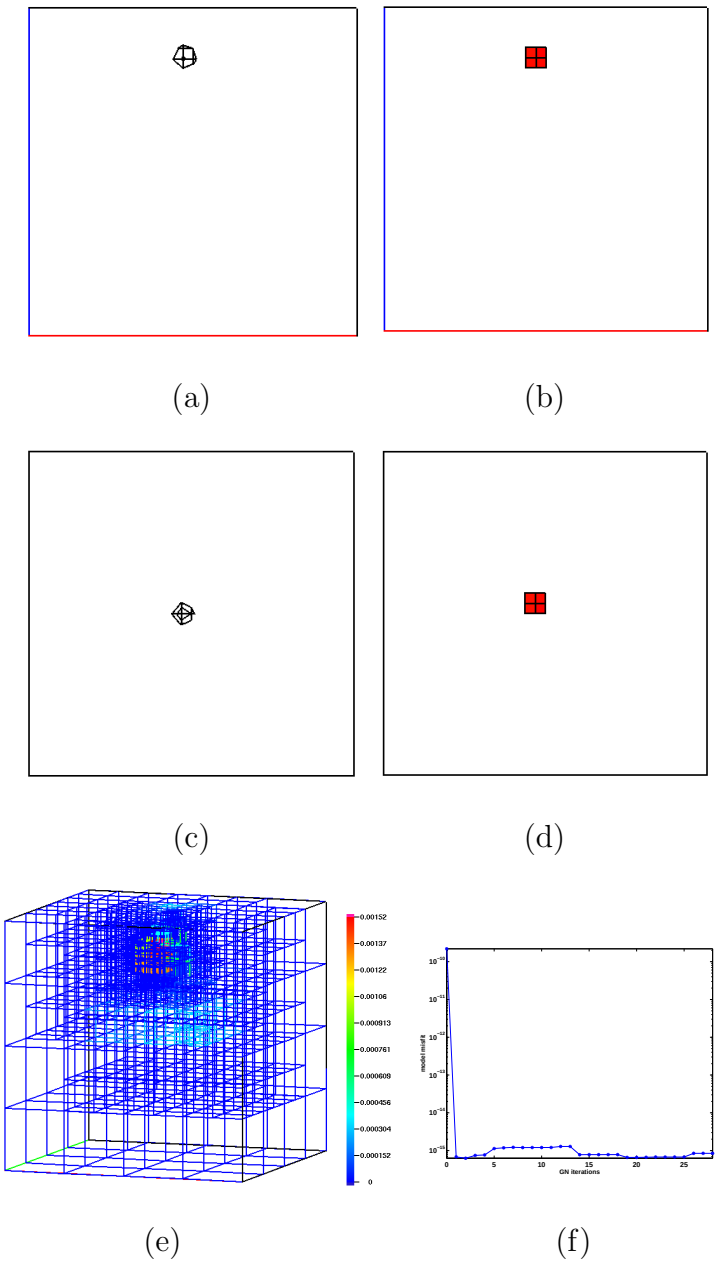

Fig. 21. Reconstructed and true images of $1cm$ deep fluorescent target:(a) True target (lateral view), (b) recovered target (lateral view), (c) True target (top view), (d) recovered target (top view), (e) Final parameter mesh, (f) Convergence of model misfit $\|v - \sigma z\|$ with Gauss-Newton(GN) iterations.

TABLE III

Table summarizes the reconstructed images for the $1cm$ and $2cm$ deep fluorescent targets. *Iter* stands for the number of Gauss-Newton iterations, $(x, y, z)_{true}$ and $(x, y, z)_{recovered}$ indicate the centroids of the true and recovered targets, N_q is the number of parameter unknowns in the final parameter mesh.

$depth(cm)$	Iter.	$\frac{1}{2}\left\|v - \sigma z\right\|_{\Sigma}^{2}$	$(x, y, z)_{\text{true}}$	$(x, y, z)_{\text{recovered}}$	N_q
1.0	28	$8.469 \cdot 10^{-16}$	$(4.0, 4.0, 6.75)$	$(4.0, 4.0, 6.75)$	2584
2.0	14	$1.124 \cdot 10^{-15}$	$(4.0, 3.8, 5.75)$	$(4.25, 3.75, 6.25)$	2416

D. Conclusions

We have experimentally demonstrated a novel clinically relevant non-contact fluorescent optical tomography system capable of increased resolution images. Area illumination and area detection frequency domain fluorescence measurements were performed on a $512ml$ tissue phantom with a gain modulated image intensified CCD camera setup operated in a homodyne mode. Fluorescent targets buried at the depths of $1cm$ and $2cm$ were identified and located successfully by employing a dual mesh adaptive finite element based tomography algorithm. Independent finite element meshes were used for modeling the light propagation in tissue and for iteratively updating the unknown fluorescence absorption map. This allowed efficient numerical simulation of area illumination source obtained by expanding the beam from a laser diode. The adaptation of the parameter mesh was governed by the progress in identifying the fluorescent target in previous iterations and no *a priori* information

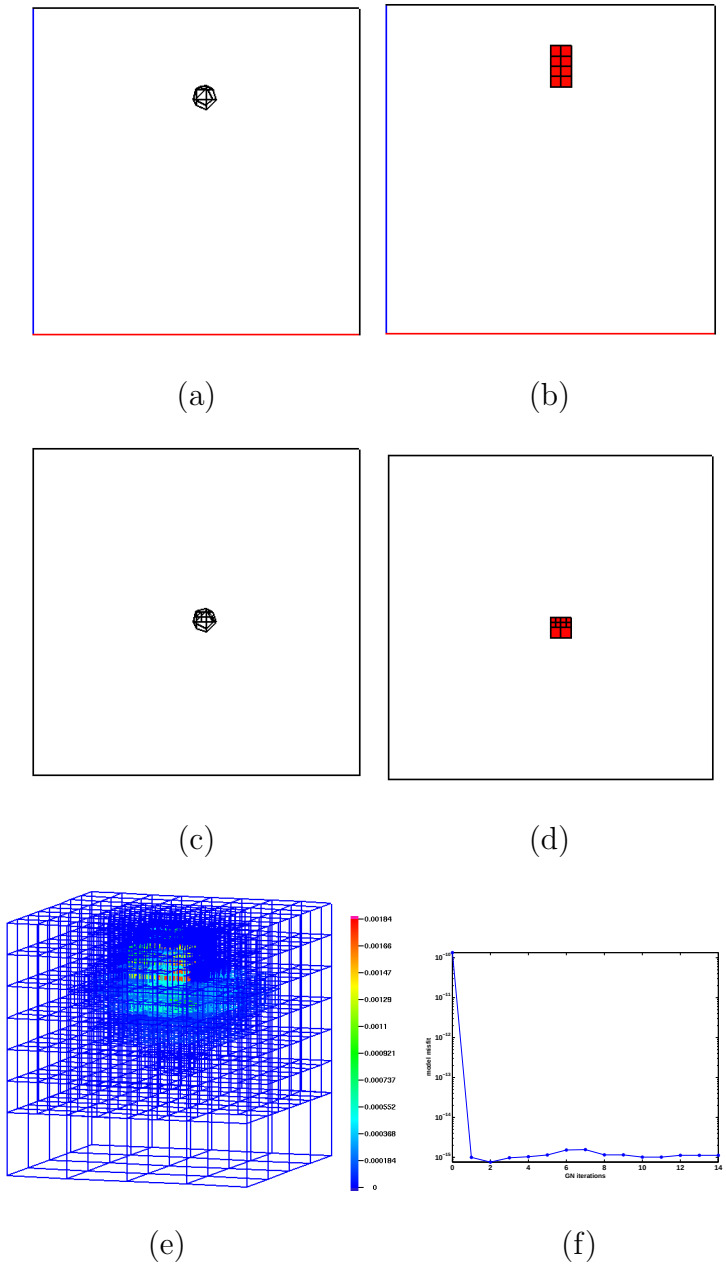

Fig. 22. Reconstructed and true images of $2cm$ deep fluorescent target:(a) True target (lateral view), (b) recovered target (lateral view), (c) True target (top view), (d) recovered target (top view), (e) Final parameter mesh, (f) Convergence of model misfit $\|v - \sigma z\|$ with Gauss-Newton(GN) iterations.

was employed, unlike the other dual mesh schemes employed in optical tomography where dual modality information such as that from ultrasound imaging [114] are used to generate finite element meshes for unknown optical parameters. Our scheme allows the generation of optimal finite element meshes, which accurately capture the variation in optical properties of tissue vs. discretization based on structural variations. The final number of unknown parameters was 2584 and 2416 for $1cm$ and $2cm$ deep targets. The number of unknowns is one order of magnitude less than required by conventional non-adaptive fluorescence tomography schemes [117] for identifying the fluorescence absorption map in a clinically relevant 512 ml tissue phantom. The reduced number of unknowns acts as a type of additional regularization and allows stable reconstructions in the presence of measurement noise.

The proposed tomography system was restricted by 1) limited field of view of $4cm$ and 2) low sensitivity of the image intensifier to the large dynamic range of fluorescence intensities over the surface. These limitations affected the accuracy of the recovered location and recovered size of $2cm$ deep fluorescent target. Improvements in optical design and more sensitive image intensifiers can enable fluorescence measurement acquisition over the entire tissue phantom surface and will be the focus of future work.

CHAPTER V

TWO TARGET RESOLUTION STUDIES

A. Introduction

The fluorescence tomography algorithm described in chapter III enables the tomographic imaging of two fluorescent targets in close proximity. In chapter IV, tomographic reconstructions from experimental area-illumination and area-detection measurements were presented for a single fluorescent target buried at the depths of upto $2cm$ from the illumination surface. In this this chapter we extend the experimental studies to the imaging of two fluorescent targets with varying lateral separation. In the following sections the experimental methods, the match of experimental data with simulations, and the results of image reconstruction studies are described.

B. Materials and methods

The tissue phantom used in the studies reported in chapter IV was modified by drilling $1mm$ holes at the bottom plate to enable the positioning of two fluorescent targets at varying lateral positions. Fig.23 depicts the bottom surface of the phantom box with the coordinates of the positioning holes. Four target positions were chosen with decreasing lateral separation $(1.17, 0.88, 0.55, 0.34$ cm) between the targets. The targets were glass bulbs of $5mm$ diameter and filled with $1\mu M$ ICG solution in 1% Liposyn. After placing the targets the tissue phantom was filled with 1% Liposyn solution. Table.IV lists the (x, y) coordinates of the two targets for each of the

TABLE IV

Table lists the (x, y) coordinates of the two targets for the resolution experiments, Δ is the edge to edge distance between the targets.

Case	$(x, y)_{\text{target-1}}$	$(x, y)_{\text{target-2}}$	Δ
1	$(3.8, 4.6)$	$(5.0, 3.0)$	1.17
2	$(3.8, 4.6)$	$(5.0, 3.9)$	0.88
3	$(3.9, 3.9)$	$(5.0, 3.9)$	0.55
4	$(5.0, 4.6)$	$(5.0, 3.9)$	0.34

four experiments carried out. The z coordinate or the height of target centers was fixed at $6.75cm$ to provide the depth of $1cm$ from the illumination surface of the phantom. Two target experiments were carried out with two different experimental configurations. First configuration was the one described in chapter IV with a $4cm$ field of view on the top surface of phantom. To increase the FOV to $6cm$, the optical configuration was changed and the fluorescence filters were moved to the front of the focusing lens. The two imaging setups are compared in Fig.24. The higher FOV provided by the second imaging setup, allowed the use of a broader excitation source. The excitation sources used with the two imaging setups are presented in Fig.25.

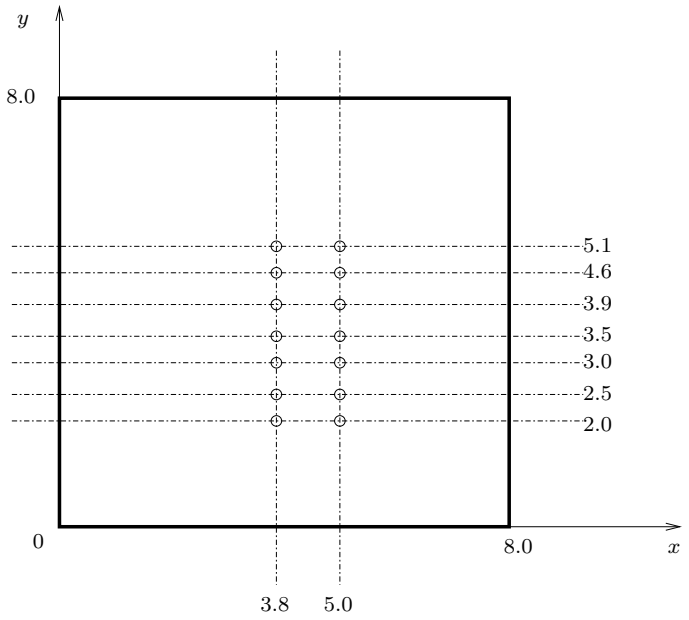

Fig. 23. The bottom ($z = 0$) plane of the tissue phantom is demonstrated with the positioning holes drilled for two target experiments.

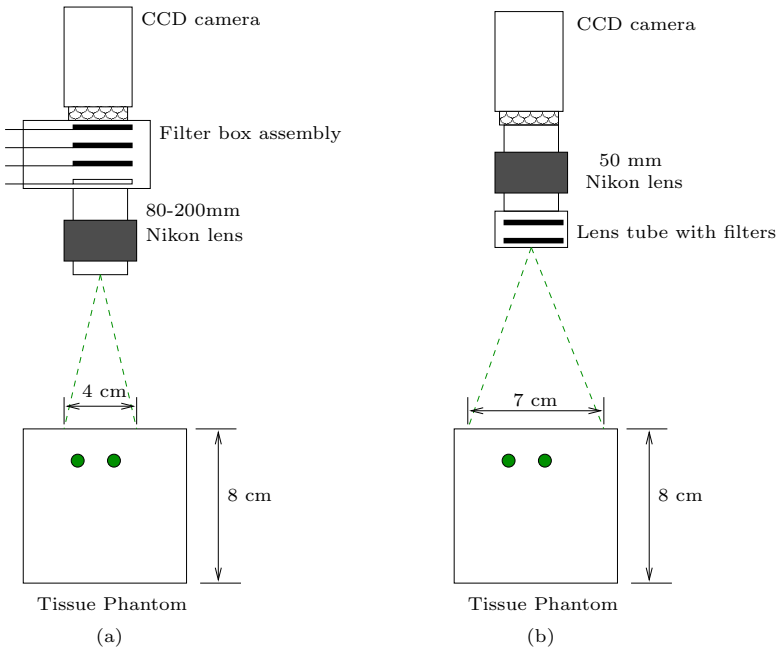

Fig. 24. Optics setup for two target experiments. a) original instrumentation arrangement with FOV of $4cm$, b) FOV increased to $7cm$ by removing the filter box assembly and changing the focusing lens, Filters were placed in a lens tube in the front of the focusing lens.

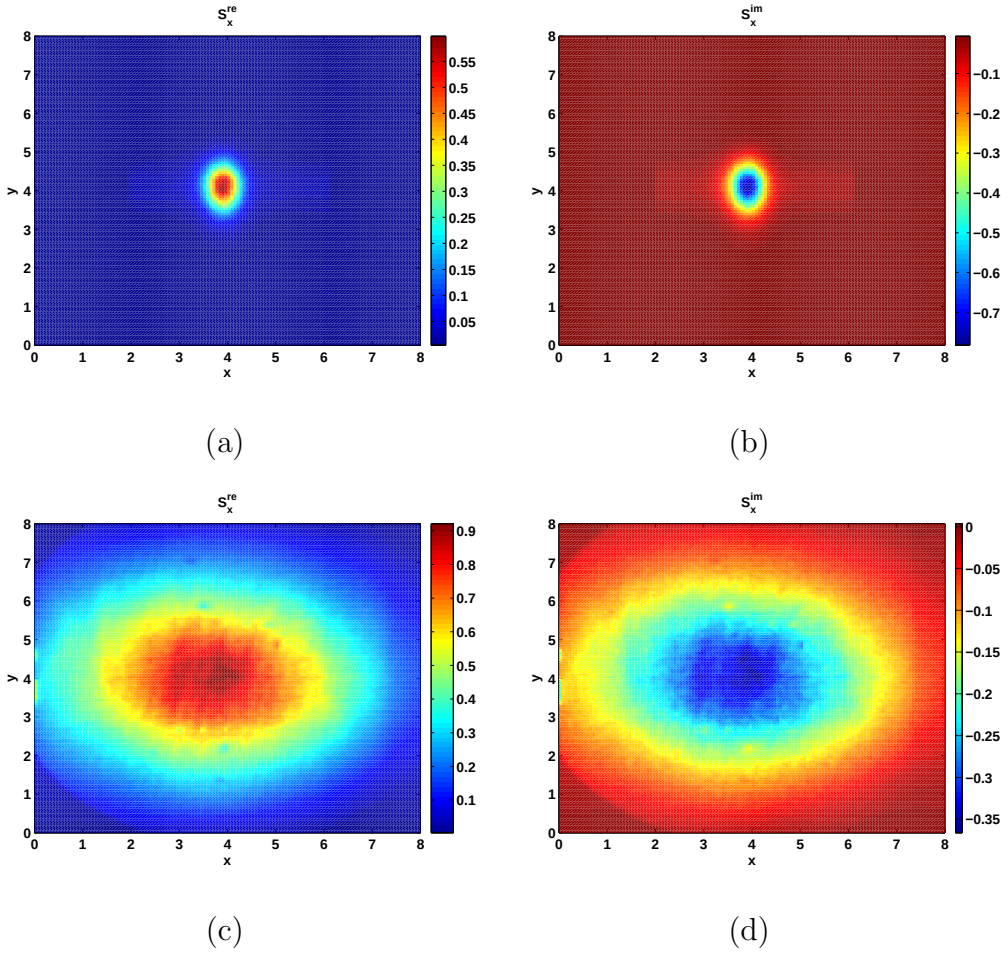

(a) (b)

(c) (d)

Fig. 25. Excitations source for (a,b)4cm FOV: real and imaginary components (c,d) 6cm FOV: real and imaginary components.

C. Results and discussion

1. Forward model match

As a first step towards accessing the feasibility of tomographic reconstruction of two fluorescent targets from experimental area measurements, forward model match studies were performed. For the four different target spacings, the predicted fluorescence measurements were generated using the adaptive finite element based forward solver incorporating the actual experimental excitation source. Forward model comparisons were compiled for both the $4cm$ and $6cm$ FOV cases. Figures (26) to (29) depict the comparison of normalized real and imaginary fluorescence fluence obtained from experiments and simulations for the target spacing detailed in table-B. The top rows in these figures represents the results from the $4cm$ FOV experiments, while the bottom row represents the $6cm$ FOV experiments. Impact of the FOV on the forward model match is clear in all the four target spacing cases. In the $4cm$ FOV case the excitation source was confined to a narrow region, and it failed to excite one of the targets to generate sufficient fluorescent signal for detection. The simulated measurement profile is broadened as a result of fluorescence emanating from two different centers in all the cases, However it is only in case-1(26c,d) that two distinct peaks can be discerned. The experimental and simulated measurements collected for the target spacing in case (1) fail to register the presence of one of the fluorescent targets in the $4cm$ FOV experiment. Hence, a broad distribution of the excitation source is needed to excite randomly distributed fluorescent targets. For the target spacings in cases (2) to (3), simulated measurements show a broadened fluorescence

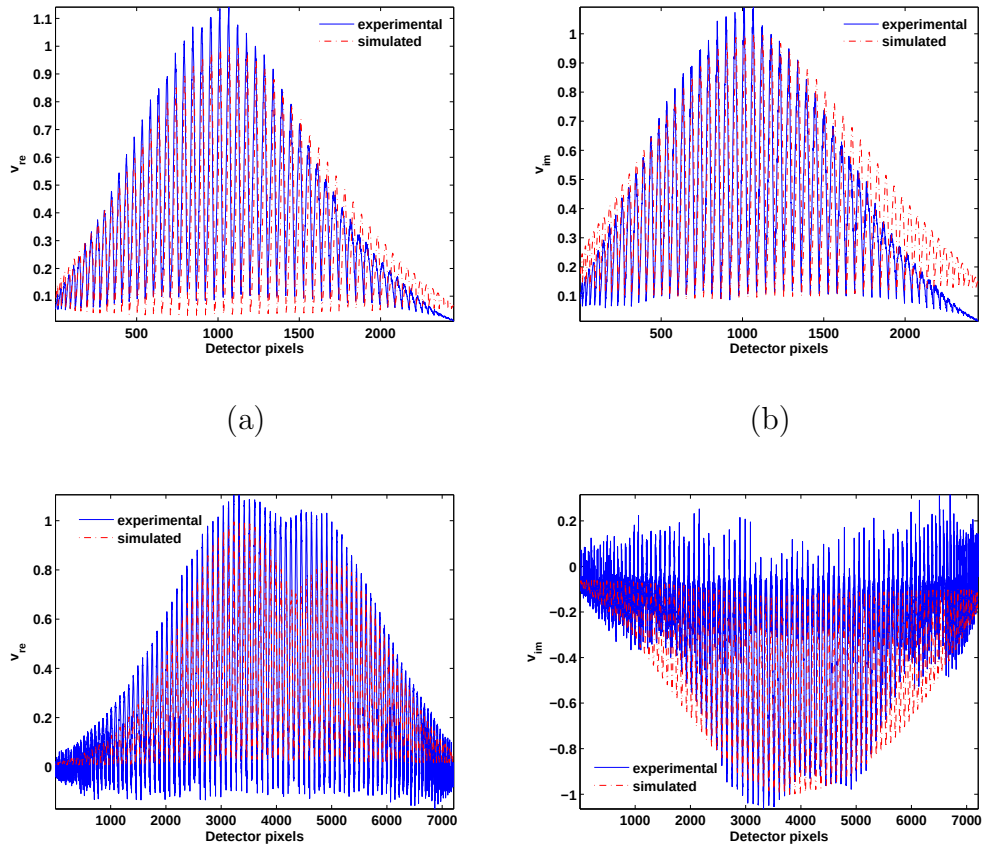

Fig. 26. Model match of experimental and predicted fluorescence measurements for two target experiment-case-1, (a,b) $4cm$ FOV experiment(real and imaginary components), (c,d) $6cm$ FOV experiment(real and imaginary components).

distribution for both the $4cm$ and $6cm$ FOV cases as shown in figures 27 and 28. However the experimental measurements in the $4cm$ FOV case do not follow the trend of the simulation as the fluorescence generated by one of the targets is too weak to be significantly registered on the image intensifier. Another advantages of the higher FOV experiments is the greater number of independent camera pixels available for measurements i.e. over 7000 as opposed to 2900 for the $4cm$ FOV case. The plots in Fig.29 are an anomaly resulting from the movement of the phantom or the camera system during the experiment, which causes the peaks of experimental and simulated data to be at different locations in the $4cm$ FOV case.

2. Image reconstructions

Based on the forward model match, only the target spacing (1) was considered for image reconstruction. Figures 30a and 30b depict the reconstructions obtained from the simulated data(refer to Fig.26). Figure 30c depicts the image reconstruction from actual experimental data for the $6cm$ FOV case(refer to Fig.26c,d).

Reconstructed images from the $6cm$ FOV experiment exhibit distinct maxima corresponding to the two targets while in the $4cm$ FOV case, only one clear minima is discernible as the the fluroescent target with weaker emission is reconstructed as a broadened trough. The reconstruction from actual experimental data fails as the reconstructed targets are located at the phantom surface. The failure of image reconstructions from the expanded laser sources in the laboratories, suggests the increasing ill-posed ness of the inverse problem for reconstructing multiple targets from only the reflectance measurements. Further the pattern of the excitation source is important

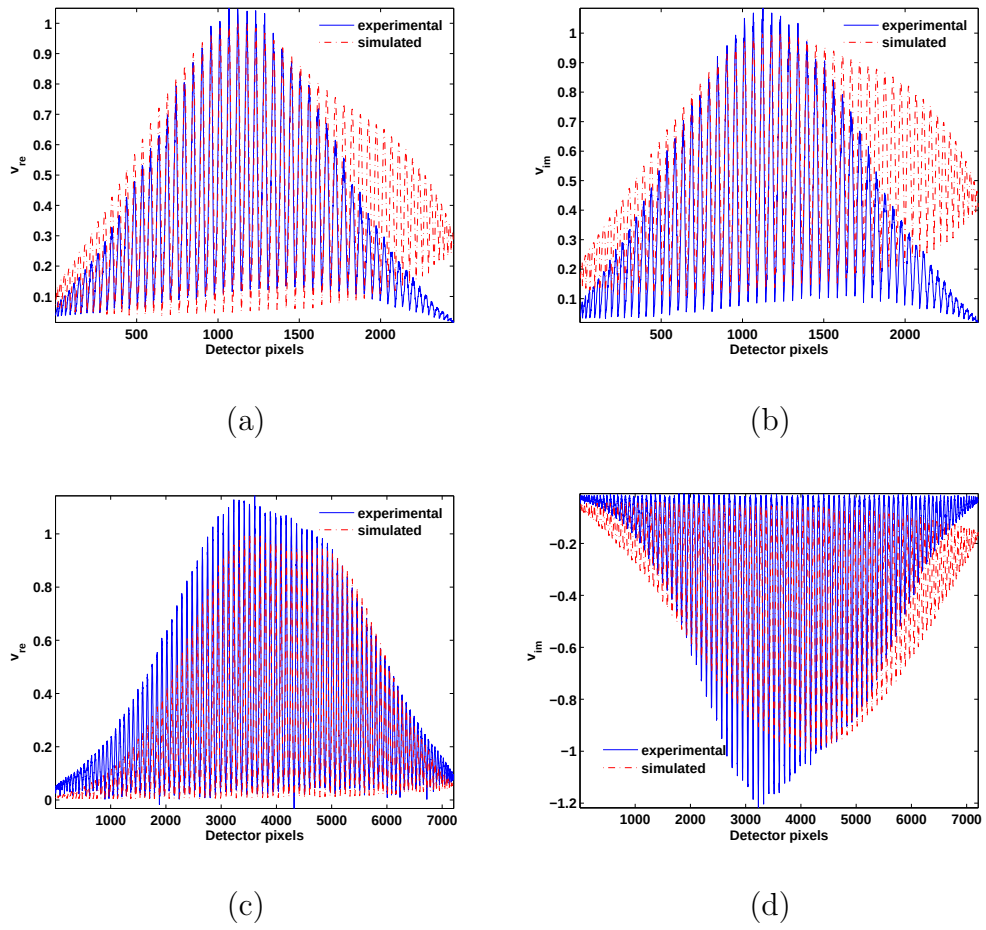

Fig. 27. Model match of experimental and predicted fluorescence measurements for two target experiment-case-2, (a,b) $4cm$ FOV experiment(real and imaginary components), (c,d) $6cm$ FOV experiment(real and imaginary components).

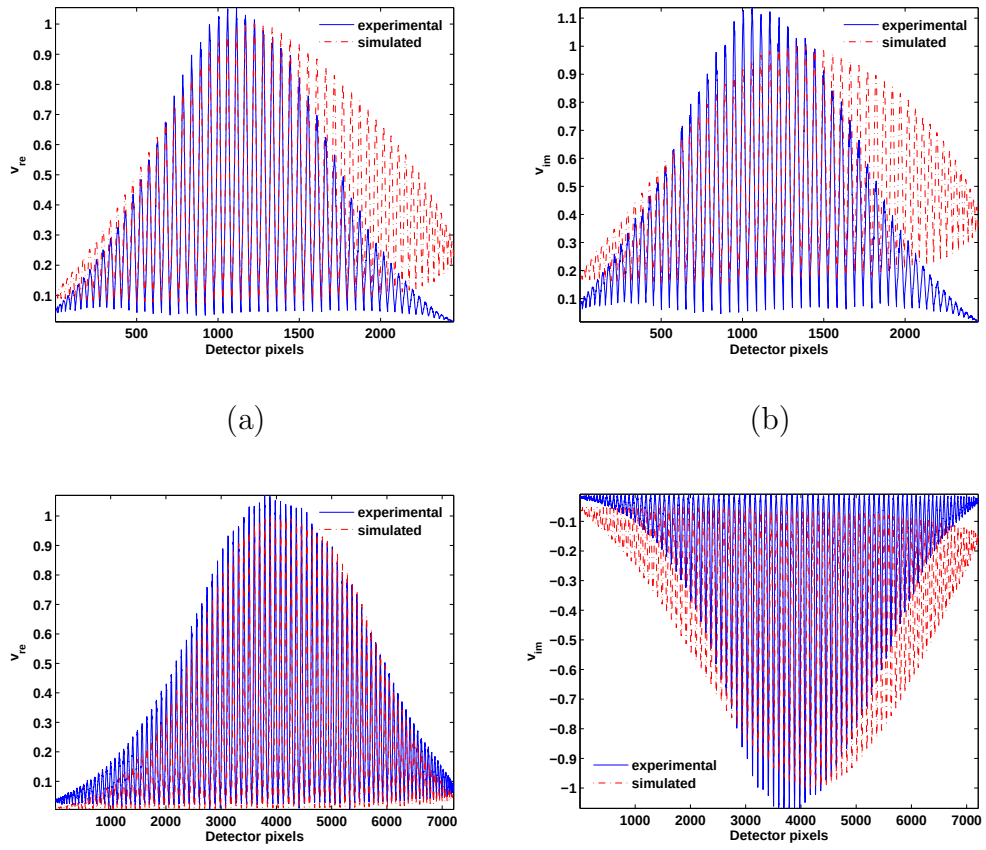

Fig. 28. Model match of experimental and predicted fluorescence measurements for two target experiment-case-3, (a,b) $4cm$ FOV experiment(real and imaginary components), (c,d) $6cm$ FOV experiment(real and imaginary components).

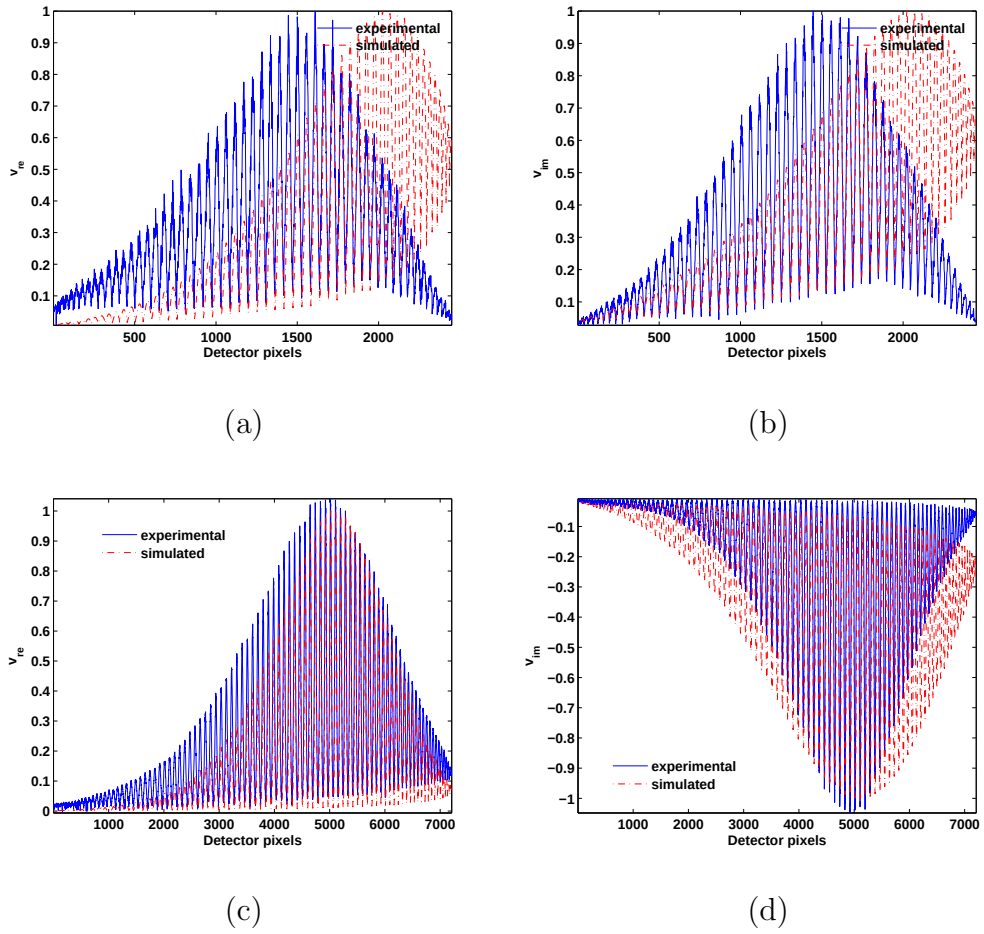

Fig. 29. Model match of experimental and predicted fluorescence measurements for two target experiment-case-4, (a,b) $4cm$ FOV experiment(real and imaginary components), (c,d) $6cm$ FOV experiment(real and imaginary components).

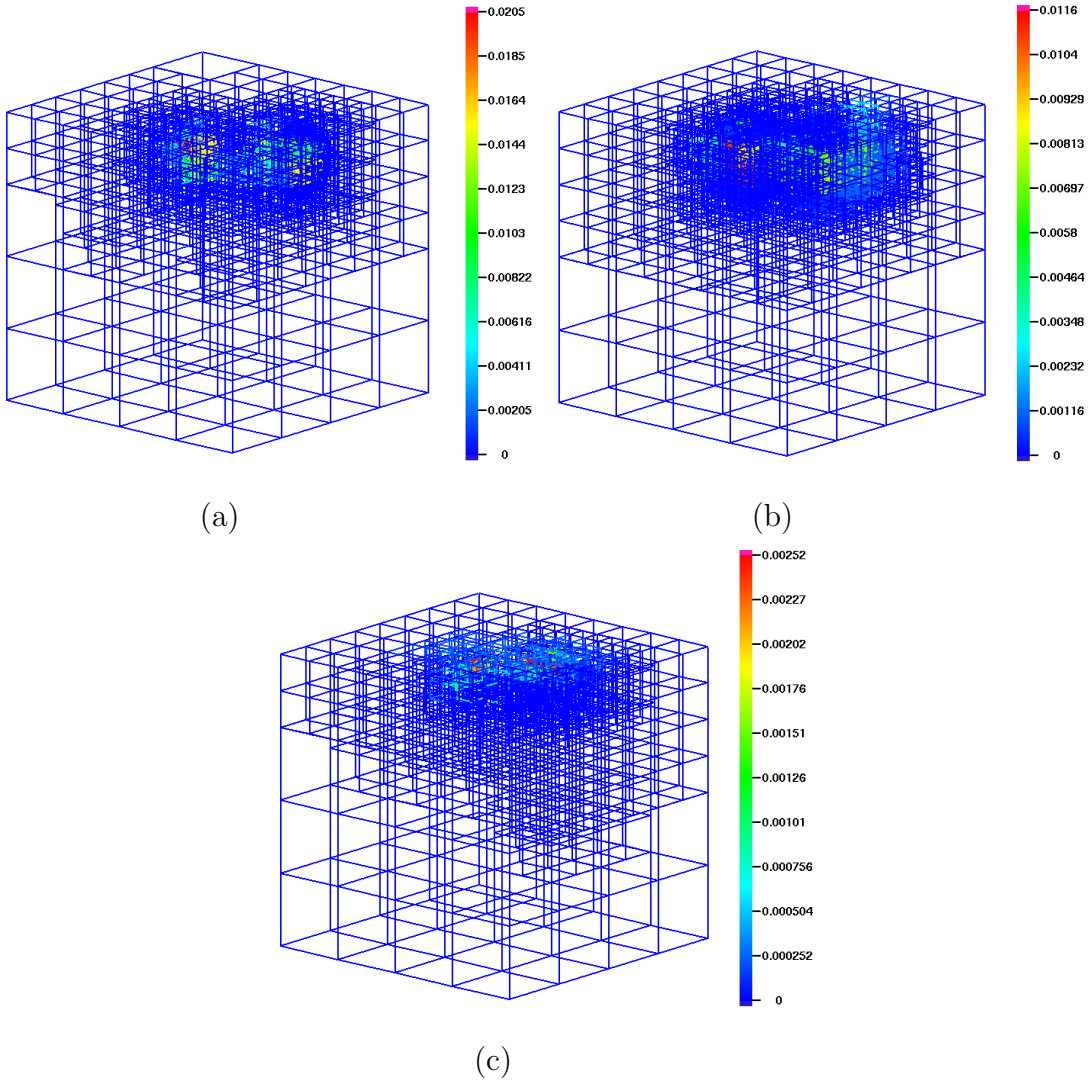

Fig. 30. Two target reconstructions: a) Simulated data 6cm FOV, b) Simulated data 4cm FOV, c)Experimental data 6cm FOV.

as the perfect Gaussian source provides high resolution two target reconstructions as demonstrated in chapter III, but the experimental sources generated by expanding the NIR laser beam do not perform as well in simulation studies. Further progress in reconstructing multiple fluorescent targets will require: 1) determining optimal surface illumination pattern, 2) Increasing the FOV while maintaining high fluorescence signal to ratio in presence of randomly distributed fluorescent targets. The second aim can be accomplished by employing multiple source and detector regions on the phantom surface i.e. by repeating the experiments with different locations of the area illumination over the phantom surface, and integrating the information collected from multiple experiments for image reconstruction.

CHAPTER VI

RADIATIVE TRANSPORT BASED SMALL ANIMAL FLUORESCENCE TOMOGRAPHY

A. Introduction

As described in chapter II, the diffusion equations are valid for describing photon transport at large source-detector separations and when $\mu_s' >> \mu_a$. In small animal tomography, the diffusion approximation to the radiative transport equation may not be valid. The full radiative transport equations (RTE) may accurately describe NIR photon propagation in small animal models, but at a substantially higher computational expenditure. Non-linear optimization based tomography based on the RTE model is not attractive because of the large computational time needed for inverting even very small phantoms [44], as the forward solver is called repeatedly during the optimization iterations. Each forward iteration with RTE can take hours on current workstations. As a first step towards developing RTE based tomography, we have tried first order Born approximation, which results in a fast tomography algorithm as it requires only one forward and one adjoint solution of the coupled RTE system (2.11). Different solution methods for solving the RTE model have been discussed in chapter II. ATTILA [65, 66] is a state of the art commercial radiative transport solver developed by Transpire corporation.(Gig Harbor,WA 98335). In collaboration with Photon Migrations Laboratories, ATTILA was modified to solve the frequency-domain coupled RTE's for fluorescence generation and propagation. In the following lines a brief description of fluorescence tomography with modified AT-

TILA as the forward solver and Born approximation based algebraic reconstruction technique is provided.

B. Methods

ATTILA can not handle complex variables, hence the fluorescence tomography problem was cast in terms of separate real and imaginary components. The coupled radiative transport equations for fluorescence imaging can be written by separating the real and imaginary parts of complex angular fluence L. In the following equations x denotes excitation field and m denotes fluorescent emission field. The coupled transport equations are:

$$-\frac{\omega}{c}L_x^{im} + \hat{s}\cdot\nabla L_x^{re} + \mu_{tx}L_x^{re} - \mu_{sx}\int_{4\pi} p(\hat{s},\hat{s}')L_x^{re}(\hat{s}')d\hat{s}' = S_x^{re} \tag{6.1}$$

$$+\frac{\omega}{c}L_x^{re} + \hat{s}\cdot\nabla L_x^{im} + \mu_{tx}L_x^{im} - \mu_{sx}\int_{4\pi} p(\hat{s},\hat{s}')L_x^{im}(\hat{s}')d\hat{s}' = S_x^{im} \tag{6.2}$$

$$-\frac{\omega}{c}L_m^{im} + \hat{s}\cdot\nabla L_m^{re} + \mu_{tm}L_m^{re} - \mu_{sm}\int_{4\pi} p(\hat{s},\hat{s}')L_m^{re}(\hat{s}')d\hat{s}' = S_m^{re} \tag{6.3}$$

$$+\frac{\omega}{c}L_m^{re} + \hat{s}\cdot\nabla L_m^{im} + \mu_{tm}L_m^{im} - \mu_{sm}\int_{4\pi} p(\hat{s},\hat{s}')L_m^{im}(\hat{s}')d\hat{s}' = S_m^{im} \tag{6.4}$$

where ω is the modulation frequency in Hz. and the excitation source is $S_x = S_x^{re} + S_x^{im}$, typically $S_x^{re} = 1$ and $S_x^{im} = 0$. The attenuation coefficients $\mu_{tx} = \mu_{axf}(\mathbf{r}) + \mu_{axi}(\mathbf{r}) + \mu_{sx}(\mathbf{r})$ and $\mu_{tm} = \mu_{am}(\mathbf{r}) + \mu_{sm}(\mathbf{r})$ denote the position dependent optical properties. The fluorescence absorption at position $\mathbf{r}$ is $\mu_{axf}(\mathbf{r})$. Tomographic image reconstruction process involves the recovery of this map over the tissue domain from scalar boundary fluence measurements. For brevity, it will be denoted by q.

The term $S_m = S_m^{re} + S_m^{im}$ represents the position dependent fluorescence source. The generation of fluorescence is considered to be isotropic, hence a $1/4\pi$ contribution is attributed to each scattering direction.

$$S_m = \frac{1}{4\pi}\frac{\phi\mu_{axf}}{1 - j\omega\tau}u = \frac{1}{4\pi}\phi\mu_{axf}\frac{(1 + j\omega\tau)}{1 + \omega^2\tau^2}u \tag{6.5}$$

Where

$$u = u^{re} + ju^{im} = \int_{4\pi} L_x^{re} + j\int_{4\pi} L_x^{im}$$

The real and imaginary parts of the fluorescence source are:

$$S_m^{re} = \frac{1}{4\pi}\frac{\phi\mu_{axf}}{1 + \omega^2\tau^2}u^{re} - \frac{\phi\mu_{axf}\omega\tau}{1 + \omega^2\tau^2}u^{im} \tag{6.6}$$

$$S_m^{im} = \frac{1}{4\pi}\frac{\phi\mu_{axf}}{1 + \omega^2\tau^2}u^{im} + \frac{\phi\mu_{axf}\omega\tau}{1 + \omega^2\tau^2}u^{re} \tag{6.7}$$

These equations can be written in an abbreviated form by defining transport operators corresponding to the right hand sides of equations (6.1) to (6.4).

$$H_x L_x = S_x \tag{6.8}$$

$$H_m L_m = B_{xm} L_x \tag{6.9}$$

H_x is the excitation transport operator [corresponding to equations (6.1) and (6.2)] and H_m is the emission transport operator [corresponding to equations (6.3) and (6.4)].

$L_x = [L_x^{re}, L_x^{im}]$, $L_m = [L_m^{re}, L_m^{im}]$ and $S_x = [S_x^{re}, S_x^{im}]$. B_{xm} is the operator which couples the excitation and emission fields. It corresponds to the left hand sides of equations (6.3) and (6.4).

1. Born approximation based tomography

In a tomography system, the scaler emission fluence, v is measured at the boundary detector locations numbered $j = 1, 2, ...M$. The parameter map, q is discretized on a finite element mesh with N nodes. The Born approximation based linearization is described in chapter II.E.1 for diffusion model. An analogous linearized model based on radiative transport equations can be written as:

$$z - z_0 = \mathbf{J}(q - q_0) \tag{6.10}$$

$$\mathbf{J} = \langle [H_m^*]^{-1} D, \frac{\partial B_{xm}}{\partial q} \rangle \tag{6.11}$$

where J is the Jacobian matrix (M x N) of sensitivities of the scalar emission fluence at the boundary detectors to the distributed q map and H_m^* is the adjoint of emission transport operator. H_m^* was approximated by switching the source and detector locations. This is only a rough approximation as unlike diffusion, transport operators are not self-adjoint. While D is the Dirac matrix (M x N) whose rows are unity at the nodes corresponding to detector locations and are zero elsewhere. q_0 is uniform guess for the fluorescence absorption and z_0 is the emission fluence at the detectors corresponding to q_0, while z denotes the actual detected emission fluence. Eqn (6.11) can be obtained from eqn(2.47) by treating all terms (except the coupling matrix B_{xm}) as independent of q. Eqn (6.11) is an illconditioned linear problem, hence direct inversion is not feasible. Numerical experiments suggested algebraic reconstruction technique (ART) or Kacmacz iterations as the most stable method for solving this inverse problem. ART iterations, as described in chapter.II.E.1. were implemented in MATLAB to solve eqn (6.11).

C. Numerical simulation results

Simulated fluorescence measurement data was generated in ATTILA as a collaborative project with John Rasmussen at the Photon Migration Labs and Todd Wareing at Transpire Corporation. Fluorescent targets ($5mm$ diameter) were simulated at the center and off-center position within a cylindrical phantom (height $2cm$, diameter $2.5cm$) of approximate dimensions needed for imaging a mouse. Sources and detectors were modeled as $1mm$ cylindrical discs positioned in three rings of 30 source and detector points. Forward and adjoint calculations were carried out with modified ATTILA solver on a fluorescent collection fine mesh (10436 nodes), while inverse image reconstruction was performed on a coarser mesh (886 nodes) to reduce the number of unknowns and convert eqn (6.11) into an overdetermined system. Forward and inverse meshes are depicted in Fig.31. Four thousand ART iterations were carried out, requiring less than 2 minutes on a SUN Ultrasparc-III workstation. Image reconstruction results are summarized in Fig.32. Fig.32a,d depict the true image of the fluorescent target at the center and offcenter positions. Fig.32b,c and Fig.32e,f depict the reconstructed images in isosurface(top 10% of the contour levels) and slice plots. Both the target size and locations were reconstructed accurately. The magnitude of the reconstructed target at $\mu_{axf} = 0.002$ was two orders of magnitude lower than the true value of $\mu_{axf} = 0.299$ and sensitive to the initial guess. Hence concentration of the fluorescence dye in the tumor target may not be quantified without prior calibration. Fig.33 depicts results from tomography performed with only the central ring of sources and detectors are depicted. Fig.33b,c depict the reconstruction results obtained when frequency domain (FDPM) measurement data at $100MHz$ was used,

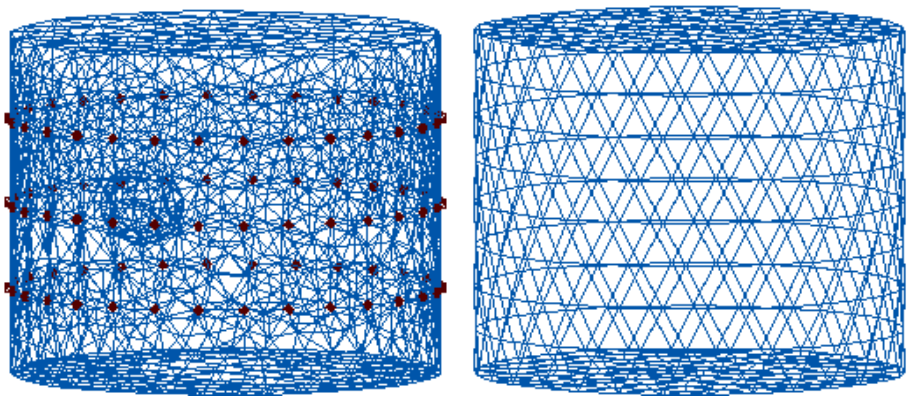

Fig. 31. Forward and inverse meshes used for RTE-Born inversion. Forward mesh(left) had 10436 nodes, Dots indicate the source/detector locations. Inverse mesh(right) had 886 nodes.

while Fig.33e,f depict the reconstruction results obtained when only the intensity information or continuous wave (CW) type measurements were used. The failure of image reconstruction from one ring of CW measurements, clear show the inadequacy of continuous wave measurements for fluorescence tomography.

D. Conclusions

The image reconstruction results from synthetic data suggest that fluorescence tomography based on radiative transport equations is feasible and it can be implemented in a computationally efficient manner by applying the Born approximation. In this preliminary work only one linearization about an initial homogeneous guess for fluorescence absorption map was used and that was adequate for accurate reconstruction of target size and volume. For more complicated tomography problems,

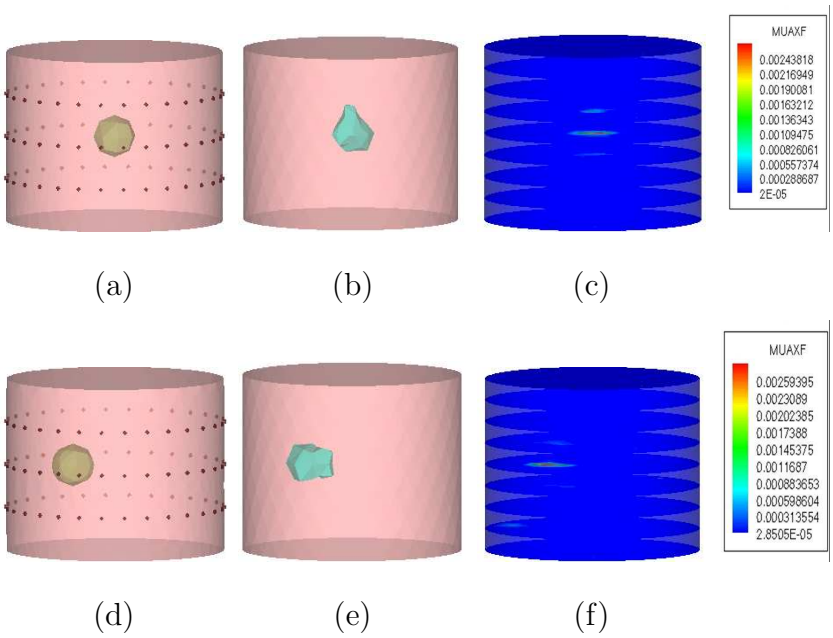

Fig. 32. Reconstruction results for RTE-Born tomography: a,d) true fluorophore distribution map (center and offcenter target), b,e) reconstructed target iso-surface plot, c,f) reconstructed target slice plot.

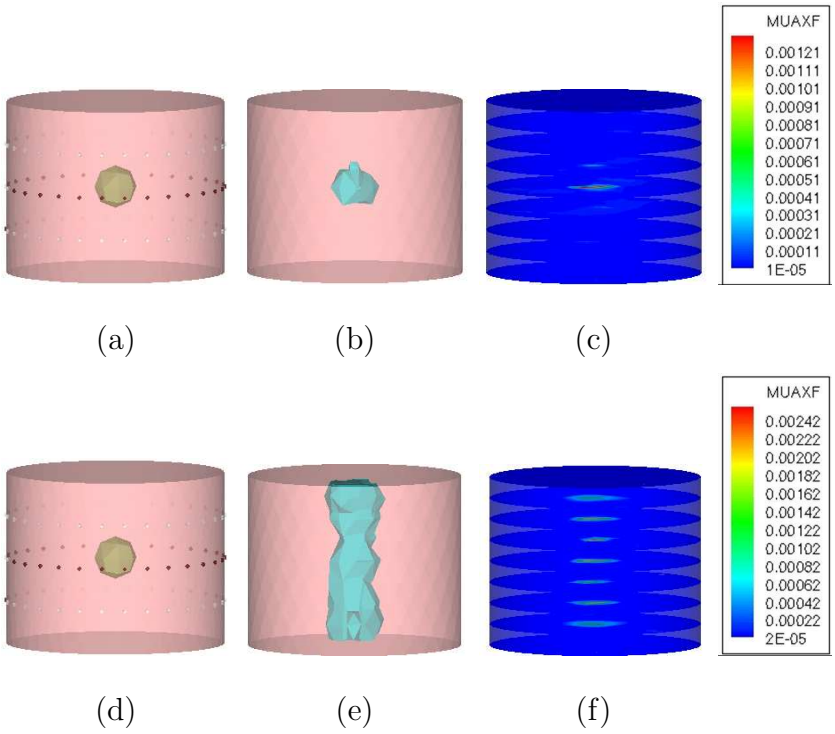

Fig. 33. Comparison of reconstruction results for RTE-Born tomography with FDPM and CW measurements: a,d) true fluorophore distribution map(FDPM and CW measurements), b,e) reconstructed target iso-surface plot, c,f) reconstructed target slice plot.

such as the presence of multiple fluorescence targets, the Born iterative method [77] may be needed for accurate image reconstructions. Improvements in the tomography scheme can be made by incorporating adaptive mesh refinements in forward and inverse meshes.

CHAPTER VII

CONCLUSIONS AND SUGGESTED FUTURE WORK

This dissertation focuses upon the development of a novel high resolution adaptive finite element based optical tomography system for three-dimensional localization of tumors in biological tissues tagged with fluorescent contrast agents. We focused on the reconstruction of the fluorophore absorption map from frequency domain measurements of the fluorescence emission signal acquired at the illumination plane in a non-contact manner. The techniques developed were general in scope to enable the tomographic reconstruction of the fluorophore lifetime map as well as any of the optical properties of the tissue media, which appear as parameters in the coupled photon diffusion equations. Although the developed technique was not tested on real biological tissues, sufficient groundwork in the area of tomography software and data acquisition procedures was developed to enable the application of fluorescence optical tomography in locating sentinel lymph nodes for tracking the progress of breast cancer in patients as well as small animal tomography. The following points highlight the issues addressed by this work.

- A dual adaptive finite element based optical tomography algorithm was developed. Separate finite element meshes were used to solve the coupled diffusion equation and for updating the unknown fluorescence absorption map. Although this was not the first application of dual meshing schemes in optical tomography, we presented the first scheme for *dynamic* and *independent* adaptation of both the forward and inverse meshes with the progress of the tomography

algorithm. This delinking of the forward and inverse meshes allowed the attainment of resolutions down to 0.0625 cm on the forward mesh and 0.125 cm on the inverse mesh while limiting the global degrees of freedom. Automatic generation of the optimal forward mesh enabled the accurate simulation of irregularly shaped area-illumination sources. This is in contrast to all previous optical tomography work, wherein meshes had to be carefully designed *a priori* for simulating the area-illumination source. The use of a separate coarser mesh for parameter estimation reduced the number of unknowns by more than an order of magnitude, while increasing the resolution. The opportunity for committing the inverse crime is avoided by our approach as the parameter map was initialized with uniform coarse cells with no knowledge of the target and the parameter mesh refined during the tomography process based on the variation in the estimated parameter map. This resulted in mesh refinement only around the suspected target region and coarsening elsewhere. Mesh refinement provides an additional regularization by limiting the high frequency errors in the reconstructed parameter map [120]. Mesh refinement process was found to be stable in presence of moderate measurement noise.

- The developed tomography scheme was tested with experimental data generated on a phantom. The tissue phantom was an $8cm$ x $8cm$ x $8cm$ clear acrylic box filled with 1% Liposyn solution. This is a clinically relevant volume for applications such as sentinel lymph node mapping. Area-illumination was achieved by an expanding the beam from an NIR laser diode. Area detection was performed with a gain modulated image intensifier charge coupled

device camera. Typically both the excitation and emission wavelength measurements were acquired within 5 minutes and without requiring any physical contact between the tissue phantom and the measurement apparatus. Surface fluorescence measurements acquired on the tissue phantom were successfully inverted to reconstruct fluorescent targets with volumes of $3ml - 4ml$ and with $0.25\mu M$ ICG concentrations buried at the depths of upto $2cm$ from the illumination surface. The area illumination source was characterized by utilizing high efficiency cross polarizers(extinction ratio 10000:1).

- Attempts were made to characterize the Rayleigh resolution for fluorescence optical tomography. Rayleigh resolution is the minimum separation of two fluorescent targets at which the maxima in the reconstructed images can still be differentiated. Simulation studies were performed with a Gaussian source and two $1cm$ deep $4mm$ diameter fluorescent targets placed at varying separations. Targets were resolved down to the separation of $1mm$, which is approximately the mean isotropic photon transport length in the tissues. Experimental verification of resolution studies could not be attained because of the signal to noise characteristics of the ICCD setup beyond a narrow $3cm$ field of view on the phantom surface. This suggests the sensitivity of image reconstruction to the spatial sampling of area detection measurements.

- As a side project during the progress of research, the use of alternative tomographic reconstruction schemes for small animal models was investigated. The diffusion approximation to RTE is not valid for describing photon transport small volume of mice. This could prevent the successful application of diffusion

based tomography for small animal disease models used widely for biomedical research. A rapid fluorescence tomography method for small animal imaging was developed by integrating the radiative transport equation (RTE) based forward model with the classical algebraic reconstruction techniques (ART). Preliminary results suggest the feasibility of RTE based fluorescence tomography.

In the candidate's opinion, the recommendations for the future work are as follows:

- The current tomography algorithm employed the Gauss-Newton method for generating the parameter update direction. Although Gauss-Newton approximation guarantees the positive definiteness of the Schur complement matrix(eqn (3.21)) and stabilizes the inversion process, it performs poorly when the error function residual is large near optimality, as is the case in presence of measurement noise. The use of full-Newton or quasi-Newton method needs to be investigated for generating parameter update directions. The ideal technique would be a hybrid approach which utilizes the Gauss-Newton update direction in the initial iterations and switches to full Newton method near the solution. The mesh adaptation in the presented work was driven by Kelly's mesh refinement criteria, which is optimized for Laplace equation. Mesh refinement driven by duality based error estimators [104] might provide meshes optimally designed for reduction of optimization error function.

- In the work presented, the image reconstruction problem was treated in a deterministic framework and the statistical information about measurement noise

or the distribution of the unknown parameter was ignored. Casting the image reconstruction problem in a probabilistic framework and treating the unknown parameter as a random variable with known *a priori* statistics might improve the performance of the tomography scheme in the presence of measurement noise. Further the tissue phantom employed had homogeneous background, while real biological tissue is highly heterogeneous. The performance of the tomography algorithm in the presence of structured background is needed before the transition to clinical applications.

- The current studies were limited by the narrow field of view (FOV) ($< 4cm$). Better image intensifier (filmless tube instead of the current GEN-III) may improve the signal to noise ratio across the field of view. Alternatively FOV can be increased by taking multiple measurements over the illumination surface by positioning the source beam and measurement region at multiple locations. These multiple experiments can then be inverted efficiently by utilizing parallel computing clusters simultaneously. Multiple experiment approach can incease the spatial sampling of the tissue phantom, while avoiding redundancy in the acquired data. Rayleigh resolution studies might be successful if carried out via a multiple experiment approach.

REFERENCES

[1] A. B. Thompson and E. M. Sevick-Muraca, "NIR fluorescence contrast enhanced imaging with ICCD homodyne detection: Measurement precision and accuracy," *J. Biomed. Opt.*, vol. 8, pp. 111–120, 2002.

[2] R. Weissleder and U. Mahmood, "Molecular imaging," *Radiology*, vol. 219, pp. 316–333, 2001.

[3] R. Weissleder, "Molecular imaging: Exploring the next frontier," *Radiology*, vol. 212, pp. 609–614, 1999.

[4] C. Contag, S. Fraser, and R. Weissleder, "Strategies in *in vivo* molecular imaging," *Neo Reviews*, vol. 12, pp. e225–e232, 2000.

[5] M. G. Pomper, "Molecular imaging: An overview," *Acad. Radiol.*, vol. 8, pp. 1141–1153, 2001.

[6] A. C. Kak and M. Slaney, *Principles of Computerized Tomographic Imaging*. New York: IEEE Press, 1988.

[7] M. Rosenthal, J. Cullom, W. Hawkins, S. Moore, B. Tsui, and M. Yester, "Quantitative SPECT imaging: A review and recommendations by the focus committee of the society of nuclear medicine computer and instrumentation council," *J. Nucl. Med.*, vol. 36, pp. 1489–1513, 1995.

[8] R. Taillefer, "The role of ^{99m}tc-sestamibi and other conventional radiopharamceuticals in breast cancer diagnosis," *Semin. Nucl. Med.*, vol. 29, pp. 16–40,

1999.

[9] F. Beekman, D. McElroy, F. Berger, S. Gambhir, E. Hoffman, and S. Cherry, "Toward in vivo nuclaer microscopy: Iodine-125 imaging in mice using micro-pinholes," *Nucl. Med. Mol. Imaging*, vol. 29, pp. 933–938, 2002.

[10] A. Bogdanov, M. Simonova, and R. Weissleder, "Engineering membrane proteins for nuclear medicine: Applications for gene therapy and cell tracking," *Quantitative Journal of Nuclear Medicine*, vol. 44, pp. 224–235, 2000.

[11] T. Massoud and S. Gambhir, "Molecular imaging in living subjects: Seeing fundamental biological processes in a new light," *Genes and Development*, vol. 17, pp. 545–580, 2003.

[12] A. Chatziioannou, "Molecular imaging of small animals with dedicated PET tomographs," *Eur. J. Nucl. Med*, vol. 46, pp. 2899–2910, 2002.

[13] S. Cherry and S. Gambhir, "Use of positron emission tomography in animal research," *Ilar. J.*, vol. 42, pp. 219–232, 2001.

[14] C. Contag, S. Fraser, and R. Weissleder, "Strategies in in vivo molecular imaging," *Neo Reviews*, vol. 1, pp. e225–e231, 2000.

[15] J. Bronzino, ed., *The Biomedical Engineering Handbook*. Boca Raton, FL: CRC Press, 1995.

[16] R. Weissleder, A. Moore, and U. Mahmood, "In vivo magnetic resonance imaging of transgene expression," *Nat. Med.*, vol. 6, pp. 351–355, 2000.

[17] A. Moore, J. Basilion, A. Chiocca, and R. Weissleder, "Measuring transferrin receptor gene expression by NMR imaging," *Biochem. Biophys. Acta*, vol. 1402, pp. 239–249, 1998.

[18] D. Turnbull and F. Foster, "In vivo ultrasound biomicroscopy in developmental biology," *Trends Biotechnol.*, vol. 20, pp. S29–S33, 2002.

[19] G. Lanza and S. Wickline, "Targetted ultrasonic contrast agents for molecular imaging and therapy," *Prog. Cardiovasc. Dis.*, vol. 44, pp. 13–31, 2001.

[20] A. Welch and M. van Gemert, eds., *Optical-Thermal Response of Laser Irradiated Tissue*. New York: Plenum Press, 1975.

[21] V. Ntziachristos, A. Yodh, M. Schnall, and B. Chance, "Concurrent MRI and diffuse optical tomography of breast after indocyanine green enhancement," *Proc. Natl. Acad. Sci.*, vol. 97, pp. 2767–2772, 2000.

[22] J. P. Houston, A. B. Thompson, M. Gurfinkel, and E. M. Sevick-Muraca, "Sensitivity and penetration depth of NIR fluorescence contrast enhanced diagnostic imaging," *Photochem. Photobiol.*, vol. 77, no. 4, pp. 77–103, 2003.

[23] M. Zhao, M. Yang, E. Baranov, X. Wang, S. Penman, A. R. Moossa, and R. M. Hoffman, "Spatial-temporal imaging of bacterial infection and antibiotic response in intact animals," *Proceedings of National Academy of Sciences*, vol. 98, no. 17, pp. 9814–9818, 2001.

[24] M. Yang, E. Baranov, P. Jiang, F.-X. Sun, X. Li, L. L. S. Hasegava, M. Bouvet, S. Penman, A. R. Moossa, and R. M. Hoffman, "Whole body optical imaging

of green fluorescent protein-expressing tumors and metastases," *Proceedings of National Academy of Sciences*, vol. 987, no. 3, pp. 1206–1211, 2000.

[25] M. Yang, E. Baranov, S. Penman, A. R. Moossa, and R. M. Hoffman, "Visulizing gene expression by whole body fluorescence imaging," *Proceedings of National Academy of Sciences*, vol. 97, no. 22, pp. 12278–12282, 2000.

[26] L. A. Gross, G. S. Baird, and R. C. Hoffman, "The structure of the chromophore within DsRed, a red fluorescent protein from coral," *Proceedings of National Academy of Sciences*, vol. 97, pp. 11990–11995, 2000.

[27] M. A. O'Leary, D. A. Boas, B. Chance, and A. Yodh, "Reradiation and imaging of diffuse photon density waves using fluorescent inhomogeneities," *J. Luminescence*, vol. 60, pp. 281–286, 1994.

[28] J. Wu, Y. Wang, L. Perleman, I. Itzkan, R. R. Desai, and M. S. Feld, "Time resolved multichannel imaging of fluorescent objects embedded in turbid media," *Opt. Lett.*, vol. 20, pp. 489–491, 1995.

[29] E. L. Hull, M. G. Nichols, and T. H. Foster, "Localization of luminescent inhomogeneities in turbid media with spatially resolved measurements of CW diffuse luminescence emittance," *Appl. Opt.*, vol. 37, pp. 2755–2765, 1998.

[30] J. C. Schotland, "Continuous wave diffusion imaging," *J. Opt. Soc. Am. A*, vol. 14, no. 275–279, 1997.

[31] M. A. O'Leary, D. A. Boas, B. Chance, and A. G. Yodh, "Fluorescence lifetime imaging in turbid media," *Opt. Lett.*, vol. 20, pp. 426–428, 1996.

[32] E. E. Graves, J. Ripoll, R. Weissleder, and V. Ntziachristos, "A submillimeter resolution fluorescence molecular imaging system for small animal imaging," *Med. Phys.*, vol. 30, pp. 901–911, 2003.

[33] V. Ntziachristos and R. Weissleder, "Experimental three-dimensional fluorescence reconstruction of diffuse media by use of a normalized Born approximation," *Opt. Lett.*, vol. 26, no. 12, pp. 893–895, 2001.

[34] V. Chernomordik, D. Hattery, I. Gannot, and A. H. Gandjbakhche, "Inverse method 3-D reconstruction of localized in vivo fluorescence-application to Sjøgren syndrome," *IEEE J. Sel. Top. Quantum Electron.*, vol. 54, pp. 930–935, 1999.

[35] H. Quan and Z. Guo, "Fast 3-D optical imaging with transient fluorescence signals," *Opt. Express*, vol. 12, no. 3, pp. 449–457, 2004.

[36] D. Y. Paithankar, A. U. Chen, B. W. Pogue, M. S. Patterson, and E. M. Sevick-Muraca, "Imaging of fluorescent yield and lifetime from multiply scattered light reemitted from random media," *Appl. Opt.*, vol. 36, no. 10, pp. 2260–2272, 1997.

[37] M. J. Eppstein, D. E. Dougherty, T. L. Troy, and E. M. Sevick-Muraca, "Biomedical optical tomography using dynamic parametrization and Bayesian conditioning on photon migration measurements," *Appl. Opt.*, vol. 38, no. 10, pp. 2138–2150, 1998.

[38] M. J. Eppstein, D. J. Hawrysz, A. Godavarty, and E. M. Sevick-Muraca, "Three

dimensional near infrared fluorescence tomography with Bayesian methodologies for image reconstruction from sparse and noisy data sets," *Proc. Nat. Acad. Sci.*, vol. 99, pp. 9619–9624, 2002.

[39] R. Roy and E. M. Sevick-Muraca, "Truncated Newton's optimization schemes for absorption and fluorescence optical tomography: Part(1) theory and formulation," *Opt. Express*, vol. 4, no. 10, pp. 353–371, 1999.

[40] H. Jiang, "Frequency-domain fluorescent diffusion tomography: A finite element based algorithm and simulations," *Appl. Opt.*, vol. 37, no. 22, pp. 5337–5343, 1998.

[41] A. Godavarty, M. J. Eppstein, C. Zhang, S. Theru, A. B. Thompson, M. Gurfinkel, and E. M. Sevick-Muraca, "Fluorescence-enhanced optical imaging in large tissue volumes using a gain-modulated ICCD camera," *Phys. Med. Biol.*, vol. 48, pp. 1701–1720, 2003.

[42] A. D. Klose, U. Netz, J. Beuthan, and A. H. Hielscher, "Optical tomography using the time-independent equation of radiative transfer part 1: Forward model," *J. Quant. Spectroscopy Rad. Transfer*, vol. 72, pp. 691–713, 2002.

[43] J. Chang, H. L. Graber, , and R. L. Barbour, "Imaging of fluorescence in highly scattering media," *IEEE Trans. Biomedical Eng.*, vol. 44, pp. 810–822, 1997.

[44] A. Klose and A. Hielscher, "Fluorescence tomography with simulated data based on the equation of radiative transfer," *Opt. Lett.*, vol. 28, no. 12, 2003.

[45] S. Jacques, "Time-resolved reflectance spectroscopy in turbid tissues," *IEEE Transactions in Biomedical Engineering*, vol. 36, no. 12, pp. 1155–1161, 1989.

[46] R. Richards-Kortem and E. Sevick-Muraca, "Quantitative optical spectroscopy for tissue diagnosis," *Annu. Rev. Phys. Chem.*, vol. 47, pp. 555–606, 1996.

[47] K. Licha, B. Riefke, V. Ntziachristos, A. Becker, B. Chance, and W. Semmler, "Hydrophillic cyanine dyes as contrast agents for near infrared tumor imaging: Synthesis, photophysical properties, and spectroscopic in vivo characterization," *Photochem. Photobiol.*, vol. 72, no. 3, pp. 392–398, 2000.

[48] R. Cubeddu, G. Canti, A. pifferi, P. Taroni, and G. Valentini, "Fluorescence lifetime imaging of experimental tumors in hematoporphyrin derivative sensitized mice," *Photochem. Photobiol.*, vol. 66, no. 2, pp. 229–236, 1997.

[49] B. Chance, J. Leigh, H. Miyake, D. Smith, S. Nioka, R. Greenfeld, M. Finander, K. Kauffmann, W. levy, M. Young, P. Cohen, H. Yoshioka, and R. Borestsky, "Comparision of time-resolved and unresolved measurements of deoxyheamoglobin in brain," *Proceedings of National Academy of Sciences*, vol. 85, pp. 4791–4975, 1988.

[50] S. R. Arridge and W. R. B. Lionheart, "Non-uniqueness in diffusion-based optical tomography," *Optics Letters*, vol. 23, pp. 882–884, 1998.

[51] S. Colak, M. van der Mark, G. Hooft, J. Hoogenraad, E. van der Linden, and F. Kuijpers, "Clinical optical tomography and nir spectroscopy for breat cancer detection," *IEEE J. Sel. Top. Quant.*, vol. 5, no. 4, pp. 1143–1158, 1999.

[52] J. Hebden, S. Arridge, and D. Delpy, "Optical imaging in medicine: I experimental techniques," *Phys. Med. Biol.*, vol. 42, no. 5, pp. 825–840, 1997.

[53] A. Ishimaru, *Wave Propagation and Scattering in Random Media*. New York: Academic Press, 1978.

[54] A. Ishimaru, "Optical multiple scattering by particles," *Part. Part. Syst. Charact.*, vol. 11, pp. 183–188, 1994.

[55] L. Henyey and J. Greenstein, "Diffuse radiation in galaxy," *Astrophys. J.*, vol. 93, pp. 70–83, 1941.

[56] S. Jacques, C. Alter, and S. Prahl, "Angular dependence of he-ne laser light scattering by human dermis," *Lasers Life Sc.*, vol. 1, pp. 309–333, 1987.

[57] A. D. Klose, U. Netz, J. Beuthan, and A. H. Hielscher, "Optical tomography using the time-independent equation of radiative transfer part 2: Inverse model," *J. Quant. Spectroscopy Rad. Transfer*, vol. 72, pp. 715–732, 2002.

[58] A. H. Hielscher, R. Alcouffe, and R. Barbour, "Comparision of finite-difference transport and diffusion calculations for photon migration in homogeneous and heterogeneous tissues," *Phys. Med. Biol.*, vol. 43, pp. 1285–1302, 1998.

[59] O. Dorn, "A transport-backtransport method for optical tomography," *Inverse Problems*, vol. 14, pp. 1107–1130, 1998.

[60] R. Sanchez and N. McCormick, "A review of neutron transport approximations," *Nucl. Sci. Eng.*, vol. 80, pp. 481–535, 1982.

[61] E. E. Lewis and W. F. M. Jr., *Computational Methods of Neutron Transport*. New York: John Wiley and Sons, 1984.

[62] S. Richling, E. Meinkohn, N. Kryzhevoi, and G. Kanschat, "Radiative transfer with finite elements I. basic method and tests," *Astronomy and Astrophysics*, vol. 380, pp. 776–788, 2001.

[63] G. Abdoulaev and A. Hielscher, "Three-dimensional optical tomography with the equation of radiative transfer," *Journal of Electronic Imaging*, vol. 12, pp. 594–601, 2003.

[64] K. Ren, G. Abdoulaev, G. Bal, and A. Hielscher, "Algorithm for solving the equation of radiative transfer in the frequency domain," *Optics Letters*, vol. 29, pp. 578–580, 2004.

[65] T. Wareing, J. McGhee, and J. Morel, "ATTILA: A three dimensional, unstructured tetrahedral mesh discrete ordinates transport code," *Trans. Am. Nucl. Soc.*, vol. 75, p. 146, 1996.

[66] J. Morel, T. Wareing, and K. Smith, "A linear-discontinuous spatial differencing scheme for s_n radiative transfer calculations," *Journal Comp. Phys.*, vol. 128, pp. 445–462, 1996.

[67] A. Milstein, S. Oh, K. J. Webb, C. A. Bouman, Q. Zhang, D. Boas, and R. P. Milane, "Fluorescence optical diffusion tomography," *Appl. Opt.*, vol. 42, no. 16, pp. 3061–3094, 2003.

[68] S. C. Brenner and L. R. Scott, *The Mathematical Theory of Finite Element Methods*. Berlin, Germany: Springer, 2002.

[69] P. G. Ciarlet, *The Finite Element Method for Elliptic Problems*. Philadelphia: SIAM, 2002.

[70] O. Axelsson and V. A. Barker, *Finite Element Solution of Boundary Value Problems*. Philadelphia: SIAM, 2001.

[71] J. Heino, S. Arridge, J. Sikora, and E. Somersalo, "Anisotropic effects in highly scattering media," *Phys Rev E*, vol. 68, p. 031908(8pp), 2003.

[72] F. Fedele, M. J. Eppstein, J. Laible, A. Godavarty, and E. M. Sevick-Muraca, "Fluorescence photon migration by boundary element method," *Journal of Computational Physics*, in press, 2005.

[73] J. Ripoll and V. Ntziachristos, "Iterative boundary method for diffuse optical tomography," *Journal of Optical Society of America*, vol. 20, no. 6, pp. 1103–1110, 2003.

[74] J. Ripoll, M. Nieto-Vesperinas, R. Weissleder, and V. Ntziachristos, "Fast analytical approximations for arbitrary geometries in diffuse optical tomography," *Optics Letters*, vol. 27, no. 7, pp. 527–529, 2002.

[75] J. Ripoll, V. Ntziachristos, R. Carminati, and M. Nieto-Vesperinas, "Kirchoff approximation for diffusive waves," *Physical Review E*, vol. 64, pp. 517–519, 2001.

[76] A. J. Davies, D. B. Christianson, L. C. W. Dixon, R. Roy, and P. van der Zee, "Reverse differentiation and the inverse diffusion problem," *Advances in Engineering Software*, vol. 28, pp. 217–221, 1997.

[77] J. Lee and E. M. Sevick-Muraca, "Three-dimensional fluorescence enhanced optical tomography using referenced frequency-domain photon migration measurements at emission and excitation wavelengths," *Journal of Optical Society of America-A*, vol. 19, no. 4, pp. 759–771, 2002.

[78] A. H. Hielscher, A. Klose, and J. Beuthan, "Evolution strategies for optical tomographic characterization of homogeneous media," *Optics Express*, vol. 7, pp. 507–518, 2000.

[79] E. Chong and S. Zak, *An Introduction to Optimization*. New York: John Wiley and Sons, 2001.

[80] G. Strang, *Linear Algebra and Its Applications*. New York: Academic Press, 1980.

[81] M. Powell, "Convergence properties of algorithms for nonlinear optimization," *SIAM Review*, vol. 28, no. 4, pp. 487–500, 1986.

[82] S. R. Arridge and M. Schweiger, "A gradient based optimization scheme for optical tomography," *Opt. Express*, vol. 2, no. 6, pp. 213–225, 1998.

[83] J. Nocedal, R. Byrd, and P. Lu, "A limited memory algorithm for bound constrained optimization," *SIAM J. of Scientific and Statistical Computing*, vol. 16(5), pp. 1190–1208, 1995.

[84] J. J. More and D. J. Thuente, "Line search algorithms with guaranteed sufficient decrease," *ACM Trans. Math. Software*, vol. 20, pp. 286–307, 1994.

[85] A. Joshi and E. M. Sevick-Muraca, *Adaptive Finite Element Methods for Distributed Parameter System Identification: Applications in Fluorescence Enhanced Frequency Domain Optical Tomography*, IEEE: American Control Conference, July 2004.

[86] A. N. Tikhonov and V. Y. Arsenin, eds., *Solution of Ill-Posed Problems*. Washington DC: Winston, 1977.

[87] R. Roy and E. M. Sevick-Muraca, "Active constrained truncated newton method for simple bound optical tomography," *Journal of Optical Society of America-A*, vol. 17, no. 9, pp. 16–27, 2000.

[88] J.C.Ye, K. Webb, and C. Bouman, "Optical diffusion tomography by iterative coordinate descent optimization in a bayesian framework," *Journal of Optical Society of America*, vol. 16, p. 2400, 1999.

[89] A. Gelb, *Applied Optimal Estimation*. Boston: MIT Press, 1974.

[90] J. P. Houston, S. Ke, W. Wang, C. Li, and E. M. Sevick-Muraca, "Optical and nuclear image quality analysis with in vivo NIR fluorescence and conventional gamma images acquired using a dual labeled tumor targeting probe," *J. Biomed. Opt. (submitted)*, September 2004.

[91] W. Bangerth, "Adaptive finite element methods for the identification of distributed coefficients in partial differential equations," PhD dissertation, University

of Heidelberg, 2002.

[92] W. Bangerth, "A framework for the adaptive finite element solution of large inverse problems. I. Basic techniques," Tech. Rep. 04-39, ICES, University of Texas at Austin, 2004.

[93] E. M. Sevick-Muraca, E. Kuwana, A. Godavarty, J. P. Houston, A. B. Thompson, and R. Roy. Ch.33, *Biomedical Photonics Handbook*, Boca Raton, FL: CRC Press, 2003.

[94] A. Godavarty, D. J. Hawrysz, R. Roy, E. M. Sevick-Muraca, and M. J. Eppstein, "Influence of the refractive index-mismatch at the boundaries measured in fluorescence enhanced frequency-domain photon migration imaging," *Opt. Express*, vol. 10, no. 15, pp. 650–653, 2002.

[95] A. Joshi, W. Bangerth, and E. Sevick-Muraca, "Adaptive finite element methods for fluorescence enhanced frequency domain optical tomography: Forward imaging problem," in *International Symposium on Biomedical Imaging*, pp. 1103–1106, IEEE, 2004.

[96] R. A. Adams, *Sobolev Spaces*. Burlington, MA: Academic Press, 1975.

[97] L. Beilina, "Adaptive Hybrid FEM/FDM Methods for Inverse Scattering Problems," PhD dissertation, Chalmers University of Technology, 2002.

[98] R. Becker, H. Kapp, and R. Rannacher, "Adaptive finite element methods for optimal control of partial differential equations: Basic concept," *SIAM J. Contr. Optim.*, vol. 39, pp. 113–132, 2000.

[99] R. Luce and S. Perez, "Parameter identification for an elliptic partial differential equation with distributed noisy data," *Inverse Problems*, vol. 15, pp. 291–307, 1999.

[100] D. G. Luenberger, *Optimization by Vector Space Methods*. New York: John Wiley, 1969.

[101] J. Nocedal and S. J. Wright, *Numerical Optimization*. New York: Springer, 1999.

[102] S. C. Brenner and R. L. Scott, *The Mathematical Theory of Finite Elements*. Berlin: Springer, 1994.

[103] R. Verfürth, *A Review of A Posteriori Error Estimation and Adaptive Mesh Refinement Techniques*. New York: Wiley/Teubner, 1996.

[104] W. Bangerth and R. Rannacher, *Adaptive Finite Element Methods for Differential Equations*. Berlin: Birkhäuser Verlag, 2003.

[105] M. Molinari, S. J. Cox, B. H. Blott, and G. J. Daniell, "Adaptive mesh refinement techniques for electrical impedence tomography," *Physiological Measurement*, vol. 22, pp. 91–96, 2001.

[106] M. Molinari, B. H. Blott, S. J. Cox, and G. J. Daniell, "Optimal imaging with adaptive mesh refinement in electrical impedence tomography," *Physiological Measurement*, vol. 23, pp. 121–128, 2002.

[107] R. Becker and R. Rannacher, "An optimal control approach to error estimation and mesh adaptation in finite element methods," *Acta Numerica*, vol. 10, pp. 1–102, 2001.

[108] H. Ben Ameur, G. Chavent, and J. Jaffré, "Refinement and coarsening indicators for adaptive parametrization: Application to the estimation of hydraulic transmissivities," *Inverse Problems*, vol. 18, pp. 775–794, 2002.

[109] A.-A. Grimstad, H. Krüger, T. Mannseth, G. Nævdal, and H. Urkedal, "Adaptive selection of parameterization for reservoir history matching," in *ECMOR VIII: 8th European Conference on the Mathematics of Oil Recovery*, pp. E–46, Freiberg, Germany, 2002.

[110] R. Li, W. Liu, H. Ma, and T. Tang, "Adaptive finite element approximation for distributed elliptic optimal control problems," *SIAM J. Control Optim.*, vol. 41, pp. 1321–1349, 2002.

[111] D. W. Kelly, J. P. d. S. R. Gago, O. C. Zienkiewicz, and I. Babuška, "A posteriori error analysis and adaptive processes in the finite element method: Part I–error analysis," *Int. J. Num. Meth. Engrg.*, vol. 19, pp. 1593–1619, 1983.

[112] W. Bangerth, R. Hartmann, and G. Kanschat, `deal.II` *Differential Equations Analysis Library, Technical Reference*, 2004. `http://www.dealii.org/`.

[113] A. Thompson, "Development of a new optical imaging modality for detection of fluorescence enhanced disease," PhD dissertation, Texas A & M University, 2003.

[114] M. Huang and Q. Zhu, "Dual-mesh optical tomography reconstruction method with a depth correction that uses a priori ultrasound information," *Appl. Opt.*, vol. 43(8), pp. 1654–1662, 2004.

[115] X. Gu, Y. Xu, and H. Jiang, "Mesh-based enhancement schemes in diffuse optical tomography," *Med. Phys.*, vol. 30, no. 5, pp. 861–869, 2003.

[116] J. P. Culver, R. Choe, M. J. Holbroke, L. Zubkov, T. Durduran, A. Slemp, V. Ntziachristos, B. Chance, and A. G. Yodh, "Three dimensional diffuse optical tomography in parallel plane transmission geometry: Evaluation of hybrid frequency domain/continuous wave clinical system for breast imaging," *Medical Physics*, vol. 30, pp. 235–246, 2003.

[117] R. Roy, A. Thompson, A. Godavarty, and E. M. Sevick-Muraca, "Tomographic fluorescence imaging in tissue phantoms: A novel reconstruction algorithm and imaging geometry," *IEEE Transactions on Medical Imaging*, vol. 24, no. 2, pp. 137–154, 2005.

[118] A. Joshi, W. Bangerth, and E. M. Sevick-Muraca, "Adaptive finite element based tomography for fluorescence optical imaging in tissue," *Opt. Express*, vol. 12, pp. 5402–5417, 2004.

[119] J. S. Reynolds, T. L. Troy, and E. M. Sevick-Muraca, "Multi-pixel techniques for frequency-domain photon migration imaging," *Biotechnolgy Progress*, vol. 13, pp. 669–680, 1997.

[120] B. Kaltenbacher, "A projection regularized newton method for nonlinear ill-

posed problems and its application to parameter identification problems with finite element discretization," *SIAM Journal on Numerical Analysis*, vol. 37(6), pp. 1885–1907, 2000.

[121] I. E. Smith, "Efficacy and safety of Herceptin (R) in women with metastatic breast cancer: Results from pivotal clinical studies," *Anti-Cancer Drugs*, vol. 12, pp. S3–S10, 2001.

[122] D.W.Kelly, S. Gago, O. Zienkiewicz, and I. Babuska, "A posteriori error analysis in finite element method: Part ii–adaptive mesh refinement," *Int. J. Numer. Math. Eng*, vol. 19, pp. 1621–1656, 1983.

[123] M. Salazar-Palma, T. K. Sarkar, L. E. G. Castillo, and A. Djordjevic, *Iterative and Self Adaptive Finite Elements in Electromagnetic Modeling.* Norwood: Artech House, 1998.

APPENDIX A

HOMODYNE DATA ACQUISITION

The response time of the ICCD camera system is not fast enough to acquire frequency domain optical signal, hence homodyne techniques are used which reconstruct the sinusoidal measurements by sampling the signal at a finite number of phase delays. Reynolds et al have described in detail the ICCD homodyne detection system for fluorescence optical imaging [119]. In homodyne mode of data analysis the intensity of the laser light source for the tissue phantom and the gain on the primary detection device that is the photo cathode of the image intensifier are modulated at the same frequency. The sinusoidal optical signal at the boundary of the tissue phantom can be described as:

$$I = I_{dc} + I_{ac}cos(\omega t + \theta) \tag{A.1}$$

ω is the modulation frequency; I_{dc} is the average intensity; I_{ac} is the amplitude of the sinusoidal signal and θ is the phase lag. The gain G on the photocathode of the image intensifier is also modulated in a similar fashion:

$$G = G_{dc} + G_{ac}cos(\omega t + \theta_G) \tag{A.2}$$

The phase offset θ_G can be specified by the data acquisition system. The signals I and G are mixed at the photocathode of the image intensifier to produce the signal

M which can be described as:

$$M = IXG = I_{dc}G_{dc} + I_{dc}G_{ac}cos(\omega t + \theta_G) + I_{ac}G_{ac}cos(\omega t + \theta) + \frac{I_{ac}G_{ac}}{2}cos(\theta_G - \theta) + \frac{I_{ac}G_{ac}}{2}cos(2\omega t\theta_G + \theta) \quad \text{(A.3)}$$

The high frequency components of M are filtered out by the phosphor screen of the image intensifier which converts the electronic signal back to optical signal, as a result the image captured by the CCD camera is a steady state image corresponding to particular phase offset θ_G:

$$M(\theta_G) = I_{dc}G_{dc} + \frac{I_{ac}G_{ac}}{2}cos(\theta_G - \theta) \quad \text{(A.4)}$$

To obtain the measurements of amplitude attenuation of the diffuse light and its phase shift relative to the source, The gain on the photo cathode is phase shifted before acquiring an image and this phase shift is varied over the full 2π cycle to capture a series of steady state images along one complete wavelength of the detected diffused intensity wave on each pixel. The amplitude and phase of the detected signal can be determined by a sinusoidal fit on the captured steady state images for different phase delays for each pixel. Fast Fourier transform(FFT) is a computationally efficient way to perform this sinusoidal fit. After the FFT, only the first frequency in the spectrum, which corresponds to the full cycle, is taken and AC and phase

components of the data for each pixel are determined by:

$$F = FFT(M(\theta_G)) \tag{A.5}$$

$$I_{ac} = \sqrt{real(F)^2 + imag(F)^2} \tag{A.6}$$

$$\theta = tan^{-1}\frac{imag(F)}{real(F)} \tag{A.7}$$

APPENDIX B

TWO DIMENSION ADAPTIVE FLUORESCENCE TOMOGRAPHY WITH TRIANGULAR FINITE ELEMENTS*

A. Introduction

The success of human genome project has paved the way for the complete characterization and quantization of biological processes at the molecular level. The ability to molecularly target therapeutic agents to specific disease markers (such as Herceptin receptors in breast cancer [121]), has spawned an urgent need for a clinical, diagnostic imaging technique for selection of appropriate molecular therapies. Fluorescence enhanced optical tomography is a novel functional imaging modality which is well suited for molecular imaging of targets in nanomolar tissue concentrations [22]. The tomography problem itself involves identification of a distributed parameter involving the recovery of the interior optical property map from the knowledge of the source distribution and a sampling of the boundary measurements, that satisfies a coupled system of elliptic partial differential equations. This is an ill-posed inverse problem. Finite element simulations of light transport in the tissue constitute the bulk of computational requirements for the parameter estimation algorithms. A fine discretization improves the quality of the simulation but at the same time increases

---

the ill-posed ness of the inverse problem by increasing the number of unknown parameters to be estimated. In this article we propose a novel algorithm which couples adaptive finite element meshing schemes with large scale non-linear optimization algorithms for computationally efficient and stable solution of the fluorescence tomography problem.

B. Mathematical model for light transport in tissue

In fluorescence enhanced frequency domain optical tomography a sinusoidally modulated Near Infrared laser light source is applied to the boundary of the domain. The light propagates diffusively throughout the domain and upon encountering a fluorescently tagged target is absorbed and produces fluorescent light. The modulated fluorescence light is detected at the boundary of the domain (Fig.34). The amplitude and phase of fluorescent wave can be predicted by the coupled diffusion equations [39].

$$-\nabla \cdot [D_x(\mathbf{r})\nabla\Phi_x(\mathbf{r},\omega)] + [\frac{i\omega}{c} + \mu_{axi}(\mathbf{r}) + \mu_{axf}(\mathbf{r})]\Phi_x(\mathbf{r},\omega) = 0 \tag{B.1}$$

$$-\nabla \cdot [D_m(\mathbf{r})\nabla\Phi_m(\mathbf{r},\omega)] + [\frac{i\omega}{c} + \mu_{ami}(\mathbf{r}) + \mu_{amf}(\mathbf{r})]\Phi_m(\mathbf{r},\omega) = \phi\mu_{axf}\frac{1}{1-i\omega\tau}\Phi_x(\mathbf{r},\omega) \tag{B.2}$$

where Φ is the complex photon fluence of the excitation or emission radiation. $\Phi = Iexp(-i\varphi)$. I is the amplitude (photons/cm^{2}s) and φ is the phase shift relative to incident excitation light; 'x' stands for NIR excitation and 'm' for fluorescent

emission; $D_{x,m}$ (cm) is the optical diffusion coefficient at excitation and emission wavelength; c is the velocity of light in the media; $\mu_{ax,mi}$ (cm^{-1}) is the absorption owing to natural chromophores; $\mu_{ax,mf}$ (cm^{-1}) is the absorption due to fluorophores; ω is the angular modulation frequency(rad/s); ϕ is the quantum efficiency of fluorescent emission and $\tau$is the lifetime(ns) of the fluorophores. Equations (B.1) and (B.2) are solved with the Robin boundary conditions:

$$2D_{x,m}\frac{\partial \Phi_{x,m}}{\partial n} + \gamma \Phi_{x,m} + S\delta(\mathbf{r}, \mathbf{r}_s) = 0 \; on \; d\Omega \tag{B.3}$$

Where n denotes the outward vector normal to the surface. In the fluorescence tomography problem considered in this contribution all the parameters except μ_{axf} are considered to be known. The distribution of μ_{axf} over the entire domain is identified from the boundary emission fluence measurements.

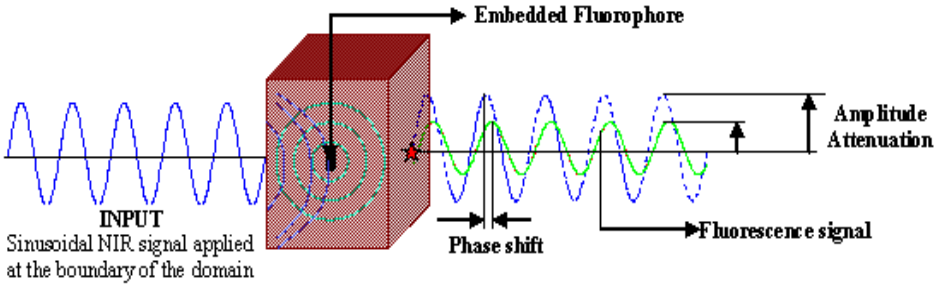

Fig. 34. Frequency domain fluorescence optical measurements

C. Inverse problem

In the fluorescence tomography problem considered in this contribution all the parameters except μ_{axf} are considered to be known. The image reconstruction problem involves identification of μ_{axf} distribution over the entire domain from the bound-

ary emission fluence measurements. This inverse problem is formulated as a simply bound constrained minimization problem:

min $E(x)\ \forall\ x$ s.t $lb \leq x \leq ub$

$$E(x) = \left\| \frac{Ax - z}{z} \right\|_2^2 \tag{B.4}$$

Here x is the unknown parameter to be estimated which is in our case. The term z denotes the experimentally measured boundary fluorescence fluence distribution and A denotes the elliptic operator defined by equations (B.1) and (B.2) which maps the optical property distribution onto the boundary fluorescence fluence distribution. The terms lb and ub denote the lower and upper bounds on x which are assumed known. In practice a finite number of boundary measurements are made for each source position. The error functional can then be written as:

$$E(x) = \frac{1}{2} \sum_{i=1}^{ns} \sum_{j=1}^{nd} \left(\frac{Ax_{ij} - z_{ij}}{z_{ij}}\right)\left(\frac{Ax_{ij}^* - z_{ij}^*}{z_{ij}^*}\right) \tag{B.5}$$

Here 'ns' denotes the number of excitation sources and 'nd' denotes the number of boundary measurements made for each source. Before the minimization can be carried out, the parameter distribution and the state equations described by the system of equations (1) need to be discretized. Galerkin finite element scheme is employed for this purpose [39]. We propose a novel scheme with separate finite element meshes for the parameter and the state equation solver. Both the meshes are adaptively refined to ensure optimality of the state equation solution and control of resolution in image reconstruction process while at the same time minimizing the computational effort.

D. Adaptive finite element mesh refinements for inverse problem

1. State equation discretization

The minimization routine iteratively updates the interior μ_{axf} map. Determination of these updates requires repeated solution of the coupled diffusion equations (B.1) and (B.2). We have employed the Galerkin finite element method. The problem domain is subdivided into triangular finite elements. A finer mesh ensures more accurate solution, however mesh needs to fine only where the error in solution is larger but the exact solution is unknown. This creates a need for the generation of a posteriori error estimates which identify the triangles to be refined once a trial solution has been computed on a coarse mesh. Solution process is started with a coarse mesh and the successive meshes are generated according to the a posteriori error estimator. To develop the error estimates for coupled diffusion equations we have followed the procedure developed by Kelly [122] and Salazar-Palma [123]. Kelly's error estimator is a residual based energy norm estimator which essentially refines the mesh where the gradient of the solution shows rapid variation. The error for each triangular element is calculated by the following equation:

$$\in_e^2 = \alpha_e \int_{\Omega^e} r_s^2 d\Omega + \beta_e \sum_{\Gamma_k \subset \Gamma_{\Omega^e}} \int_{\Gamma_k} r_{ed}^2 d\Gamma \tag{B.6}$$

Here r_s and r_{ed} are the surface and lumped edge residuals of the intra-element and inter-element photon fluence flux densities. α_e and β_e are weighing factors depending upon the triangle dimensions. The global error for the finite element mesh is

determined by summing the local error for all the elements:

$$\|e\|_{\Omega}^{2} = \sum_{e=1}^{N_e} \in_{e}^{2} \tag{B.7}$$

If global error is greater than a predefined threshold the mesh is refined then the mesh is refined wherever the local error is greater than 50% of the maximum error, that is if

$$\frac{\in_{e}^{2}}{max(\in_{e}^{2})} \geq 0.5 \tag{B.8}$$

The triangles which were marked to refined were subdivided into four triangles. To maintain the continuity of the mesh neighboring triangles are also refined to some degree.

E. Parameter discretization

The unknown parameter x is also discretized on a separate triangular mesh which is coarser than the state equation mesh to ensure that the inverse problem is well posed. The parameter mesh is adapted when the error function has converged on the coarser mesh. This refinement is driven by the jump in the reconstructed unknown parameter. In effect this refines the mesh at the boundaries of the fluorescent heterogeneity embedded in the domain and thus improves the resolution of the reconstructed image only where needed. The refinement criteria we have used is inspired by the work of Molinari et al [105] in electrical impedance tomography. The elemental error estimate for the parameter mesh estimates the smoothness of the parameter distribution. It is given by:

$$\in_{e}^{p} = \sum_{edges} |log(x_i) - log(x_j)|\, l_{ij} \tag{B.9}$$

Where l_{ij} is the length of the edge separating element i and element j. x_i is the value of the parameter in the triangle i. The criterion described in equation (B.8) is used to determine the triangles to be refined.

F. Inversion algorithm

We have employed the limited memory BFGS method with simply bound constraints [83] to carry out the minimization of the error functional. Limited memory BFGS method is a quasi-Newton optimization method which approximates the second derivative of the error function by storing the gradients of error function at previous five iterates. This results in a robust and memory efficient algorithm. The quasi-Newton update for the μ_{axf} map is given by

$$\mu_{axf}^{k+1} = \mu_{axf}^{k} - \alpha^k (H^k)^{-1} g^k$$

Here g^k is the gradient of the error function evaluated at kth iterate. The gradients of the error functional are constructed by an ad joint differentiation scheme [39] employing the finite element discretization of the state equations; H^k is the Hessian matrix of the error function at the current iterate. It is approximated by the following expression:

$$H^{k+1} = (I - \rho s_k y_k^T) H^k (I - \rho y_k s_k^T) + \rho s_k s_k^T$$

Where $s_k = \mu_{axf}^{k+1} - \mu_{axf}^{k}$

$y_k = g_{k+1} - g_k$

The number of vectors k stored can be varied according to the dimensions of the problem. We have gotten optimal results with $k = 5$. The term α^k is the step length which is determined by the line search procedure of More and Thuente [84]. We

have used the information about lower and upper bounds of μ_{axf} in determining the update direction. This helps in minimizing computational costs and ensuring feasible solutions. When the error function converges on a given mesh, the meshes for the state and parameter variables are refined. This process is continued till there is no further decrease in error function.

G. Implementation and results

The inversion process is outlined above was tested with synthetic measurement data generated on a two dimensional domain. The domain used is an ellipse with a fluorescent heterogeneity embedded in the middle (Fig.35).

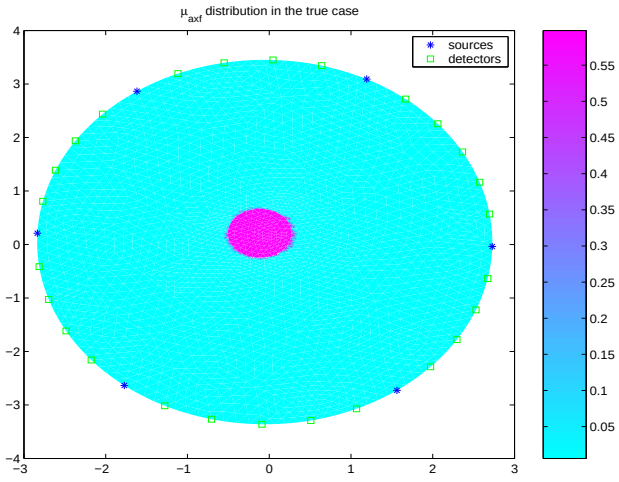

Fig. 35. Domain used for generating synthetic data

The optical properties are fixed to have a fluorescence absorption contrast of 100 : 1 in the embedded heterogeneity with respect to the background. Six sources

and twenty six detectors for each source are used. To generate the boundary fluorescence fluence measurements the coupled diffusion equations were solved on a very fine finite element mesh with 2257 nodes and 4384 triangles. The reconstruction algorithm started with coarse meshes (154 nodes) for the state and the unknown parameter (fluorescence absorption coefficient) and the meshes were adaptively refined during the iterations of the limited memory BFGS method. The final solution was obtained in 250 iterations. The final state mesh contained 751 nodes and the parameter mesh contained 401 nodes. Fig.36 shows the evolution of the state and parameter meshes. MATLAB's PDE Toolbox was used to generate and adaptively refine the finite element meshes for these contributions. Fig.37 shows the reconstructed image.

A substantial accuracy was attained in the state equation solution as the global solution error was matched with a 2257 node mesh with only 751 nodes.In the parameter mesh, maintaining a separate adaptable discretization helped in keeping the number of unknowns to 401 while still providing a finer resolution at the boundary of the heterogeneity.

The efficiency achieved by adaptive finite element schemes is demonstrated in Fig.38 which compares the decrease in global error(eqn(B.7)) attained by adaptive mesh refinement with that attained by uniform global refinement.

To reduce the global error to a level equivalent to global refinement, adaptive refinement requires an order of magnitude less number of nodes. This results in a two order of magnitude saving in the computational cost of the algorithm.

H. Conclusions and future Work

We have demonstrated a novel approach to handle large dimensional ill-posed system identification problems for distributed parameter systems with adaptive finite elements. The approach can be readily transformed for handling three dimensional systems provided sophisticated tools for handling three dimensional meshes are available. Currently work is underway on applying these techniques for three dimensional problems and on working with actual experimental data obtained in the photon migration laboratories.

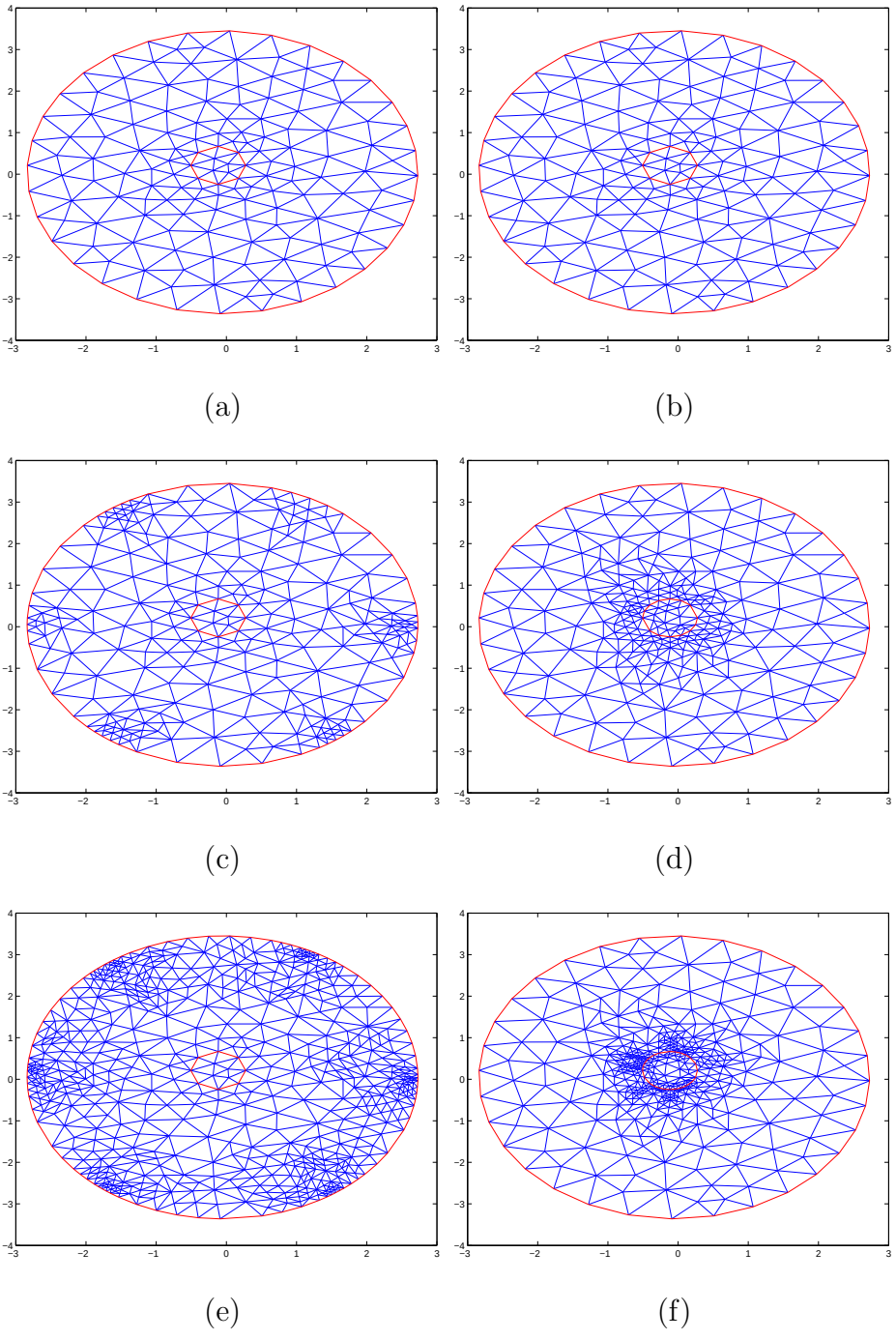

Fig. 36. Self adaptive mesh evolution for state and parameter discretization

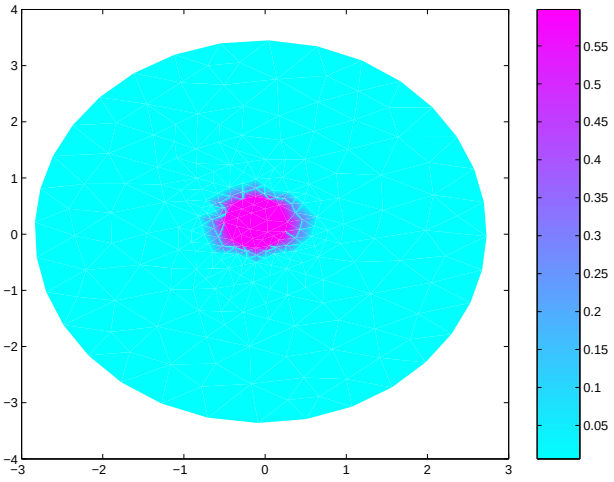

Fig. 37. Recovered μ_{axf} map

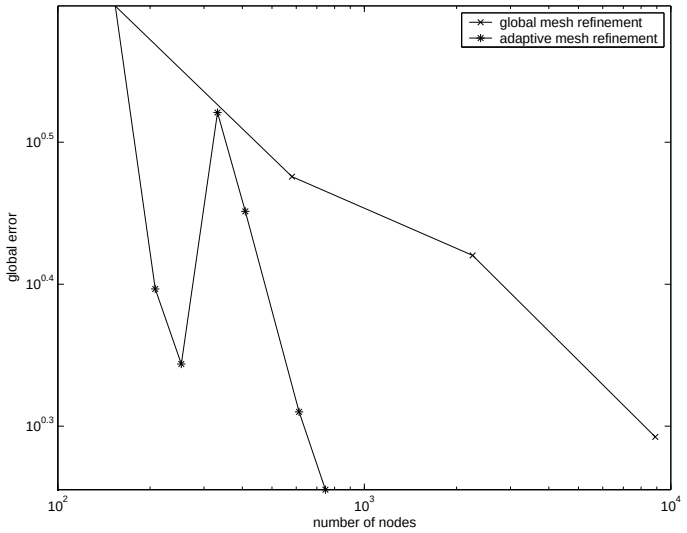

Fig. 38. Global error decrease with adaptive and uniform refinement

VITA

Amit Joshi was born in Haridwar, India, on September 23, 1978. He attended the Central government school at Rishikesh, India. Amit finished in the top 0.1% of the 12^{th} grade students, who appeared in the Central Board of Secondary Education chemistry examination, all over India. He joined the Department of Chemical Engineering at Panjab University, Chandigarh, which is the second oldest chemical engineering department in India, and graduated with an honors bachelor's degree in chemical engineering in June 2000. Amit graduated at the top of the class and was awarded the University Gold Medal for academic performance. In addition, he held the univeristy merit scholarship for all four years of his stay in Panjab University. Amit joined the Department of Chemical Engineering at Texas A&M University in August 2000. He started working on his Ph.D. at the Photon Migration Laboratories under the supervision of Dr. Eva Sevick-Muraca in June 2001. During his doctoral student tenure, Amit won the first prize at the Graduate Student Research Week oral presentation competition. He also won the Seimens Young Investigator travel award at the 3^{rd} Annual Conference of the Society of Molecular Imaging at St. Louis, MO, September 2004. Following the completion of his doctorate in summer 2005, Amit will take up the position of Research Associate at the Baylor College of Medicine in Houston, TX.

The typist for this dissertation was Amit Joshi.